THE SUNYAEV-ZELDOVICH EFFECT AS A PROBE OF BLACK HOLE FEEDBACK

by

Suchetana Chatterjee

Bachelor of Science, Presidency College (Calcutta University), 2001

Master of Science, Indian Institute of Technology, Kanpur, 2003

Submitted to the Graduate Faculty of

the Department of Physics and Astronomy in partial fulfillment

of the requirements for the degree of

Doctor of Philosophy

University of Pittsburgh

2009

UNIVERSITY OF PITTSBURGH

DEPARTMENT OF PHYSICS AND ASTRONOMY

This dissertation was presented

by

Suchetana Chatterjee

It was defended on

August 3, 2009

and approved by

Arthur Kosowsky, Associate Professor

David Turnshek, Professor and Department Chair

John Hillier, Professor

Chandralekha Singh, Associate Professor

Grant Wilson, Assistant Professor

Dissertation Director: Arthur Kosowsky, Associate Professor

ABSTRACT

THE SUNYAEV-ZELDOVICH EFFECT AS A PROBE OF BLACK HOLE FEEDBACK

Suchetana Chatterjee, PhD

University of Pittsburgh, 2009

Feedback from supermassive black holes has a substantial but only partially understood impact on structure formation in the universe. The Sunyaev-Zeldovich signal from the hot gas that is present in black hole environments serves, as a potential probe of this feedback mechanism. Using a simple one-dimensional Sedov-Taylor model of energy outflow we calculate the angular power spectrum of the Sunyaev-Zeldovich distortion. The amplitude of temperature fluctuation is of the order of a micro-Kelvin in the cosmic microwave background at arcminute scales. This signal is at or below the noise level of current microwave experiments including the Atacama Cosmology Telescope and the South Pole Telescope.

To further investigate this effect we have constructed microwave maps of the resulting distortion around individual black holes from a cosmological hydrodynamic simulation. The simulation employs a self-consistent treatment of star formation, supernova feedback and accretion and feedback from supermassive black holes. We show that the temperature distortion scales approximately with the black hole mass and accretion rate, with a typical amplitude up to a few micro-Kelvin on angular scales around 10 arcseconds. We also discuss the possible techniques for detection of this signal which includes pointed observations from high resolution millimeter wave telescopes and cross-correlation of optical quasar catalogs with microwave maps.

We perform a cross-correlation analysis of the signal, by stacking microwave maps of quasars identified in the Sloan Digital Sky Survey. We use the microwave data from the

Wilkinson Microwave Anisotropy Probe experiment to do this analysis. We perform a two-component (SZ+Dust) fit to the cross-correlation spectrum. Our results yield a best fit y parameter of $(5.8 \pm 1.8) \times 10^{-7}$. This signal is likely to be originating from the Sunyaev-Zeldovich distortions from intervening large scale structures. We show that the Atacama Cosmology Telescope will be able to constrain this signal with a much higher statistical significance.

In this work we have shown that a traditional tool of cosmology, namely the microwave background, can be used as a potential probe of feedback from supermassive black holes, which is an interesting problem in theories of galaxy evolution.

keywords: cosmic microwave background — cosmology:theory — galaxies:intergalactic medium — quasars:general — submillimeter.

TABLE OF CONTENTS

LIST OF TABLES

LIST OF FIGURES

PREFACE

The education of the individual, in addition to promoting his own innate abilities, would attempt to develop in him a sense of responsibility for his fellow men in place of the glorification of power and success in our present society.

Albert Einstein

I had the privilege to grow up in a social environment where education was given a lot of priority, and I was certainly blessed with an education system where I could afford the best schools and colleges for free. I thank the Indian government and the people of India and I am indebted to them for this purpose. My primary and high school teachers from Mary Immaculate School (MIS) Berhampore and Maharani Kashiswari Girls' High School (MKGHS) were wonderful. It is their love and inspiration in those tender years that gave me the confidence and courage to accomplish in life. My higher secondary education at Berhampore Girls' college (BGC) was also a great experience. BGC was one of the leading institutes in the district of Murshidabad, in promoting higher education for women in science. It was MIS, MKGHS, and BGC where I acquired important skills like working in groups, leading class projects, and participating in seminars and co-curricular activity. These skills played pivotal roles in shaping my later scientific career.

1998-2001 were probably the best years of my life in terms of personal and professional excellence. The amazing intellectual environment of Presidency College built the base of my conception of science and I exactly knew what future would be awaiting me. I pay my deepest respect to all my professors and non teaching staff at Presidency College for their guidance, support, love and utmost care. I would specially like to mention Prof. Dipan-

jan Roychowdhury, Prof. Debapriya Syam, Prof. Pradip Kumar Datta, and Prof. Shyamal Chakraborty with whom I shared personal relations. Our beloved laboratory assistant Santosh da (which means elder brother Santosh) was one of the rare people I have seen in my academic career with such a strong work ethic and yet so caring.

My next venture at Indian Institute of Technology Kanpur (IITK) was a challenging yet enlightening experience with academic ecstasy. I was able to interact and learn from some of the eminent Physicists of the country. Prof. S D Joglekar's Mathematical methods, Prof. Sreerup Raichaudhuri's quantum mechanics, Prof. Pankaj Jain's quantum field theory made me fall in love with theoretical physics. I had the opportunity to spend a summer at Harish Chandra Research Institute (HRI) as a visiting summer student while at IITK. That was my first experience with cosmology research. I am thankful to Prof. Pinaki Majumdar for his help and support as a coordinator of the summer program and Prof. J S Bagla for mentoring my summer research.

From IITK to University of Pittsburgh was a "great leap forward". It was in Pittsburgh, where I transformed to a matured scientist and professional from a class-going student. I was so lucky to step into a department where Physics teaching received a lot of attention. I had the prime opportunity to have eminent teachers like Prof. Adam Leibovich, Prof. Frank Tabakin, and Prof. Yadin Goldschmidt. My experimental internship at Prof. Heberle's lab was a creative experience. That's when I came to learn how hard an experimenter's job is. It was a lifetime experience for me to have a teacher and mentor like Prof. Dan Boyanovsky. His General Relativity and Astroparticle physics classes were the best classes in my life. Thanks to Prof. Boyanovsky for teaching me several theoretical concepts that were extremely valuable during the course of this work. My deepest regards to Prof. Andy Connolly and Prof. Ravi Sheth for being my mentors in the first two years of graduate school. I have special regards for Prof. Chandralekha Singh with whom I shared both personal and professional relations. My summer internship on "Physics Education Research" with her and working with her as a teaching assistant for Physics 0175 were great experiences. It was a pleasure to have Dr. Singh on my thesis committee. I am thankful to Prof. David Turnshek and Prof. John Hillier for serving on my thesis committee, teaching me astrophysics, and supporting me all through. I am grateful to Prof. Tiziana Di Matteo, for letting me work with her simulations,

on which Chapter 5 of this thesis is based. I thank Prof. Grant Wilson for serving on my committee and providing useful suggestions about the work that lead to the completion of this thesis. I am extremely privileged to have Prof. Jeff Newman as one of my academic mentors and colleagues in the department. It was his idea that led to the work described in Chapter 7. Prof. Newman inspired me to get into the mammoth task of working with real data. I am indebted to Prof. Newman for teaching me lot of statistical techniques, and always answering my naive questions related to astrophysical observations. I am grateful to Prof. Andrew Zentner for some useful discussions throughout the course of this work. I am especially thankful to Prof. Sandhya Rao for being supportive of me during my hard times in graduate school and being a careful proof reader of my thesis and papers. Last but not least is my advisor Prof. Arthur Kosowsky. Arthur was more of a friend than an advisor. Physics was not the only thing we chatted about. We had in numerous discussions about society, politics, art, music, education systems and what not. He was very enthusiastic about my personal success and achievements.

It was a pleasant experience to have wonderful colleagues and collaborators. Dr. Inti Pelupessy and Dr. Shirley Ho had been great colleagues to work with. Inti's patient efforts in explaining GADGET to me and simulations in general were extremely helpful. It was Shirley's enthusiastic efforts that led to the completion of the work described in Chapter 7. I thank her for the hours of discussion we had over phone and in person during the course of this work. My sincere gratitude to Prof. Evan Scannapieco, Dr. Neelima Sehgal, Prof. Eichiro Komatsu, Dr. Ryan Scranton, Prof. Tim Hamilton, Prof. Andrew Blain, Prof. James Moran, Prof. Bruce Partridge, Prof. Mark Gurwell, Dr. Christoph Pfrommer, Prof. Avi Loeb, and Prof. James Aguirre for useful discussions and suggestions related to different aspects of the work described in Chapters 4, 5, 6 and 7 of this thesis. I am extremely thankful to Prof. David Spergel for providing guidance throughout the work described in Chapter 7. His suggestion of Weiner filtering the maps was one of the key steps for determining the cross-correlation signal. I would also like to thank the department of Astrophysical Sciences at Princeton University for hosting my visits at Princeton where some of the work for Chapter 7 was done. I thank Valery Rashkov for providing his thesis which was useful for deriving the exact form of the Weiner filter. I acknowledge Craig Markwardt for use of the MPFIT package, the Legacy

Arxiv for Microwave Background Data Analysis (LAMBDA) for providing the data products from the Wilkinson Microwave Anisotropy Probe (WMAP) science team and the National Radio Astronomy Observatory (NRAO) for providing the NRAO-VLA Sky Survey (NVSS) source catalog. Thanks to Lewis and Challinior for providing the Code for Anisotropies in the Microwave Background (CAMB) source code and Jet propulsion Laboratory (JPL) for providing the HEALPix package.

The list will be incomplete if I do not mention the role of my friends and peers in helping me achieve success. We learned from each other and within a healthy environment of competition we really cared about each other's success too. The endless hours of discussions, argument, agreement, and disagreement played monumental roles in my understanding of Physics. It was those Easter years where we learned from each other, taught each other and unlocked our imagination. Ritaban, Kunal, Soumya, Subhayan, Didhiti, Seemanti, Sanghamitra and Saiti are some to specially mention. I am proud to say that eight of my batch mates from Presidency and IITK became successful Astrophysicists. The person who played the most significant role in my academic life is Ritaban. I feel so fortunate to have a friend and colleague like him. It was his support, advice (both academic and off-academic) and enthusiasm for the last eleven years that kept my motivation firm and drove me to the road of success. We worked as a team in every aspect of life ranging from Boston 'Finale' to Astrophysics. I never felt alone and never felt afraid since Ritaban was always with me. Dipankar Maitra, one of my seniors at Presidency College was also extremely helpful in giving me suggestions all through my Physics career. Satarupa Sengupta acted as an elder sister during my years in Presidency college girls' hostel. It was because of her that I barely felt out of home.

In Pittsburgh I had nice people to interact with. I would specially mention my IITK classmate Suman Bhattacharya and my officemates Yi-Cheng Huang, Mei-Wu Yang, and Benjamin Brown. My heartiest thanks to our graduate secretary, Leyla Hirschfield. She was always helpful about so many things that I can not even list here. Thanks to our computer consultant Greg Gollinger, for his limitless help during the course of this work. My best regards to Michele Slogan, Laura Provolt, Jim Stango, Lynn Ruminski, and our ex-assistant chair Judy Stern for help with several administrative affairs. My roommate Amrita and

several other friends made my living in Pittsburgh a pretty enjoyable experience.

Finally, I would like to mention my family and relatives for giving me so much love and affection all through these years. It was a difficult situation to leave them back home and come and work in a foreign land. If it wasn't their love and support I wouldn't have had the determination and strength. Having a Physicist father was enough enthusiasm and inspiration for me to become a Physicist. It is hard for me to mention some names and not to mention others since all of them are so important and special to me. So I would just mention my maternal grandfather Shree Sishir Kumar Mukherjee whom I lost thirteen years back, and whose love and care are something that I still miss today.

This work was supported by the National Science Foundation through grant AST-0408698 to the ACT project, by grant AST-0546035, the Mary. E. Warga fellowship, the Zaccheus Daniel Fellowship, the Andrew Mellon Fellowship, and several teaching assistantships at the University of Pittsburgh. Funding for the Sloan Digital Sky Survey (SDSS) and SDSS-II has been provided by the Alfred P. Sloan Foundation, the Participating Institutions, the National Science Foundation, the U.S. Department of Energy, the National Aeronautics and Space Administration, the Japanese Monbukagakusho, the Max Planck Society, and the Higher Education Funding Council for England. The SDSS Web Site is http://www.sdss.org/.

The SDSS is managed by the Astrophysical Research Consortium for the Participating Institutions. The Participating Institutions are the American Museum of Natural History, Astrophysical Institute Potsdam, University of Basel, University of Cambridge, Case Western Reserve University, University of Chicago, Drexel University, Fermilab, the Institute for Advanced Study, the Japan Participation Group, Johns Hopkins University, the Joint Institute for Nuclear Astrophysics, the Kavli Institute for Particle Astrophysics and Cosmology, the Korean Scientist Group, the Chinese Academy of Sciences (LAMOST), Los Alamos National Laboratory, the Max-Planck-Institute for Astronomy (MPIA), the Max-Planck-Institute for Astrophysics (MPA), New Mexico State University, Ohio State University, University of Pittsburgh, University of Portsmouth, Princeton University, the United States Naval Observatory, and the University of Washington.

DEDICATED TO THE MEMORY OF MY TEACHERS

WHOM I LOST DURING THE COURSE OF THIS WORK

Shree Prakash Chandra Basu

and

Prof. Yadin Goldschmidt

1.0 INTRODUCTION

In this Chapter, I will develop the motivation for this dissertation work and give a brief description of the remaining Chapters in this thesis.

1.1 THE STANDARD MODEL OF COSMOLOGY

One of the triumphs of modern physics lies in its successful attempt in establishing the standard model of cosmology. Decades of theoretical and observational efforts from the entire physics community led to our firm understanding of the properties of the universe. It is now believed, through several observational results, that the universe started with a hot Big Bang and gradually expanded and cooled. In 1929 Edwin Hubble's phenomenal observation led to the idea of an expanding universe. Previously the idea of the primeval atom and the beginning of the universe was proposed by Friedmann and Lemaitre. In the 1940s George Gamow along with his collaborators Alpher and Hermann estimated that if light elements were produced following the beginning of the universe, then there should be a relic blackbody radiation of about 10 K in the present day universe (Kragh 1999). In 1964, this radiation was discovered by Penzias and Wilson. The radiation, called the cosmic microwave background (CMB) radiation, has a characteristic temperature of 3 K (Penzias & Wilson 1964). The discovery of the CMB marked the modern era of cosmology. After the launch of the COsmic Background Explorer (COBE) satellite in 1989 the spectrum of the CMB was measured with extreme precision. The spectrum is a perfect blackbody with a characteristic temperature of 2.73 K (Mather et al. 1990). The temperature of the background radiation is extremely uniform with fluctuations of one part in 10^5 (Smoot et

al. 1992). Theoretically it was predicted that the growth and evolution of structures in the universe are seeded by small density perturbations in the early universe. The temperature fluctuations in the CMB observed by COBE were in good agreement with the theoretical predictions.

The findings of the COBE satellite were the first in a new wave of important cosmological observations. With the advancement of new technology, galaxy surveys were able to cover much larger areas on the sky and far greater depths in redshift. The Sloan Digital Sky Survey (SDSS) (Abazajian et al. 2003) gave us a wealth of information and revolutionized our understanding of the universe. With large data sets, the SDSS team measured the galaxy power spectrum (Tegmark et al. 2004) and detected the baryon acoustic peak in the large scale correlation function of galaxies (Eisenstein et al. 2005). The Wilkinson Microwave Anisotropy Probe (WMAP) (Bennett et al. 2003) satellite measured the power spectrum of the temperature fluctuations in the microwave background with much higher precision than COBE (about a factor of 30 in angular scale), resulting in strong constraints on the basic cosmological model. Luminosity distance measurements of distant supernovae from the Supernova Cosmology team (Perlmutter et al. 1999) and the High-Z Cosmology team (Riess et al. 1998) showed evidence for an accelerating expansion of the universe. These measurements, combined with lensing measurements and X-ray observations of galaxy clusters (e.g., Bradac et al. 2006; Clowe et al. 2006; Vikhlinin et al. 2009), drove a convergence to the standard model of cosmology known as the Lambda Cold Dark Matter (LCDM) paradigm.

The key features of this model are as follows: The universe is homogeneous and isotropic at large scales and the smooth component of the universe is well described by a Friedmann-Robertson Walker (FRW) solution to Einstein's field equations in general relativity. The initial density perturbations are Gaussian with a nearly scale invariant spectrum. These initial perturbations are responsible for the growth of structures in the universe. The universe is spatially flat to a very high degree. About seventy percent of the current energy density of the universe consists of a dark energy component which is responsible for driving the current phase of acceleration. About twenty five percent of the universe consists of non-relativistic (cold) dark matter which does not have electromagnetic interactions. The remaining 5% (approximately) of the universe is composed of baryonic matter. In addition it is believed

that inflation in the very early universe provides a mechanism for generating the initial perturbations.

The CMB has been the most powerful probe for constraining cosmology. The first constraint came from the discovery of the CMB in 1964 that effectively ruled out the steady state model of cosmology (Hoyle, Burbidge, & Narlikar 1993). Following this first discovery, there were several experiments that measured the temperature fluctuations in the CMB. Some of the recent ones are COBE (Smoot et al. 1992), WMAP (Bennett et al. 2003), Mobile Anisotropy Probe (MAT) (Miller et al. 1999), Balloon Observations of Millimetric Extragalactic Radiation and Geomagnetics (BOOMERANG) (de Bernardis et al. 2000), MAXIMA-1 (Hanany et al. 2000), Cosmic Background Imager (CBI) (Mason et al. 2003), Medium Scale Anisotropy Probe (MSAM) (Wilson et al. 2000), Very Small Array (VSA) (Dickinson et al. 2004), Degree Angular Scale Interferometer (DASI) (Halverson et al. 2002), Arcminute Cosmology Bolometer Array Receiver (ACBAR) (Reichardt et al. 2009), and ARCHEOPS (Tristram et al. 2005). A full list of CMB experiments is given in LAMBDA [1]. By accurately measuring the statistics of temperature fluctuations in the CMB sky, WMAP has firmly established the LCDM model and has measured the basic parameters of cosmology with very high precision (Dunkley et al. 2009; Komatsu et al. 2009). These parameters include the density of dark matter in the universe (Ω_{DM}), the density of baryonic matter in the universe (Ω_b), the Hubble constant (or the expansion rate of the universe H_0), the scale dependence of fluctuations (n_s), and the redshift of reionization (z_{reion}) (Komatsu et al. 2009).

These, when combined with other measurements, specify other parameters in cosmology. For example, the constraint on spatial flatness and the matter density in the universe provide constraints on the dark energy density parameter. The combined results from WMAP and other astronomical experiments (e.g., Hubble key project (Freedman et al. 2001), supernova luminosity distances (Kowalski et al. 2008), baryon acoustic oscillation (BAO) measurements from galaxy surveys (Percival et al. 2007)) gave new insights on the nature of the initial perturbation and any violation of the standard cosmological model. The CMB polarization measurement (e.g., Page et al. 2007) is potentially the smoking gun for detecting primor-

[1] http://lambda.gsfc.nasa.gov

Cosmological Parameter	Symbol	Value
Baryon density	Ω_b	0.0474 ± 0.0014
Dark matter density	Ω_{DM}	0.243 ± 0.013
Total matter density	Ω_m	$\Omega_b + \Omega_c$
Dark energy density	Ω_Λ	0.709 ± 0.014
Hubble constant	H_0	69.7 ± 1.3 km/s/Mpc
Matter fluctuation	σ_8	$0.851^{+0.020}_{-0.019}$
Age of the universe	t_0	13.64 ± 0.11 Gyr
Scalar Spectral index	n_s	0.969 ± 0.012
Redshift of reionization	z_{reion}	11.7 ± 1.4

Table 1.1: Standard cosmological parameters obtained by combining data from WMAP5, supernovae, Lyman alpha forest, and baryon acoustic oscillations experiments.

dial gravity waves from inflation (e.g., Kamionkowski, Kosowsky, & Stebbins 1997). The PLANCK [2] surveyor satellite will have better measurements of the CMB polarization and the nature of the primordial perturbations. The parameters of the standard cosmological model are summarized in Table 1.1 (Courtesy: LAMBDA[1]). The cosmological parameters are derived by combining WMAP 5 year data (Dunkley et al. 2009), BAO measurements from the Two Degree Field (2DF) and SDSS (Percival et al. 2007), Lyman alpha measurements (Seljak, Slosar, & Mcdonald 2006), and the supernova "Gold sample" (Riess et al. 2004).

[2]http://www.rssd.esa.int/Planck

1.2 THE SUNYAEV-ZELDOVICH EFFECT

The temperature fluctuations in the CMB described above are called primary anisotropies. Apart from the primary anisotropies in the CMB there are a class of temperature fluctuations in the CMB which arise due to the interaction of the microwave photons with matter in the low-redshift universe (see Aghanim, Majumdar, & Silk 2008 for a review). These low-redshift and small-angle anisotropies are collectively known as "secondary anisotropies" in the microwave background. The most prominent among them is the Sunyaev-Zeldovich (SZ) effect (Sunyaev & Zeldovich 1972), which is the inverse Compton scattering of the microwave photons by hot electrons. The CMB photons are scattered by the hot electrons, and as a result of that, the photons move from the Rayleigh-Jeans side to the Wein side of the spectrum. Due to conservation of photon number in the process, we see a deficit and enhancement of photons below and above a threshold frequency. This threshold frequency is called the null frequency and occurs at about 220 GHz. The decrease and increase in intensity manifest as cold and hot spots in the CMB temperature field. The SZ effect provides a powerful method for detecting accumulations of hot gas in the universe (see Carlstrom, Holder, & Reese 2002 for a review of SZ). Galaxy clusters, which contain the majority of the thermal energy in the universe, provide the largest SZ signal. Clusters were first detected this way through pioneering measurements over the past decade (e.g., Birkinshaw, Gull, & Northover 1978; Carlstrom, Joy, & Grego 1996; Joy et al. 2001), and thousands of them are expected to be detected by the upcoming SZ surveys like the Atacama Cosmology Telescope (ACT [3]) (Kosowsky et al. 2006) and the South Pole Telescope (SPT [4]) (Ruhl et al. 2004). This will enable us to use cluster number counts and cluster peculiar velocities as efficient cosmological probes (e.g., Mohr 2005; Bhattacharya & Kosowsky 2008).

However, a number of other astrophysical processes will also create SZ distortions. These include SZ distortion from peculiar velocities during reionization (McQuinn et al. 2005, Illiev et al. 2006), supernova-driven galactic winds (Majumdar, Nath, & Chiba 2001; White, Hernquist, & Springel 2000), kinetic SZ from Lyman Break Galaxy outflow (Babich & Loeb

[3]http://www.physics.princeton.edu/act/
[4]http://pole.uchicago.edu

2007), hot proto galactic gas (e.g, de Zotti et al. 2004, Rosa-Gonz'alez et al. 2004, Massardi et al. 2008), and supernovae from the first generation of stars (Oh, Cooray, & Kamionkowski 2003). Here, we investigate one generic class of SZ signals: the hot bubble surrounding an active galactic nuclei (AGN) powered by a supermassive black hole.

1.3 FEEDBACK FROM ACTIVE GALACTIC NUCLEI

Analytic models and numerical simulations of galaxy cluster formation indicate that the temperature and the X-ray luminosity in galaxy clusters should be related as $L_x \propto T^2$ in the absence of gas cooling and heating (see Peterson & Fabian 2006 for a review). Observations show instead that $L_x \propto T^3$ over the temperature range 2 to 8 kev with a wide dispersion at lower temperature, and a possible flattening above (e.g., Markevitch 1998; Arnaud & Evrard 1999). The simplest explanation for this result is that the gas had an additional heating of 2 to 3 keV per particle (e.g., Wu, Fabian, & Nulsen 2000; Voit et al. 2003). Several non-gravitational heating sources have been discussed in this context (see Peterson & Fabian 2006); AGN feedback (also alternatively called black hole feedback) (e.g., Binney & Tabor 1995; Silk & Rees 1998; Ciotti & Ostriker 2001; Nath & Roychowdhury 2002; Kaiser & Binney 2003; Nulsen et al. 2004) is perhaps the most realistic possibility.

The effect of this feedback mechanism on different scales of structure formation have been addressed by several authors (e.g., Mo & Mao 2002; Oh & Benson 2003; Granato et al. 2004). The evidence of AGN heating in cluster cores has been shown by different groups (e.g., McNamara et al. 2005; Voit & Donahue 2005; Sanderson, Ponman, & O'Sullivan 2006; see McNamara & Nulsen 2007 for a recent review). The impact of this non-gravitational heating in galaxy groups, which have shallower potential wells and thus smaller intrinsic thermal energy than galaxy clusters, can also be substantial (e.g., Arnaud & Evrard 1999; Helsdon & Ponman 2000; Lapi, Cavaliere, & Menci 2005). Observational efforts to detect the impact of AGN feedback have been carried out using galaxy groups in SDSS by Weinmann et al. (2006), and with a *Chandra* group sample by Sanderson, Ponman, & O'Sullivan (2006). Detailed theoretical studies of galaxy groups using simulations which include AGN feedback

have been undertaken by, e.g., Zanni et al. (2005), Sijacki et al. (2007), and Bhattacharya, Di Matteo, & Kosowsky (2007). At smaller scales the impact of AGN feedback has been investigated by Schawinski et al. (2007) with early-type galaxies in SDSS, and has also been studied in several theoretical models of galaxy evolution (e.g, Kawata & Gibson 2005; Bower et al. 2006; Cattaneo et al. 2007). Growing observational evidence points to a close connection between the formation and evolution of galaxies with their central supermassive black holes (e.g., Magorrian et al. 1998, Ferrarese & Merritt 2000, Tremaine et al. 2002) and their host dark matter halos (Merritt & Ferrarese 2001; Tremaine et al. 2002). Several groups have now investigated black hole growth and the effects of AGN feedback in the cosmological context (e.g., Scannapieco & Oh 2004; Di Matteo, Springel & Hernquist 2005; Lapi et al. 2006; Croton et al. 2006; Thacker, Scannapieco, & Couchman 2006, Sijacki et al. 2007).

In this dissertation work we have used the SZ distortions in the CMB produced from energy feedback due to supermassive black holes as a probe of the feedback energy. Probing black hole energy feedback via SZ distortions is a new direct observational route to understand the growth and evolution of supermassive black holes and their role in structure formation. Similar work has been carried out by Natarajan & Sigurdsson (1999), Aghanim, Balland, & Silk 2000, Yamada, Sugiyama & Silk (1999), Lapi, Cavaliere, & De Zotti (2003), Platania et al. (2002), Roychowdhury, Ruszkowski, & Nath (2005), Scannapieco, Thacker, & Couchman (2008), and Moodley et al. (2008). In the next Section a brief description of the Chapters in this thesis is presented

1.4 DESCRIPTION OF CHAPTERS

In Chapter 2, I will describe briefly the theoretical and observational aspects of the CMB and the temperature anisotropies in it. I will start with the primary anisotropy in the CMB and describe the secondary fluctuations and their cosmological implications. Finally, I will present a full derivation of the SZ effect starting from the Boltzmann equation and discuss its cosmological significance.

In Chapter 3, I will discuss the importance of AGN feedback and its role on growth of structures. I will also discuss possible experimental probes based on observations in other wave bands along with the SZ effect (X-ray, optical and radio). This will be followed by a survey of various theoretical models of AGN feedback.

Chapter 4 involves the calculation of the SZ distortion that we get from analytic modeling of AGN feedback. Our model relies on a one dimensional Sedov-Taylor solution of energy ejection. I will discuss the Sedov-Taylor formalism and describe the equations used for modeling the feedback process. I will then present the analytical calculations of the SZ distortion under a simplified set of assumptions about the geometry and the physical state of the system. I will discuss the calculation of the power spectrum of SZ distortion in multipole space using a halo model prescription and show its dependence on some of the free parameters in the model. Finally, I will calculate the observational signal for SZ distortion from the power spectrum using a Gaussian beam.

The work presented in Chapter 4 is based on the following publication: **Chatterjee, S., & Kosowsky, A., 2007, ApJL, 661, L113**. I have derived the Sedov-Taylor equations for the particular case following Scannapieco & Oh (2004). I developed the code to do the halo model calculation of the power spectrum and obtained the observational signal from the power spectrum. The initial idea for the project was suggested by Evan Scannapieco. Arthur Kosowsky provided general feedback, revised the draft, and suggested the idea of calculating the experimental signal.

Chapter 5 involves numerical simulation of the SZ effect from AGN feedback. This work is complimentary to the analytic model discussed in Chapter 4, since we use a different model of feedback in the simulations carried out by Di Matteo et al. (2008). This gives us an opportunity to compare our analytic results with the numerical results. I will begin with a description of the implementation of the simulation that we have used. This will be followed by a presentation of the SZ distortion maps and the corresponding angular profiles. Finally, I will describe the mass scaling relations that have been derived from the simulation.

The work presented in Chapter 5 is based on the following publication: **Chatterjee, S., Di Matteo, T., Kosowsky, A., & Pelupessy, I., 2008, MNRAS, 390, 535**. I have analyzed the data from the simulation performed by Di Matteo et al. (2008). I have

developed the code to do the line-of-sight integral and produced the 2 dimensional maps presented in this thesis. I have generalized the code for performing the line-of-sight integral for all the black holes in the simulation to compute the mass-scaling relations. The basic code to read in the simulation data and the map-making algorithm was provided by Tiziana Di Matteo. Tiziana Di Matteo also helped to improve the draft. Inti Pelupessy helped with debugging the codes and provided useful suggestions. Arthur Kosowsky provided general feedback and revised the draft.

In Chapters 6 and 7, I will describe the techniques that can be used to measure the SZ distortion due to feedback from AGN. The two methods that I have proposed are direct detection through pointed observations in millimeter wave band, and statistical analysis via cross-correlation with observations at other wavelengths. In Chapter 6, I will sketch the optimum configuration for direct detection. In Chapter 7, I will present the cross-correlation analysis of the signal using data from WMAP and the SDSS quasar catalog.

The work presented in Chapter 7 is based on the following publication: **Chatterjee, S., Ho, S., Newman, J. A., & Kosowsky, A., 2009 (to be submitted to ApJ)**. I have analyzed the public data from the WMAP collaboration (Hinshaw et al. 2009), and the SDSS catalog prepared by Ho et al. (2008). I have developed the analysis pipeline using the public software packages: HEALPix (Gorski et al. 2000), WMAP's IDL analysis software, Goddard library codes, and the IDLUTILS library (David Schlegel) to filter the CMB maps, construct the masks, and perform the cross-correlation analysis. The original idea for the project was suggested by Jeff Newman and David Spergel. Shirley Ho provided very useful suggestions for developing the analysis pipeline, revised the draft, and provided the quasar catalog. David Spergel suggested that we use the filters and provided general feedback. Jeff Newman gave several suggestions on the statistical methods used to interpret the result and helped improve the draft. Arthur Kosowsky provided some general feedback, helped in interpreting the results, and revised the draft.

In Chapter 8, I will give a summary of the work presented in this thesis and suggest some future extensions of this work.

2.0 ANISOTROPIES IN THE COSMIC MICROWAVE BACKGROUND

In this Chapter, I will briefly describe the theoretical and observational aspects of the CMB and the temperature anisotropies in it. I will begin with the primary anisotropy in the CMB and describe the secondary fluctuations and their cosmological implications (§2.2.1 and §2.2.2). In §2.2.3 I will present a full derivation of the SZ effect, which is the leading secondary anisotropy in the CMB. I will discuss the cosmological and astrophysical significance of the SZ effect in §2.2.4.

2.1 THE COSMIC MICROWAVE BACKGROUND

The CMB is the relic radiation from Big Bang. The physics of the CMB is simple and it is a direct signature of the hot and dense phase of the early universe. Approximately $300,000$ years after the Big Bang, at a redshift of 1100, when the temperature of the universe was 3000 K, electrons and protons combined to form neutral hydrogen. This event is called the epoch of "recombination". Before recombination the photons and the electrons (baryons) were tightly coupled via Thompson scattering (the non-relativistic limit of Compton scattering is taken since the electrons are non-relativistic at a temperature of 3000 K), and the cosmological plasma was a coupled baryon-photon fluid (Peebles & Yu 1970). As a consequence of this tight coupling the baryon-photon fluid had a single bulk velocity. With the formation of neutral hydrogen, there was a decrease in the number density of free electrons (n_e). As a result of that, the scattering rate ($\Gamma = \sigma_T n_e v$) decreased and fell below the expansion rate (Hubble parameter) of the universe. This made the baryon-photon plasma fall out of equilibrium (also known as the decoupling of photons), and the photons free-streamed to

today's CMB sky. The epoch of recombination is called the "surface of last scattering" since that was the last time when photons were scattered off. In the next Section, I will give a simple description of the physics of recombination.

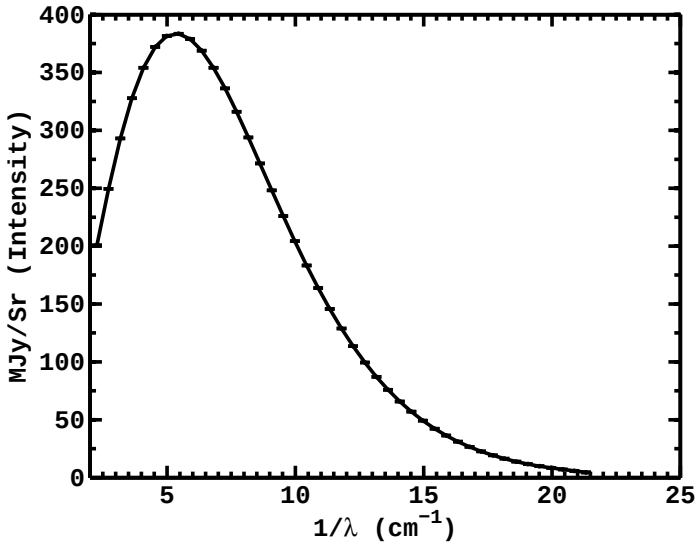

Figure 2.1: Blackbody spectrum from COBE. The data is taken from LAMBDA [1]. Data credit: Fixsen & Mather (2002) Courtesy: COBE science team and NASA

2.1.1 Physics of Recombination

From simple atomic physics we would expect recombination to happen at a redshift when the mean energy of the photons falls below the ionization energy of hydrogen (13.6 ev). Once that condition is satisfied, photons will not be able to photoionize hydrogen in the universe and there will not be free electrons to scatter the photons. However, the energy of the CMB photons is not uniform, and the black body distribution will have its high energy tail. Since the baryon-photon ratio (η) in the universe is $\approx 5 \times 10^{-10}$, the tiny fraction of the high energy photons within the tail of the distribution, will still be enough to photoionize hydrogen in the early universe. The exact temperature of recombination will depend on the ionization fraction (X), η, and the mean photon energy K_BT. If we assume a Maxwell-Boltzmann distribution $f(E) = n(2\pi m_e K_B T)^{-3/2} e^{-E/K_BT}$, of the baryonic species

(during recombination they are all non-relativistic), then we can write the following equation involving the number densities of the particles:

$$\frac{n_H}{n_p n_e} = \frac{g_H}{g_p g_e}\left(\frac{m_H}{m_p m_e}\right)^{3/2}\left(\frac{K_B T}{2\pi\hbar^2}\right)^{-3/2} exp\left(\frac{(m_p + m_e - m_H)\,c^2}{K_B T}\right)$$
$$= \left(\frac{m_e K_B T}{2\pi\hbar^2}\right)^{-3/2} \exp\left(\frac{Q}{K_B T}\right). \tag{2.1}$$

Equation 2.1 is called the Saha equation, where p, H, and e denote protons, neutral hydrogen, and electrons, respectively.

Using charge neutrality, we write $n_e = n_p$. The ionization fraction can be written as $n_H = (1 - X)n_p/X$. The baryon-photon ratio is given as $\eta = n_p/(Xn_\gamma)$. Using these substitutions we can write the Saha equation as

$$\frac{1 - X}{X^2} = \eta n_\gamma \left(\frac{m_e K_B T}{2\pi\hbar^2}\right)^{-3/2} \exp\left(\frac{Q}{K_B T}\right)$$
$$= 3.84\eta \left(\frac{K_B T}{m_e c^2}\right)^{3/2} \exp\left(\frac{Q}{K_B T}\right), \tag{2.2}$$

where we have used $n_\gamma = 0.243(K_B T/\hbar c)^3$. If we assume $X = 1/2$, then that gives a recombination temperature of 3740 K (Ryden 2002).

Note that recombination was not an instantaneous process. The decoupling of photons follows recombination due to the decrease of free electron density. If we equate the Thompson-scattering rate with the Hubble parameter (assuming matter domination) we get the following relation (Ryden 2002) $\Gamma(z) = X(z)(1+z)^3 n_{bary,0}\sigma_T c = 4.4\times10^{-21} s^{-1} X(z)(1+z)^3 = H(z) = 1.24\times10^{-18} s^{-1}(1+z)^{3/2}$. From the Saha equation we get the value of z_{dec} (redshift of decoupling) to be ≈ 1130 (Ryden 2002). However, not all the photons decoupled at this single redshift and there is an added complication related to the validity of Saha equation. The Saha equation is only valid at equilibrium. The reaction falls out of equilibrium as the scattering rate fall below the expansion rate. When these subtleties are taken into account, there appears a finite width of the surface of last scattering. The CMB is a perfect blackbody with a uniform temperature of $3740/1130 \approx 3$ K. The uniform temperature field of the CMB gives a snapshot of the smooth distribution of matter in the early universe. Figure 2.1 shows the blackbody spectrum of the CMB, as measured by COBE (Mather et al. 1990).

Although the CMB is extremely smooth, calculations of cosmological perturbation theory predict temperature fluctuations in the smooth background. With the discovery of the microwave background, efforts were taken to detect these temperature fluctuations. The temperature fluctuations in the CMB were proposed to have signatures of initial density perturbations in the early universe which ultimately lead to the growth of structures. The COBE satellite made a full-sky map of the temperature fluctuations in the CMB with an angular precision of 7 degrees (Smoot et al. 1992). The WMAP satellite measured these temperature fluctuations and the corresponding power spectrum with an angular resolution of 30 arcminutes (Bennett et al. 2003). In Fig. 2.2 the all sky temperature maps from COBE and WMAP are shown. The maps have been taken from Bennett et al. (1996) and Hinshaw et al. (2009). In the next Section, I will discuss the origin of the temperature fluctuations in the CMB and emphasize the importance of these fluctuations as cosmological probes.

2.2 ANISOTROPIES IN THE CMB

The fluctuations in the CMB can be categorized into two broad classes: primary and secondary. The primary fluctuations arise from density perturbations in the very early universe. The secondary fluctuations in the CMB arise due to its interaction with matter in the late universe. These fluctuations are the signatures of different physical mechanisms at different epochs of the evolutionary history of the universe, and they serve as tools to study the entire thermal history of the universe.

2.2.1 Primary Anisotropies

The primary fractional temperature fluctuation in the CMB as measured by COBE and WMAP is 10^{-5} and hence the physics is well described by linear perturbation theory. These fluctuations are the seeds of structure formation. They are generated by the quantum fluctuations in the scalar field driving inflation. The quantum fluctuations perturb the energy momentum tensor $T_{\mu\nu}$. The fluctuations in the energy momentum tensor perturbs the Ein-

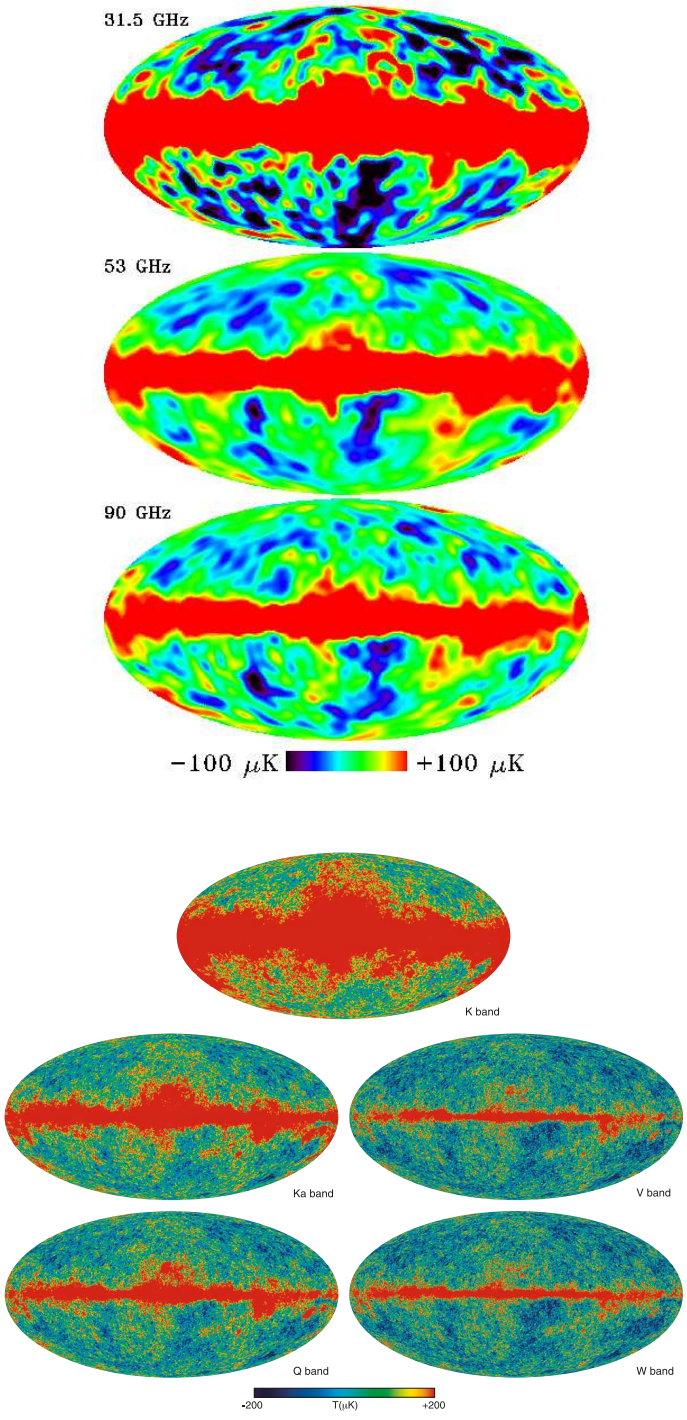

Figure 2.2: All sky temperature maps from COBE (top) and WMAP(bottom). The figures are taken from Bennett et al. (1996) (COBE) and Hinshaw et al. (2009) (WMAP). Courtesy: LAMBDA [1], WMAP Science team, and NASA. The maps show the improvement in angular resolution from COBE to WMAP.

stein tensor $G_{\mu\nu}$ via Einstein's field equation, which results in the fluctuations of the metric from an FRW cosmology. In a Newtonian scenario, the fluctuations in the metric resemble the fluctuations in the gravitational potential, and thus temperature fluctuations in the photon field arise due to inhomogeneity in the gravitational field, a phenomenon known as Sachs Wolfe effect (Sachs & Wolfe 1967). These fluctuations provide the initial conditions for the primary anisotropies seen in the CMB temperature field. The inflationary paradigm, which sets the initial conditions for temperature fluctuations in the CMB, generates fluctuations in a scale-independent manner. This means that the fluctuations in the gravitational potential are equal at all scales. See Appendix A for a discussion of scale invariance.

At the epoch of recombination the baryon-photon fluid is under the effect of gravity (dark matter potential wells) and with gravitational perturbations in the potential, acoustic oscillations are generated, where the radiation pressure of the baryon-photon fluid acts as the restoring force. See Appendix B for more discussions. The physics of the acoustic oscillations is simple. Due to the effect of gravity and pressure gradient, perturbations at or below the sound horizon scale at large scattering get compressed (due to gravity) and rarefied (due to pressure gradients) which account for photons getting hotter an colder. This illustrates the fact that if the baryon-photon fluid is at maximum compression at the time of photon decoupling , its energy density will be higher than average. Since $T \propto E^{1/4}$ this will make the photons intrinsically hotter on average. Conversely, if the baryon-photon fluid is under maximum expansion at decoupling, then the photons will be cooler than average. At large scale (small k; superhorizon) the solution represents the non-oscillatory limit (see Hu & Dodelson 2002 for a review), and we get the regular Sachs-Wolfe effect. There is also a Doppler anisotropy introduced in the photons due to the motion of the photons. The growth of perturbations in the early universe can be thought of as a forced-damped harmonic oscillator. The photon diffusion term and the finite width of the surface of last scattering are responsible for the damping of the acoustic peaks and troughs.

For the CMB radiation to be a blackbody, the distribution function at the position $\mathbf{x}$ is given by

$$f(\nu, \hat{n}, \mathbf{x}) = [\exp(h\nu/K_B T(\hat{\mathbf{n}}; \mathbf{x}) - 1]^{-1}. \tag{2.3}$$

For a description of the temperature fluctuation in the sky we want a harmonic description

of the field. This is written as

$$\Theta(\hat{\mathbf{n}}) = \frac{T(\hat{\mathbf{n}}) - \bar{T}}{\bar{T}} = \sum_{lm} \Theta_{lm} Y_{lm}(\hat{\mathbf{n}}). \tag{2.4}$$

We can write the temperature field at recombination as (Hu 2008)

$$\Theta(\hat{\mathbf{n}}) = \int dD \Theta(x) \delta(D - D_*), \tag{2.5}$$

where $D = \int dz/H(z)$, D_* is the distance, a CMB photon has traveled since recombination, and $\Theta(x) = \frac{T(x)-\bar{T}}{\bar{T}}$ is the spatial temperature fluctuation at recombination (see Hu 2008 for a review). The temperature fluctuation is written in Fourier modes as

$$\Theta(x) = \int \frac{d^3k}{(2\pi)^3} \Theta(k) e^{ik.x}, \tag{2.6}$$

and the two-point function is defined by the power spectrum of fluctuations as

$$\langle \Theta(k)^* \Theta(k' \rangle = (2\pi)^3 \delta(k - k') P(k). \tag{2.7}$$

Using Eq. 2.5 and 2.6 we have

$$\begin{aligned}
\Theta(\hat{\mathbf{n}}) &= \int dD \Theta(x) \delta(D - D_*) \\
&= \int dD \int \frac{d^3k}{(2\pi)^3} \Theta(k) e^{ik.x} \delta(D - D_*) \\
&= \int dD \delta(D - D_*) \int \frac{d^3k}{(2\pi)^3} \Theta(k) e^{ik.x} \\
&= \int \frac{d^3k}{(2\pi)^3} \Theta(k) e^{ik.D_* \hat{n}}.
\end{aligned} \tag{2.8}$$

The exponential term in Eq. 2.8 can be expanded in the following way (Hu 2008):

$$e^{ikD_* \hat{n}} = 4\pi \sum_{lm} i^l j_l(kD_*) Y^*_{lm}(\hat{k}) Y_{lm}(\hat{n}). \tag{2.9}$$

Using Eq. 2.4, 2.8 and 2.9 we can write,

$$\Theta_{lm} = \int \frac{d^3k}{(2\pi)^3} \Theta(k) 4\pi i^l j_l(kD_*) Y_{lm}(k). \tag{2.10}$$

Using Eq. 2.10 and 2.7, the two-point correlation function can be written as

$$\begin{aligned}\langle\Theta^*_{lm}\Theta_{l'm'}\rangle &= \delta_{ll'}\delta_{mm'}C_l \\ &= \int\int \frac{d^3k'}{(2\pi)^3}\frac{d^3k}{(2\pi)^3}P(k)(4\pi)^2(-i)^l(i)^{l'}j_l(kD_*)j_{l'}(k'D_*)Y^*_{lm}(k)Y_{l'm'}(k') \\ &= \delta_{ll'}\delta_{mm'}4\pi\int\frac{d\ln k}{(2\pi)^3}\Delta^2_T(k)j^2_l(kD_*), \end{aligned} \tag{2.11}$$

where $\Delta^2_T(k) = k^3P(k)$. This implies

$$C_l = 4\pi\int j^2_l(kD_*)\Delta^2_T(k)d\ln k. \tag{2.12}$$

For a slowly varying and nearly scale invariant power spectrum we can do the following approximation (Hu 2008).

$$C_l = 4\pi\Delta^2_T(k)\int j^2_l(kD_*)d\ln k. \tag{2.13}$$

The remaining integral, $\int j^2_l(x)d\ln x$, can be evaluated in closed form as $I = \frac{1}{2l(l+1)}$ (Hu 2008): This gives

$$C_l = \frac{2\pi}{l(l+1)}\Delta^2_T(l/D_*), \tag{2.14}$$

where the fluctuation is evaluated at the peak of the Bessel function ($l \sim kD_*$). Conventionally the temperature fluctuations at different angular scales are plotted according to Eq. 2.14. Eq. 2.14 is called the power spectrum of temperature fluctuations. Due to acoustic oscillations in the early universe the power spectrum will have acoustic peaks. Note that both the peaks and troughs in the perturbations will appear as peaks in the power spectrum since it represents the square of the amplitude of fluctuations.

Figure 2.3 gives the measurement of the angular power spectrum of fluctuations for a LCDM cosmology from WMAP5 with the best-fit theoretical model (Nolta et al. 2009). The first peak occurs at $l = 200$ corresponding to an angular scale of a degree in the sky. The structures in the power spectrum peaks have important cosmological consequence. Efforts to locate the first peak (at a scale of 1°) were undertaken by ground based experiments such as MAT, BOOMERANG, MAXIMA-1. Finally after combining the results with the WMAP experiment, we have precise measurements of the first five acoustic peaks. Fluctuations

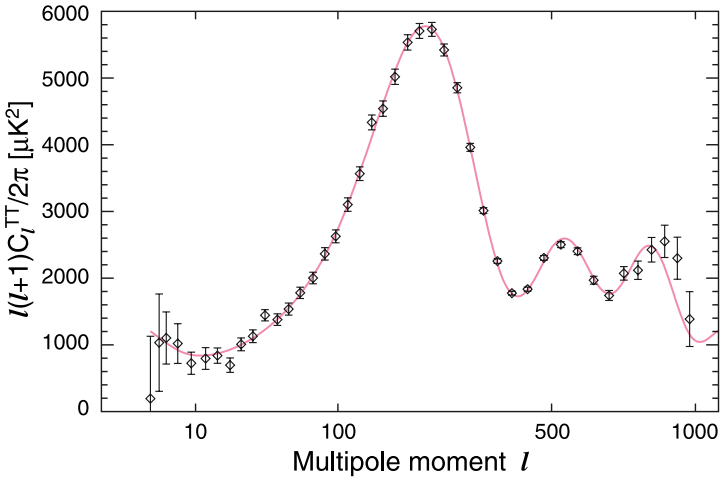

Figure 2.3: WMAP 5 year measurement of the angular power spectrum (Nolta et al. 2009). The solid line corresponds to the power spectrum with the best-fit cosmology. Courtesy: LAMBDA[1] and NASA. Data credit: WMAP Science team.

below a scale of $10^{'}$ are exponentially damped (Silk 1968) and has been confirmed by the CBI experiment (Padin et al. 2001).

The angular scale of the first peak is related to the geometry of the universe. The angular scale at which the first peak occurs, corresponds to the ratio of the sound horizon at last scattering to the angular diameter distance to last scattering. For a negatively curved universe the first peak would appear at a smaller angular scale than a degree (higher multipoles) and for a positively curved universe the first peak would appear to be at a higher angular scale (lower multipoles). However the angular scale of the peaks would also depend on the content of the universe since the angular diameter distance is a function of Ω_Λ and Ω_m. The determination of the first acoustic peak gave clear evidence of spatial flatness of the universe (Miller et al. 1999). The second peak is related to the baryon-photon ratio at the time of recombination. The baryon-photon ratio also determines the even-odd modulation of the peak amplitudes (Hu 2008). The precise measurement of the second peak gave limits on the baryon density (Spergel et al. 2007).

2.2.2 Secondary Anisotropies

The secondary fluctuations include all the temperature anisotropies that are generated after the epoch of recombination and decoupling (z = 1100) in the CMB. The secondary anisotropies in the CMB are

1. The integrated Sachs Wolfe (ISW) effect,
2. Ress-Sciama (RS) effect,
3. Gravitational lensing of the CMB,
4. Ostriker-Vishniac (OV) effect,
5. The kinetic Sunyaev Zeldovich (KSZ) effect, and
6. The thermal Sunyaev-Zeldovich (TSZ) effect. The first three are termed as gravitational secondaries and the last three are called scattering secondaries. The ISW, RS, and lensing effects are achromatic in nature, and the OV, KSZ, and TSZ effects have frequency variation.

2.2.2.1 ISW Effect After decoupling the universe expands, and the seeds of small anisotropies that are generated in the gravitational potential continue to grow as large scale structures in the universe. The ISW effect arises from the time varying component of the gravitational potential. When the universe is matter dominated as it is at the time of recombination and decoupling, the gravitational potential stays static. However at the epoch of radiation domination ($z \geq 10000$), and dark energy domination (z below 0.8) the gravitational potential becomes time varying. This can be shown from the Poisson equation. The growth of CDM perturbations in a flat universe is given by the following equation, (see Ryden 2002).

$$\frac{d^2\delta_k}{dt^2} + 2H\frac{d\delta_k}{dt} - (3/2)\Omega_m H^2 \delta_k = 0, \tag{2.15}$$

where terms being usual. The Poisson equation can be written as,

$$\nabla^2(\delta\phi) = 4\pi G\delta\bar{\rho}\delta, \tag{2.16}$$

where δ is the density perturbation, and ϕ is the gravitational potential. For matter domination we can solve the perturbation equation using a power law solution. This will give

an indicial equation of $3n(n-1)+4n-2=0$, where n is the power law index. This gives us a growing mode solution $\delta \propto t^{2/3}$. From Poisson equation we can write the potential at matter domination as $\phi \propto R^2\rho\delta \propto a^2a^{-3}t^{2/3}$. At matter domination $a \propto t^{2/3}$. This makes the potential to be time-independent. When the energy content of the universe is dominated by both matter and radiation (early universe), or dark energy and matter (as it is now), one can do a numerical calculation to show that the gravitational potential varies with time (see Dodelson 2002). The ISW effect becomes important at these two epochs. The photon undergoes redshift, and blueshift respectively while climbing up, and down, the potential well. For a time varying potential this could induce a net blueshift or a redshift to the photon which manifests as temperature anisotropy in the CMB. At the time of radiation domination this effect is termed as early ISW effect whereas at the onset of dark energy domination, we call it the late ISW effect.

The amplitude of the early ISW effect is very small and it occurs at lower angular scales. This is in marked difference with the late ISW effect which is dominant at larger angular scales. In the late ISW effect the potential decays over a longer amount of time (of the order of a Hubble time), and thus small scale anisotropies are washed out due to the traveling of photons through multiple peaks and troughs of the gravitational potential (see Aghanim, Majumdar, & Silk 2008 for a review of secondary effects). The ISW effect can be probed by observations of large scale structure. The ISW effect has been detected by several groups through cross-correlation of the CMB sky with galaxy survey data sets from SDSS, National Radio Astronomy Observatory (NRAO)- Very Large Array (VLA) Sky Survey (NVSS), 2-Micron All Sky Survey (2MASS) (e.g., Diego, Hansen, & Silk 2003; Boughn & Crittenden 2005; Fosalba & Gaztanaga 2004; Afshordi, Lin, & Sanderson 2005; Padmanabhan et al. 2005b, Ho et al. 2008; Giannantonio et al. 2008).

2.2.2.2 RS Effect The Ress-Scaima (RS) effect is the non-linear ISW effect, where the perturbation in the gravitational potential is considered beyond first order. If the photon-crossing time through the gravitational well is comparable to the evolution time of the gravitational potential there will be a non-zero contribution to the temperature anisotropy at small angular scales (Rees & Scaima 1968). This can also be true for an isolated collapsed

structure along the line of sight of the CMB (Birkinshaw & Gull 1983), where there could be a change in the gravitational potential of the collapsed structure due to its bulk motion (see Aghanim, Majumdar & Silk 2008 and references therein). This is known as the moving halo effect. Analytic, and numerical calculations show that the RS effect peaks at l between 100, and 300. The temperature fluctuation $\Delta T/T$ is between $10^{-6} - 10^{-7}$ (e.g., Seljak 1996a; Hu 2000; Cooray 2002a).

2.2.2.3 CMB Lensing As the CMB photons propagate from the surface of last scattering to $z = 0$, the primary fluctuations in the CMB get lensed by the intervening matter distribution (Blanchard & Schneider 1987). This effect is called the lensing of the CMB. With the effect of lensing, certain patches of the sky are magnified and demagnified. The effect would not have been present if the CMB would have been perfectly isotropic. For CMB lensing the important factor is not the absolute value of the light deflection, but the relative deflection compared to close by light rays (see Aghanim, Majumdar, & Silk 2008 for references). The deflection of an anisotropic temperature field results in transfer of power from higher angular scales to lower ones (Hu 2000). Weak lensing of the CMB does not correspond to any characteristic scale and its effect is seen at scales below an arcminute, where there is a modification in the CMB power spectrum due to transfer of power.

To understand the full significance of lensing, higher order correlations are also important (e.g., Bernardeau 1997; Zaldarriaga 2000; Cooray 2002c; Kesden, Cooray, & Kamionkowski 2003). The lensing effect in the CMB can couple the E and B modes of polarization in the CMB (see Aghanim, Majumdar, & Silk 2008 for references). The induced B mode polarization signal from CMB lensing would be an important source of confusion for detection of primordial gravity waves through B-mode polarization measurements (Kaplinghat, Knox, & Song 2003). There is evidence of detection of the lensing effect from cross-correlation with large scale structure data sets (Smith, Zahn, & Dore 2007; Hirata et al. 2008). Detection of CMB lensing is possible with arcminute scale microwave experiments like ACT through cross-correlation with large scale structure tracers and cross-correlation cosmography (Das & Spergel 2008).

2.2.2.4 OV Effect The Lyman-alpha resonance line of hydrogen at a wavelength of 1216 Å has been used to trace the source of neutral hydrogen through its absorption in quasar spectra (Gunn & Peterson 1965). The absence of the Gunn-Peterson effect in quasar spectra was the strongest suggestion for reionization of the universe after recombination. It is now believed that reionization occurred between a redshift of $7.0 \leq z \leq 20.0$ (see Aghanim, Majumdar, & Silk 2008 and references therein). Plausible sources for reionizing the universe are radiation from first generation stars (see Barkana & Loeb 2007 for a review). The CMB photons are scattered by the ionized electrons that generates scattering secondaries in the CMB. The velocity field of the scattering electrons induces Doppler shifts in the CMB photon distribution. The modulation of the velocity field occurs due to density contrast of the baryon distributions, and the spatial variations of ionization fractions. The OV effect occurs when the ionization fraction is homogeneous, and the anisotropies are generated by the fluctuations in the density field of the baryons (Ostriker & Vishniac 1986; Dodelson & Jubas 1995). The OV effect arises from the linear perturbation in the density field of the underlying baryon (electron) distribution. The effect is proportional to the square of the density contrast ($\propto \delta^2$) since the linear perturbation in the velocity field introduces the extra term in density (Scannapieco 2000; and references in Aghanim, Majumdar, & Silk 2008). The effect peaks at a scale of an arcminute with a characteristic amplitude of a μK (Zhang, Pen, & Trac 2004).

2.2.2.5 KSZ Effect The KSZ effect (Sunyaev & Zeldovich 1980; see Rephaeli 1995 for a review of SZ) is essentially the non-linear extension of the OV effect where the Doppler shift of the CMB photon arises due to the line of sight component of the bulk motion of collapsed structures such as clusters of galaxies. The KSZ effect can be used to measure cluster peculiar velocities from SZ experiments like ACT[3]. Measurements of peculiar velocities can be useful in constraining dark energy parameters (e.g., Bhattacharya & Kosowsky 2008). They can also be used to measure the large scale velocity fields of the universe. A combined measurement of velocity and density fields can be used to put constraint on theories of modified gravity through the Poisson equation (Bhattacharya et al. 2009 (in prep)).

2.2.2.6 TSZ Effect The TSZ effect (Sunyaev & Zeldovich 1972) is the inverse Compton scattering of the CMB photons from hot electrons present in galaxy clusters along the line of sight, and is the most prominent secondary fluctuation in the CMB. The change in intensity is proportional to the integrated electron pressure along the line of sight. In the non-relativistic limit the TSZ signal appears as a decrement in CMB intensity below 220 GHz and an increase at higher frequencies. The equivalent intensity difference manifests as a temperature difference in the CMB. A typical cluster of mass $10^{14}M_{\odot}$ induces a temperature distortion of about $\sim 100\mu K$. The TSZ effect is independent of redshift and hence is an important observational tool in cosmology (see Carlstrom, Holder, & Reese 2002 for a review). In the next Section, I will give a full derivation of the TSZ effect, and discuss how it can be used as a tool in cosmology.

2.2.3 Derivation of the SZ Effect

I start from the Boltzmann equation assuming an isotropic distribution of photons. Let $n(\omega)$ be the phase space density of photons and $f_e(P)$ be the phase space density of the electrons. I will assume non relativistic electrons followed by a Maxwellian distribution at temperature T_e. If $f_e(P)$ and $f_e(P_1)$ are the distribution functions of the electron before and after the scattering and $n(\omega)$ and $n(\omega_1)$ are the distribution functions of the photon before and after the scattering event then the Boltzmann equation for $n(\omega)$ is given as (Rybicki & Lightman 1985; see Dodelson 2002 also)

$$\frac{\partial n(\omega)}{\partial t} = c \int d^3P \int \frac{d\sigma}{d\Omega} d\Omega [f_e(P_1) n(\omega_1)(1 + n(\omega)) - f_e(P) n(\omega)(1 + n(\omega_1))], \tag{2.17}$$

where c is the speed of light and $d\sigma/d\Omega$ is the scattering cross-section. The scattering term is proportional to the scattering cross-section (which will be Thompson scattering cross-section if the energy of the electrons is much lower than the rest mass of the electrons), and the interaction term in the Lagrangian. The Compton scattering process can be written in terms of a two way process from the conservation of energy and momentum as

$$P + \omega \rightleftharpoons P_1 + \omega_1. \tag{2.18}$$

In the forward scattering, there is a creation of states P_1 and ω_1, and annihilation of states P and ω. I can write the forward scattering term as $(a^\dagger|n(\omega_1)\rangle)(a|n(\omega)\rangle)(b^\dagger|f_e(P_1)\rangle)(b|f_e(P)\rangle)$, where a, $a^\dagger$, b, and $b^\dagger$ are the bosonic and fermionic annihilation and creation operators respectively in the Fock representation. The backward scattering term will be creation of states P and ω and annihilation of states P_1 and ω_1 and would be proportional to $(a^\dagger|n(\omega)\rangle)(a|n(\omega_1)\rangle)(b^\dagger|f_e(P)\rangle)(b|f_e(P_1)\rangle)$. Using the eigenvalues for the operators, I get the entire matrix element for the forward scattering term as $(1+n(\omega_1))(1-f_e(P_1))f_e(P)n(\omega)$, and the backward scattering process as $(1+n(\omega))(1-f_e(P))f_e(P_1)n(\omega_1)$. For a dilute non-degenerate distribution of electrons, $1-f_e \approx 1$. With this approximation I can write the change in the photon phase-space density in the form given in Eq. 2.17.

I consider a small fractional energy transfer between the photons and the electrons. This enables me to expand $f_e(P_1)$ and $n(\omega_1)$ in terms of $f_e(P)$ and $n(\omega)$.

$$n(\omega_1) = n(\omega) + (\omega_1 - \omega)\frac{\partial n(\omega)}{\partial \omega} + 1/2(\omega_1 - \omega)^2 \frac{\partial^2 n(\omega)}{\partial \omega^2}, \tag{2.19}$$

$$f_e(E_1) = f_e(E) + (E_1 - E)\frac{\partial f_e(E)}{\partial E} + 1/2(E_1 - E)^2 \frac{\partial^2 f_e(E)}{\partial E^2}, \tag{2.20}$$

where $E_1 = P_1^2/2m_e$, $E = P^2/2m_e$, and m_e is the mass of the electron. I define the following variables,

$$\Delta = \frac{\hbar(\omega_1 - \omega)}{K_B T_e}, \tag{2.21}$$

$$x = \frac{\hbar\omega}{K_B T_e}. \tag{2.22}$$

K_B is Boltzmann constant and T_e is the temperature of the electrons. Using Eq. 2.19, 2.21, and 2.22 I get

$$n(\omega_1) = n(\omega) + \Delta n^{'} + \frac{\Delta^2}{2} n^{''}, \tag{2.23}$$

where the derivatives are with respect to x. For a Maxwellian distribution of electrons we can write $\partial f_e/\partial E = -(1/K_B T_e) f_e$, and $\partial^2 f_e/\partial E^2 = (1/(K_B T_e)^2) f_e$. Using Eq. 2.20, I get

$$f_e(E_1) = f_e(1 + \Delta + \Delta^2/2). \tag{2.24}$$

I can now use Eq. 2.17, 2.23, and 2.24 to get

$$\frac{\partial n}{\partial t} = c\int d^3P \int \frac{d\sigma}{d\Omega} d\Omega [f_e(E)(1+\Delta+\frac{\Delta^2}{2}) (n+\Delta n^{'}+\frac{\Delta^2 n^{''}}{2})(1+n) - f_e(E)n(1+n+\Delta n^{'}+\frac{\Delta^2 n^{''}}{2})]. \quad (2.25)$$

Keeping second order terms in Δ, I get

$$\frac{\partial n}{\partial t} = c(n^{'}+n(1+n))\int\int d^3P \frac{d\sigma}{d\Omega} d\Omega f_e \Delta + c\left(\frac{n^{''}}{2}+n^{'}(1+n)+\frac{n(1+n)}{2}\right)\int\int d^3P \frac{d\sigma}{d\Omega} d\Omega f_e \Delta^2. \quad (2.26)$$

Equation 2.26 is the Fokker-Plank expansion of the Boltzmann equation in orders of the energy transfer. The term involving Δ^2 is the random walk term and the term involving Δ is called the secular term.

To evaluate the integral, I need to know the energy transfer Δ. I evaluate Δ by applying the energy momentum conservation relations. Let the initial and final 4-momentum of the photon be $\bar{P_\gamma} = (1,\bar{n})\hbar\omega/c$ and $\bar{P_{\gamma 1}} = (1,\bar{n_1})\hbar\omega_1/c$, and the initial and final momentum of the electron be $\bar{P_e} = (E/c, P)$ and $\bar{P_{e1}} = (E_1/c, P_1)$, where $\bar{n}$ and $\bar{n_1}$ are the unit direction vectors before and after the scattering event. Now applying the conservation of 4-momentum I get

$$|P_{e1}|^2 = |P_e + P_\gamma - P_{\gamma 1}|^2. \quad (2.27)$$

This gives

$$\frac{E_1^2}{c^2} - P_1^2 = \frac{E^2}{c^2} - P^2 + 2\hbar\omega\frac{E}{c^2} - \frac{2P.n\hbar\omega}{c} - \frac{2\hbar^2\omega_1\omega}{c^2}(1-n.n_1) - 2\hbar\omega_1\frac{E}{c^2} + \frac{2P.n_1\hbar\omega}{c}. \quad (2.28)$$

Here I have explicitly used the fact that the 4-momentum of the photon is zero since it does not have a rest mass. Now using Eq. 2.21, I can write

$$\omega_1 = \frac{K_B T_e \Delta}{\hbar} + \omega. \quad (2.29)$$

Using Eq. 2.29, I can write Eq. 2.28 as

$$\frac{E\hbar\omega}{c} - \hbar\omega P.n = \frac{\hbar^2\omega}{c}(1-n.n_1)\left(\omega+\frac{K_B T_e\Delta}{\hbar}\right) + \frac{E\hbar}{c}\left(\omega+\frac{K_B T_e\Delta}{\hbar}\right) - \hbar P.n_1\left(\omega+\frac{\Delta K_B T_e}{\hbar}\right). \quad (2.30)$$

Using the expression for $x = \hbar\omega/(K_B T_e)$, I have

$$\Delta = \frac{xp(n_1 - n) - \frac{x^2 K_B T_e}{c}(1 - n.n_1)}{E/c - P.n_1 + xK_B T_e(1 - n, n_1)}. \tag{2.31}$$

For non-relativistic electrons $E = m_e c^2$, and thus I can write

$$\Delta = \frac{x.p(n_1 - n)}{m_e c} + O(K_B T_e/m_e c^2). \tag{2.32}$$

I will now evaluate the integral involving the term Δ^2 in Eq. 2.26. Let,

$$I_2 = \int d^3P f_e \Delta^2 \int \frac{d\sigma}{d\Omega} d\Omega. \tag{2.33}$$

Let χ be the angle between P and $(n_1 - n)$ and $d^3P = P^2 dP d\Omega^{'}$. If I choose χ to be the polar angle in the $\Omega^{'}$ integral and if n_1 lies along the polar axis in the Ω integral, I can write I_2 as a product of three integrals (Rybicki & Lightman 1985) given as

$$\begin{aligned} I_2 &= \frac{n_e x^2}{(m_e c)^2} (2\pi m_e K_B T_e)^{-3/2} \int P^4 \exp\left(\frac{-P^2}{2m_e K_B T_e}\right) dP \int\int \cos^2\chi \sin\chi d\chi d\phi^{'} \\ &\int\int \frac{3\sigma_T}{8\pi}(1 + \cos^2\theta)(1 - \cos\theta)\sin\theta d\theta d\phi, \end{aligned} \tag{2.34}$$

where $d\sigma/d\Omega = (3\sigma_T/(16\pi))(1+\cos^2\theta)$ (Rybicki & Lightman 1985) and σ_T is the Thompson cross section. The $(1 - \cos\theta)$ factor comes from the $(n_1 - n)$ term. After evaluating the three integrals, I get

$$\begin{aligned} I_2 &= \frac{n_e x^2}{(m_e c)^2} (2\pi m_e K_B T_e)^{-3/2} \left[(3/4)(2m_e K_B T_e)^{3/2} m_e K_B T_e \pi^{1/2}\right] (4\pi/3)(2\sigma_T) \\ &= \frac{2\sigma_T K_B T_e n_e x^2}{m_e c^2}. \end{aligned} \tag{2.35}$$

My next step involves evaluating the integral with the secular term in the Fokker-Planck equation. This can be achieved in a similar way, but I will adopt a simpler method for evaluating the integral using the photon number conservation. Since n is the photon phase space density and x is proportional to the momentum of the photons, than from conservation of photon number I have,

$$\frac{d}{dt}\int n x^2 dx = 0 = \int \frac{\partial n}{\partial t} x^2 dx. \tag{2.36}$$

Now

$$\frac{d}{dt}\int nx^2dx = -\int \frac{\partial}{\partial x}(x^2j(x))dx, \tag{2.37}$$

Eq. 2.37 implies that the change in total flux arises only from flux through the boundaries. Here $j(x)$ is a function of x only. This comes from the continuity equation where the $x^2j(x)$ term is the equivalent of current density. From Eq. 2.36 and 2.37 I have

$$\left(\frac{\partial n}{\partial t}\right)x^2 = -\frac{\partial}{\partial x}(x^2j(x)). \tag{2.38}$$

I need to find the functional form of $j(x)$. According to Eq. 2.26, I have

$$\frac{\partial n}{\partial t} = C_1(x)n^{''} + C_2(x,n)n^{'} + C_3(n,x), \tag{2.39}$$

where C_1, C_2 and C_3 are the coefficients to be determined. Comparing Eq. 2.39 and 2.26, I know that $j(x)$ should have a term involving $n^{'}$ with coefficients independent of n. So the most general form of $j(x)$ can be written as

$$j(x) = g(x)(n^{'} + h(n,x)), \tag{2.40}$$

where h and g are two functions to be determined. The photons follow the Bose-Einstein distribution. This gives

$$n = \frac{1}{e^{x+\alpha}-1} \tag{2.41}$$

$$\frac{\partial n}{\partial x} = -n(n+1), \tag{2.42}$$

where α is the chemical potential. I can match the boundary condition for an equilibrium distribution and this will give $\partial n/\partial t = 0$. Now, $\partial n/\partial t = 0$ will require the current density to be a constant (Rybicki & Lightman 1985), but that can be achieved only by assuming $j(x) = 0$, otherwise the current flux will blow up. Thus using Eq. 2.40, I have

$$n^{'} = -h(n,x)$$

$$h(n,x) = n(n+1). \tag{2.43}$$

Using Eq. 2.38 and 2.40 we have

$$\frac{\partial n}{\partial t} = -(g^{'}n^{'} + gn^{''} + h^{'}g + g^{'}h + 2n^{'}g/x + 2hg/x), \tag{2.44}$$

where the primes are derivatives with respect to x. Comparing Eq. 2.26, 2.39, and 2.44, I have

$$\frac{c}{2}I_2 = -g(x)$$
$$g(x) = -\frac{cx^2 n_e \sigma_T K_B T_e}{m_e c^2}. \tag{2.45}$$

Using Eq. 2.43 and 2.45, I get the full form of $j(x)$ as

$$j(x) = -cx^2 n_e \sigma_T \left(\frac{K_B T_e}{m_e c^2}\right)(n^{'} + n(n+1)). \tag{2.46}$$

Using the form of j(x) in Eq. 2.38, I get the following equation :

$$\frac{\partial n}{\partial t} = (c n_e \sigma_T)\left(\frac{K_B T_e}{m_e c^2}\right)\frac{1}{x^2}\frac{\partial}{\partial x}\left(x^4(n^{'} + n + n^2)\right). \tag{2.47}$$

Equation 2.47 is known as the Kompaneets equation (Kompaneets 1957) which is the non relativistic approximation of the Boltzmann equation with small energy transfers. I will now do a transformation of variable which will involve in going from the electron temperature to the temperature of radiation (Zeldovich & Sunyaev 1969). Let $y = (\hbar\omega)/(K_B T_r)$, where T_r is the temperature of the radiation field. For the present case this will correspond to the CMB temperature of 2.73 K. Changing variables from x to y gives the Kompaneets equation as follows (Rephaeli 1995),

$$\frac{\partial n}{\partial t} = (c n_e \sigma_T)\left(\frac{K_B T_e}{m_e c^2}\right)\frac{1}{y^2}\frac{T_r}{T_e}\frac{\partial}{\partial y}\left(y^4\left(n^{'}\frac{T_e}{T_r} + n + n^2\right)\right), \tag{2.48}$$

where the derivatives are taken with respect to y now.

If the temperature of the electrons is large compared to the temperature of radiation, which is the case for cluster X-ray gas (kev electrons) with reference to the CMB (mev photons), then the first term in Eq. 2.48 dominates, and the Kompaneets equation takes the following form (Zeldovich & Sunyaev 1969, Rephaeli 1995)

$$\frac{\partial n}{\partial t} = y n_e \sigma_T \frac{K_B T_e}{m_e c}\left(y\frac{\partial^2 n}{\partial y^2} + 4\frac{\partial n}{\partial y}\right). \tag{2.49}$$

In the limit of weak scattering, I can perturbatively expand the photon distribution function in orders of y with respect to the equilibrium distribution function. To first approximation this will enable me to write the distribution function as of purely Planckian nature with no

chemical potential. Using this distribution function for n given as, $n = 1/(e^y - 1), \partial n/\partial y = -e^y/(e^y - 1)^2$, and $\partial^2 n/\partial y^2 = 2e^y/(e^y - 1)^3 - e^y/(e^y - 1)^2$, I have Eq. 2.49 written as

$$\frac{\partial n}{\partial t} = n_e T_e \frac{K_B \sigma_T}{m_e c} \frac{y e^y}{(e^y - 1)^2} \left(\frac{y(e^y + 1)}{(e^y - 1)} - 4 \right). \tag{2.50}$$

Now the intensity of the photon distribution is given as

$$I = \frac{2h\nu^3}{c^2(e^y - 1)} = i_0 y^3 n, \tag{2.51}$$

where $i_0 = 2\frac{(K_B T_r)^3}{(hc)^2}$. Using Eq. 2.50 and 2.51, I get the change in the intensity of the photon distribution due to the up scattering process:

$$\begin{aligned} \Delta I = \int i_0 y^3 \frac{\partial n}{\partial t} \frac{dl}{c} &= \int n_e T_e \frac{K_B \sigma_T}{m_e c^2} \frac{y^4 e^y}{(e^y - 1)^2} \left(\frac{y(e^y + 1)}{(e^y - 1)} - 4 \right) dl \\ &= i_0 G(y) \int n_e T_e \frac{K_B \sigma_T}{m_e c^2} dl = i_0 G(y) Y. \end{aligned} \tag{2.52}$$

The above integral is done along the line of sight of the cluster and Y is defined as the Compton Y parameter and $G(y)$ is the spectral distortion. The Compton Y parameter is designated by "y" in the literature and so I will now use the notation "y" to denote the Compton y parameter. For clarity I will denote the dimensionless parameter y by x (as popularly done in the literature), such that $x = \hbar\omega/(K_B T_r) = \hbar\omega/(K_B T_{CMB}) = h\nu/(K_B T_{CMB})$. So for an inverse Compton scattering of the CMB photons by non relativistic electrons in clusters, I get a spectral distortion in the CMB given by the function $G(x)$ such that

$$G(x) = \frac{x^4 e^x}{(e^x - 1)^2} \left(\frac{x(e^x + 1)}{(e^x - 1)} - 4 \right), \tag{2.53}$$

where $x = \hbar\omega/(K T_{CMB})$. The change in intensity is proportional to the product of the spectral distortion and the y parameter which is an integrated line of sight pressure of the cluster gas (Sunyaev & Zeldovich 1972) and is given by

$$y = \frac{K_B \sigma_T}{m_e c^2} \int n_e T_e dl, \tag{2.54}$$

where n_e and T_e are the number density and temperature of the electron gas in the cluster, and K_B, σ_T, m_e, and c are Boltzmann constant, Thomson scattering cross section, mass of the

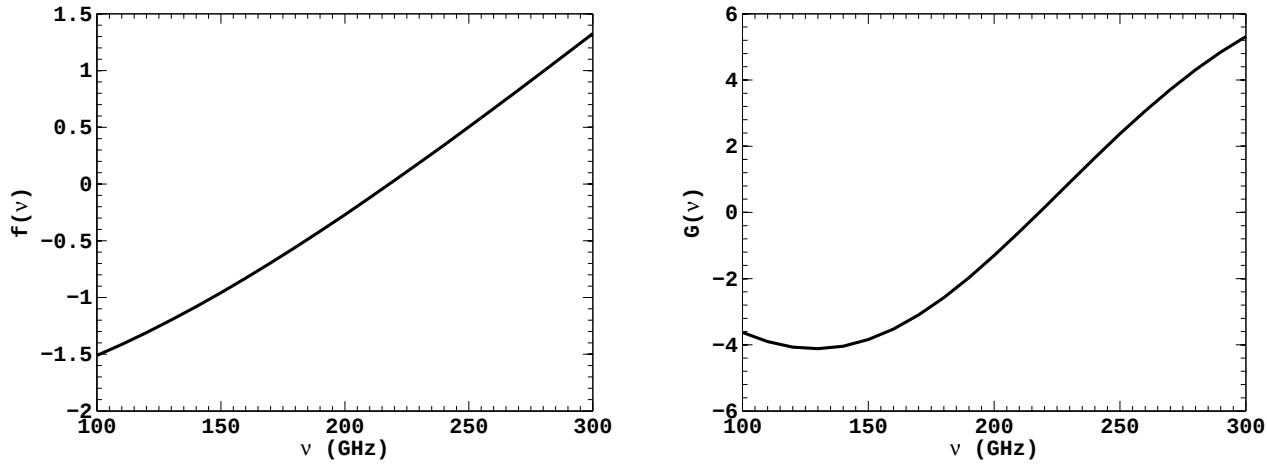

Figure 2.4: Frequency variation of the two functions f(ν)(Eq. 2.57) and G(ν) (Eq. 2.53) where $\nu = K_B T_{CMB} x/h$

electron, and speed of light respectively. Now the change in intensity can be characterized as a temperature change in the CMB. I can write the following transformation between intensity and temperature.

$$\Delta I = \frac{2h\nu^3}{c^2} \frac{e^x}{(e^x-1)^2} \frac{h\nu}{K_B T_{CMB}^2} \Delta T. \tag{2.55}$$

Using Eq. 2.55, 2.53, and 2.52 I get

$$\Delta T = T_{CMB} y f(x), \tag{2.56}$$

where

$$f(x) = \left(\frac{x(e^x+1)}{(e^x-1)} - 4 \right). \tag{2.57}$$

In Fig. 2.4 the functional dependence of G(x) and f(x) on frequency are shown for a fixed CMB temperature of 2.73 K. At 220 GHz the functions become zero. This frequency is defined as the null frequency of the SZ effect. Below the null frequency we see a decrement in intensity and above the null frequency we see an enhancement in the intensity. This manifests as hot and cold spots in the CMB. Note that the SZ distortion is a spectral distortion and

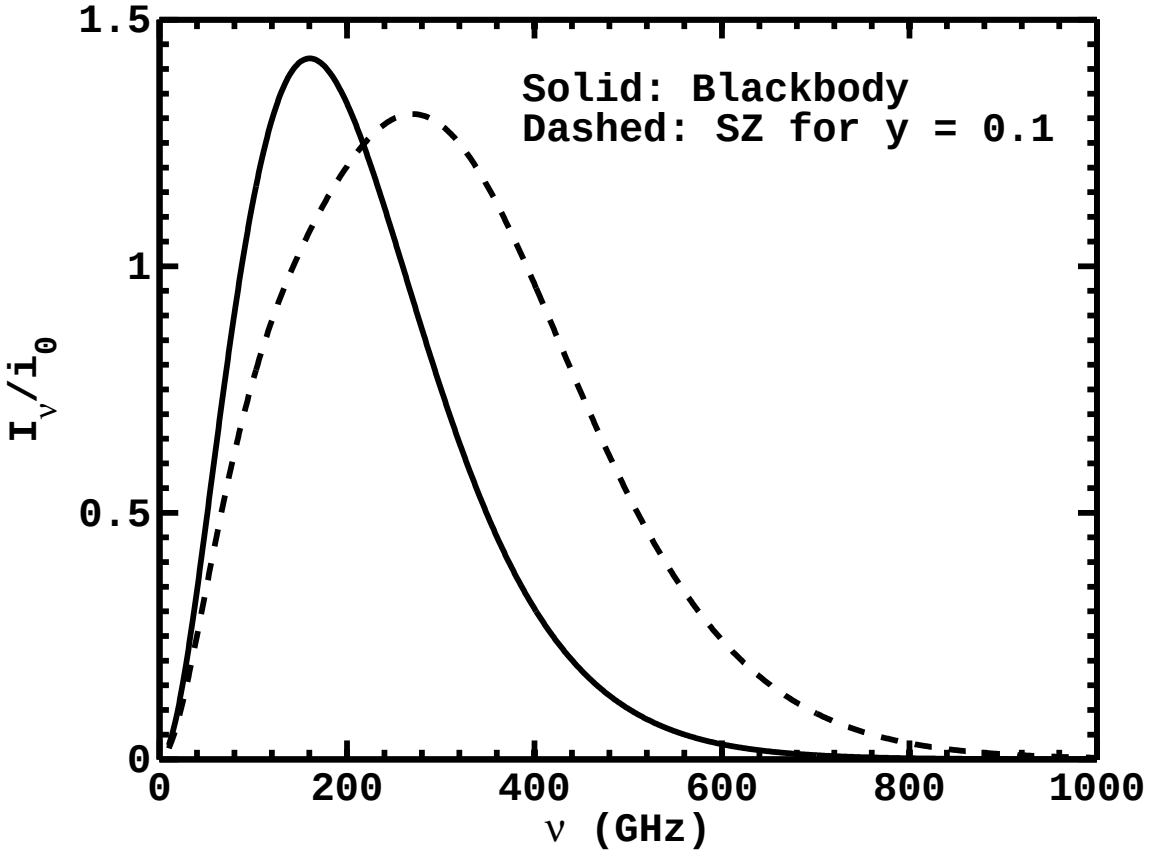

Figure 2.5: SZ spectrum for a Compton y parameter of 0.1. The reference blackbody spectrum is plotted in solid to show the spectral distortion where $i_0 = 2.7 \times 10^{-15}$ ergs/cm^2/sec/Hz/Steradian. The typical y parameter for a galaxy cluster is 10^{-4}. At 220 GHz we have the null or the cross-over frequency. The null frequency is a function of the blackbody temperature only (for the non-relativistic case), and is at 220 GHz for a 2.73 K blackbody. The null frequency varies and depends on cluster temperature, once we incorporate the relativistic corrections. In Eq. 2.31 we have neglected terms of $O(K_B T_e/m_e c^2)$. The null frequency varies accordingly.

so there is a departure from the blackbody spectrum. In Fig. 2.5 the SZ spectrum for a Compton y parameter of 0.1 is shown with reference to the blackbody spectrum.

The TSZ effect arises from the random thermal motion of the electrons. If there is a finite velocity of the cluster in the CMB frame there will be an additional Doppler term. This Doppler anisotropy is called the KSZ distortion. The KSZ distortion is easy to calculate. Using a relativistic transformation, I can write $\nu^{'} = \nu(1-\beta)\gamma$, where $\gamma = 1/\sqrt{(}1-\beta^2)$ and $\beta = v/c$, where v is the peculiar velocity of the cluster along the line of sight. For a small β, I can write $\Delta T = -T\beta\tau$, (Sunyaev & Zeldovich 1980) where $\tau = \sigma_T \int n_e dl$, is the optical depth of the cluster. The change in intensity due to the kinetic SZ effect can be obtained through Eq. 2.55. Substituting for ΔT in Eq. 2.55, I get the change in intensity due to KSZ effect as,

$$\Delta I = -i_0 \frac{x^4 e^x}{(e^x-1)^2} \frac{v\sigma_T}{c} \int n_e dl. \tag{2.58}$$

Note that the kinetic SZ effect comes as a net positive or negative effect depending on the direction of the peculiar velocity of the cluster with respect to the CMB frame. Unlike the thermal SZ effect the kinetic SZ effect does not undergo any spectral distortion and is a pure blackbody.

2.2.4 Cosmology with the SZ Effect

In recent years the SZ effect has become a useful tool in cosmology. Below, I give a brief description on some of the cosmological uses of the SZ effect.

2.2.4.1 Distance Measurements The SZ effect can be used to determine distances with combined X-ray observations. As shown in the previous Section, the SZ flux is given as

$$\Delta T_{SZE} \propto \int dl n_e T_e, \tag{2.59}$$

where terms being usual. The X-ray flux is given as

$$S_x = \int dl n_e^2 \Lambda_{eH}, \tag{2.60}$$

where Λ_{eH} is the X-ray cooling function. We further substitute $dl = D_A d\zeta$, where D_A is the angular diameter distance. Substituting for n_e from Eq. 2.59 and 2.60, we get the approximate angular diameter distance as follows:

$$D_A \propto \frac{(\Delta T_0)^2 \Lambda_{eH0}}{S_{x0} T_{e0}^2 \theta_c}, \tag{2.61}$$

where the integral is evaluated along the line of sight through the center of the cluster.

θ_c is the characteristic angular scale of the cluster. The characteristic scale in the plane of the sky, θ_{sky}, is measured and this serves as an observational proxy for θ_c. With the assumption of spherical symmetry the ratio between the two quantities is assumed to be unity. The second assumption relies on the clumping factor $C \equiv \frac{\langle n_e^2 \rangle^{1/2}}{\langle n_e \rangle}$ being close to one too. This assumption is violated with the presence of cluster substructures. The measurement of the angular diameter distance as a function of redshifts can be used to measure distances (see Carlstrom, Holder, & Reese 2002 for more discussion). With this technique distances can be measured to high redshifts directly and it is completely independent of other techniques. Presently the value of Hubble constant measured from combined SZ and X-ray techniques using data from *Chandra*, the Owens Valley Radio Observatory (OVRO), and Berkeley-Illinois-Maryland-Association (BIMA) interferometric array is $H_0 = 76.9^{3.9}_{-3.4}$ kms^{-1} for a LCDM cosmology (Bonamente et al. 2006). There is a 12% systematic uncertainty associated with the measurement of the Hubble constant.

2.2.4.2 Gas Mass Fraction Measurement The intercluster medium (ICM) contains most of the baryonic mass of the cluster in the form of hot X-ray gas (White et al. 1993). Measuring the gas mass fraction f_g in a cluster is a reasonable estimate of the baryonic mass in the cluster and the universal baryon fraction. A measurement of the baryon fraction gives an estimate of Ω_m with a known value of Ω_b, where Ω_m and Ω_b are the matter density and baryon density of the universe. The gas mass is directly measured by SZ observations. If the total gravitating mass is M and the electron temperature is T_e then we can either estimate the total mass (for e.g., from lensing observations) or assume hydrostatic equilibrium and estimate T_e to get the gas mass fraction given by the ratio $\Delta T_{SZ}/T_e^2$, where ΔT_{SZ} is the observed SZ decrement or increment. Laroque et al. (2006) determined $f_g = 0.116 \pm$

$0.005^{0.009}_{-0.016}$, using data from OVRO and BIMA. The uncertainties in the measurement are statistical, followed by systematics at 68% confidence.

2.2.4.3 Cluster Cosmology The SZ effect serves as a potential tool for detecting large samples of galaxy clusters. Since the number density of clusters is a sensitive function of the underlying cosmology, this enables us to do cosmology with galaxy clusters. See Appendix C for more discussion. For example, a higher Ω_m universe will predict less clusters at high redshift compared to lower density universe. The cluster number density is also a sensitive probe of the dark energy parameters (e.g., Mohr 2005). One of the important aspects of SZ cluster surveys is related to the minimum mass limit of the survey. The mass range to which a survey is sensitive is determined by the beam size and sensitivity of the instrument (see Carlstrom, Holder, & Reese 2002). This sets a minimum threshold mass for a flux limit survey. The mass selection function is relatively uniform (within a factor of 2-3) which makes SZ a more robust observational tool for fulfilling the completeness criterion compared to X-rays. Through dedicated SZ surveys like ACT and SPT, cluster number counts can be observed as a function of redshift. With a large sample of clusters there can be direct measurements of redshift evolution of cluster number density. This can in principle constrain cosmological parameters. Although to do precision cosmology the cluster mass needs to be estimated with better precision. Otherwise there will be systematic bias in measurements of cosmological parameters due to the inaccuracy of cluster mass measurements. Francis, Bean, & Kosowsky (2005) show that a 10% systematic bias in mass measurements of galaxy cluster can incorporate uncertainties that are greater than 1σ level statistical errors. Nagai (2006) shows from numerical simulation that there exists a tight correlation between integrated SZ flux from clusters and their corresponding mass which favors the completeness criterion described above.

The other technique for detecting clusters is through X-ray observations. The current constraint on cosmological parameters from clusters detected through X-ray observations is 20% for dark energy parameters (Vikhlinin et al. 2009). The two methods have relative pros and cons. Since the X-ray flux suffers from cosmological dimming where as the SZ flux is redshift independent, SZ is a better probe for detecting clusters beyond redshift

1.0. Also a large region of the sky needs to be observed to obtain a statistically significant sample to do cluster cosmology. Since X-ray measurements are much more expensive than SZ observations, it is not possible to obtain a large sample of clusters with X-ray measurements. The greatest disadvantage of SZ measurements is confusion noise which can lead to a null detection or a false positive detection. The confusion noise and astronomical contamination can be disentangled by multi frequency observations (Carlstrom, Holder, & Reese 2002). Recently Staniszewski et al. (2008) detected four galaxy clusters with SPT by observing 40 square degrees of the southern sky in 95, 159 and 225 GHz. Two of these clusters are at redshift 0.4. The other two clusters are at redshift ≥ 0.8. Three of these four clusters are first discovered through SZ observations. Also Hincks et al. (2009) detected ten clusters with ACT of which two are new cluster candidates. Since clusters probe the highest peaks of the density field, they can also be used to study cosmological initial conditions. With Gaussian initial conditions there is a definite prediction of the peak statistics. An observed excess of high peaks should be a signature of non-Gaussianity (Benson, Reichardt, & Kamionkowski 2001). However there will be contribution from local non-Gaussianity which can confuse the primordial non-Gaussian signatures.

2.2.4.4 Cluster Peculiar Velocities The KSZ effect is also a powerful tool for cosmology since it is the only known way to measure large scale velocity fields. This provides an opportunity to constrain modified gravity theories with a combined measurement of the density and velocity fields. However to obtain an accurate peculiar velocity of galaxy clusters to the level of precision cosmology, careful multifrequency observations are required to separate it from the thermal SZ and primary CMB signal. The first limit on cluster peculiar velocities from KSZ measurements was provided by Holzapfel et al. (1997). With combined SZ and X-ray data (Sunyaev-Zeldovich Infrared Experiment (SUZIE) and ROentgen SATellite (ROSAT)) they measured the peculiar velocities for nearby clusters Abell 2163 ($v_{pec} = 490^{+1370}_{-880}$, z = 0.202) and Abell 1689 ($v_{pec} = 170^{+815}_{-630}$, z =0.183). The spectrum of KSZ is degenerate with the CMB and it is intrinsically weak in nature. This makes the determination of peculiar velocity from clusters extremely difficult. However the mean peculiar velocity on large scales from large sample of clusters is still an interesting route for

measuring velocity fields. The uncertainty in Planck's cluster peculiar velocities is expected to be between 500-1000 Km/Sec (Aghanim, Gorski, & Puget 2001). With sufficiently large number of cluster peculiar velocities (of the order of thousands), this velocity error could still be sufficient to obtain optimistic constraints on dark energy parameters (Bhattacharya & Kosowsky 2008). However the current status of KSZ is not promising and constraints are to come from better observations in future.

2.2.4.5 Small Angle SZ In the previous Sections, I discussed the SZ effect from virialized gas in galaxy clusters. However there will be small scale astrophysical effects that can produce SZ distortions in the CMB (see references in Chapter 1). For the current work we have estimated the SZ distortion due to energy feedback from active galaxies. In the next Chapter, I will describe the importance of AGN feedback in theories of galaxy formation and discuss about how the SZ effect can be used as an effective probe of this process.

3.0 FEEDBACK FROM ACTIVE GALACTIC NUCLEI

In this Chapter, I will discuss the importance of AGN feedback and its role on structure formation. In §3.1 I will describe the observational and theoretical evidences of the role of AGN feedback on evolution and growth of structures. In §3.2 and 3.3 I will give a brief description of the possible ways for probing AGN feedback with X-ray, radio, and optical observations. In §3.4 I will give a brief description of the current theoretical models of AGN feedback. In §3.5 I will discuss how we can use the SZ effect as a new tool to probe feedback energy from AGNs.

3.1 ROLE OF AGN FEEDBACK ON STUCTURE FORMATION

3.1.1 The Cooling Flow Problem

One of the hallmarks of X-ray astronomy lies in detecting clusters via the hot X-ray gas present in the ICM. The first clusters detected in this way were the Perseus and Coma clusters by the Uhuru satellite (Giacconi et al. 1971; Gursky et al. 1971; Forman et al. 1972). Around 40 clusters were identified as X-ray sources by the mid 1970's (Gursky & Schwartz 1977). Clusters are the largest virialized objects in the universe with masses between $10^{14} - 10^{15} M_{\odot}$. The total gas fraction in clusters is about 16% with about 13% in the ICM and 3% in galaxies. The rest of the mass consists of dark matter. The gas densities at the center of galaxy clusters could be as high as 10^{-1} cm^{-3} to 10^{-3} cm^{-3}, which is different from the cosmic baryon density of 10^{-8} cm^{-3}. The virial radius of a cluster is defined as the radius within which the mean density of the cluster is 200 times the critical density

($9.4 \times 10^{-30} gms/cm^{-3}$) of the universe. The gas of the cluster is heated by gravitational infall to temperatures between 1-15 keV (see Peterson & Fabian 2006 for a review). This comes from the simple assumption of virial equilibrium of $K_B T \simeq GMm_p/R_v$, where M is the mass of the cluster, R_v is the viral radius ($\simeq 1Mpc$), m_p is mass of proton, G is the gravitational constant, K_B is Boltzmann constant, and T is the temperature of the cluster. The total X-ray luminosity in galaxy clusters range from 10^{43} ergs s^{-1} to 10^{46} ergs s^{-1} (see Peterson & Fabian 2006 for references).

Some of the gas then cools to form stars and the cooling time of the gas is given as $t_{cool} \propto T^{\alpha}/n_e$ where T is the temperature of the gas and n_e is the gas density (see Fabian 1994 for a review of cooling flows). This comes from the fact that $t_{cool} = E/(dE/dt) = K_B T/n_e \Lambda(T)$, where $\Lambda(T)$ is the cooling function (see Peterson & Fabian 2006; Sutherland & Dopita 1993). The exponent α will depend on the emission mechanisms assumed. The intracluster gas is densest at the core of the cluster which makes the cooling time at the core of the cluster to be the shortest. The emission from gas in clusters is mainly due to thermal Bremsstrahlung process (e.g., Sarazin 1988), and the X-ray luminosity of the radiation is given as $L_x \propto n_e^2 T^{1/2} R_v^3$ where terms are same as defined above. The other emission mechanisms are bound-free emission and two-photon emission. Several other line emissions follow the continuum radiation (Peterson & Fabian 2006 and references therein). To calculate the X-ray cooling function and the resulting cooling time, an integration of the energy weighted emission processes is performed (Sutherland & Dopita 1993). Since the gas density is highest at the center, the X-ray surface brightness at the cluster center tends to be strongly peaked too. The radiative cooling due to this emission would lead to a subsonic inflow of gas to maintain the pressure equilibrium. This will lead to a mass deposition rate of several hundreds of $M_{\odot}$/yr of cold gas in the cluster center. This is known as the cooling flow in cluster centers, and clusters that have cooling flows are called cool core clusters. However recent Chandra and X-MM-Newton observations have shown significant departure from the standard cooling flow picture (see Peterson & Fabian 2006 for references). The spectroscopically determined mass deposition rate is found to be few tens of $M_{\odot}$/yr (Voigt & Fabian 2004) which is in sharp contrast to the expected cooling flows in galaxy clusters. These observations suggested the presence of some other mechanisms that could be a viable

source for reducing the mass dropout due to cooling.

3.1.2 The $L_X - T$ Relation

If we assume the dominant emission mechanism in clusters to be thermal Bremsstrahlung, then the X-ray luminosity is given as, $L_x \propto n_e^2 T^{1/2} R_v^3$. For a self similar model (Gravitational infall) in a virialized cluster ($T \propto M/R_v \propto R_v^2$) we have $L_x \propto T^2$ (Kaiser 1986). However observations show that $L_x \propto T^3$ within the temperature range of 2-8 keV (e.g., Arnaud & Evrard 1999; Helsdon & Ponman 2000; Voit et al. 2003). This shows a departure from self-similar model and presence of non-gravitational effects in galaxy clusters.

3.1.3 Cosmic Downsizing

According to standard LCDM cosmology structures form hierarchically. This implies that bigger structures grow by accretion and merging of smaller structures. Superimposed on this distribution of dark matter are the baryons which fall into the dark matter potential well, and eventually undergo radiative cooling to form stars. The larger the structure is, the longer it takes gas to cool (Rees & Ostriker 1977; Silk 1977) and form stars. This makes, galaxy formation even more hierarchical than dark matter. However optical and near infrared observations show that the largest galaxies are in place and the relatively smaller ones are still forming stars at a redshift of 2.0 (e.g., Glazebrook et al. 2004). This effect is called "cosmic downsizing" (Cowie et al. 1996). This anti-hierarchical scenario in galaxy distribution is thought to be the impact of local baryonic physics.

3.1.4 The Missing Piece

Recent observational and theoretical studies have suggested that AGNs could be the missing piece in this picture. The observed correlation between black hole mass-bulge mass (e.g., Gebhardt et al. 2000; Merrit & Ferrarese 2001; Tremaine et al. 2002), and morphological parameters like the concentration and Sersic index (e.g., Graham & Driver 2007) of the host galaxies strongly suggest the connection between galaxy evolution and AGN activity. The

observed discrepancy in the $L_x - T$ relation suggests an additional heating of 2-3 keV per particle of the gas in the cluster (e.g., Wu, Fabian, & Nulsen 2000) and AGNs in cluster centers could be a plausible source for heating the surrounding gas. In recent work on theoretical models of galaxy evolution with AGN feedback the observed cosmic downsizing has been reproduced (e.g., Scannapieco & Oh 2004; Granato et al. 2004; Croton et al. 2006; Cattaneo et al. 2006; Thacker, Scannapieco, & Couchman 2006; Di Matteo et al. 2008). Parallel connections of the cosmic downsizing effect can also be drawn with the observed luminosity functions of quasars. Deep X-ray surveys of AGNs show that the spatial density of AGNs with higher X-ray luminosity peaks at a higher redshift than that of lower luminosity AGNs (e.g., Ueda et al. 2003). The theoretical simulations show that heating from AGNs suppresses star formation and hence formation of galaxies (e.g., Scannapieco & Oh 2004; Di Matteo et al. 2008; Scannapieco, Silk, & Bouwens 2005). The drop in the quasar luminosity function at lower redshifts has also been reproduced in these simulations (e.g., Scannapieco & Oh 2004).

Di Matteo, Springel, & Hernquist (2005) carried out simulations of galaxy mergers and used AGN outflows to produce the observed relation between black hole mass and velocity dispersion of stars in the center of the host galaxy ($M_{BH} - \sigma$) relation. Levine & Gnedin (2005) combined cosmological simulations with analytic modeling of AGN feedback to put a constraint on the redshift evolution of the filling factor for AGN outflows. They showed that the kinetic luminosity of the AGNs should be $< 10\%$ of the bolometric luminosity of the AGN or the intergalactic medium (IGM) would be filled with AGN outflows at $z = 0$. Levine & Gnedin (2006) also investigated the impact of AGN feedback on the matter power spectrum. They found two competing effects that impact the power spectrum. The AGN outflows move baryons from high to low mass regions, and thus decrease the amplitude of the matter power spectrum. Also, due to high clustering, AGNs transfer the power from large to small scales. With a semi analytic model of AGN feedback, Menci et al. (2006) studied the role of AGN feedback on the color distribution of galaxies from $z = 0$ to $z = 4$. They found that at low redshift AGN feedback increases the number of bright red galaxies. Croton et al. (2006) investigated the cosmological impact of AGN feedback to explain the low mass dropout rates in the cooling cores of galaxy clusters and reproduced the exponential cut-off

at the bright end of the galaxy luminosity function. Thacker, Scannapieco, & Couchman (2006) reproduced the observed $L_x - T$ relation in galaxy clusters and showed that AGN heating is more prominent in galaxy groups.

Evidence for the role of AGN feedback on galaxy evolution has been widely established through theoretical simulations and X-ray observations of galaxy clusters. However feedback models in theories depend on fine tuning of free parameters to match observed results. Also, no single theoretical model is sufficient in describing all the observed properties. AGN feedback has not been the only element that plays a role in theories of galaxy formation and several alternatives have been proposed in this context. To explain the downsizing effect, Keres et al. (2005) reported a bimodal distribution in the gas accretion phase in the galaxy distribution that accounted for the quenching of star formation in high mass galaxies. Stellar and supernova feedback (Pettini et al. 2001) have been other suggested alternatives for quenching star formation. Khochfar & Ostriker (2008) explained the quenching of star formation by including more sophisticated model of gas physics. In the context of non-gravitational heating source in clusters, other alternatives including cosmic rays (e.g., Colafrancesco, Dar, & DeRujula 2004), supernova outflows (e.g., Silk et al. 1986), and exotic events like interactions with dark matter (e.g., Totani 2004) have been addressed by different authors. Another alternative to AGN feedback has been thermal conduction (Zakamska & Narayan 2003). The theory involves conducting heat from the outskirts of the galaxy to the core. In the following Sections, I will describe the multifrequency observations and some theoretical models of AGN feedback.

3.2 X-RAY OBSERVATIONS OF AGN FEEDBACK

Modern X-ray telescopes are sensitive to X-ray energies ranging from 0.1 keV-10 keV (see McNamara & Nulsen 2007 for a review). Results from X-ray observations show that AGNs at the center of galaxy clusters are pouring huge amount of energy into the gas in the intra-cluster medium. AGN activity on the X-ray gas in clusters was first noted by Branduardi-Raymont et al. (1981) in Perseus with the Einstein satellite. Other observations with Rosat were done

by, e.g., Boehringer et al. (1993), Huang & Sarazin (1998). However the explanation of AGN activity was not fully understood until observations of the *Chandra* and XMM-Newton satellites. There has been observational evidence of three dozen cD galaxies in clusters and a similar number of giant Ellipticals (gE) harboring cavities or bubbles in their X-ray halos (e.g., McNamara et al. 2000; Heinz et al. 2002). It is believed that the cavities are produced by AGN outflows displacing the X-ray gas in the intracluster medium. Cavity systems in clusters can also vary in size from 1 kpc to 200 kpc (e.g., Forman et al. 2005). These X-ray cavities are associated with radio lobes and a correlation exists between radio luminosity and cavity power (e.g., Dunn & Fabian 2006). An interesting discovery from *Chandra* is the X-ray cavity that is not associated with radio lobes (McNamara et al. 2001; Fabian et al. 2002). These cavities are called ghost cavities and are believed to be aging radio relics that have broken free from the jets (see McNamara & Nulsen 2007 for discussion). The work required to inflate cavities against the pressure is around 10^{55} ergs in gEs and about 10^{61} ergs in rich clusters (e.g., Rafferty et al. 2006). The displaced gas mass from these cavities could be $10^{10} M_{\odot}$ in an average cluster system such as Abell 2052 (e.g., Blanton et al. 2001) but could be as high as $10^{12} M_{\odot}$ in powerful outbursts as seen in MS0735.6+7421 and Hydra A (see McNamara & Nulsen 2007 for references).

3.3 RADIO AND OPTICAL OBSERVATIONS

3.3.1 Radio Observations

The other major tool to study AGN feedback is through radio observations. Radio observations offer a view of the extent of AGN interaction, provide insights into outburst history, and give clues about source geometry, whereas from X-ray observations we get a direct view of the physical state of the gas, a measure of energies injected by outbursts, and a view of the gas motion (e.g., Vrtilek et al. 2008). Radio jets are the main mechanism by which energy is carried from AGNs. Burns (1990) studied the multifrequency properties of cD galaxies in clusters using radio data from 6 cm VLA maps and X-ray data from the Einstein IPC.

The results showed significant correlation between x-ray cooling cores and radio emission and morphology. As discussed before, the absence of sufficient cooling led to the hypothesis of AGN activity at the center of the cluster. It is now shown by, e.g., Dunn, Fabian, & Taylor (2005) and Dunn & Fabian (2006), that cooling core clusters harbor radio bubbles that are associated with AGN heating. Dunn & Fabian (2006) used the VLA and the Australian Telescope Compact Array (ATCA) to show that the radio morphology of some of these bubbles are bilobed with an average bubble size of $1 - 2$ kpc. Birzan et al. (2004) studied a large sample of X-ray cavities and radio bubbles in clusters and groups and obtained the PV energy of the cavity and their ages. Best et al. (2006a) estimated the heating rate from radio loud AGNs in galaxy clusters to be $H = 10^{21.4}(M_{BH}/M_{\odot})^{1.6}$ W, by using data from NVSS and Faint Images of the Radio Sky at Twenty centimeters (FIRST). Best (2007) showed that the heating from radio loud AGNs balances the cooling flow in elliptical galaxies within groups and clusters. However, it is important to note that the cooling flow problem is still not understood theoretically. AGN feedback is a possible explanation but there is still enough room in theory for cold gas to condense into filaments and make its way to the cluster center. At even lower radio frequencies Giacintucci et al. (2008) studied radio morphology of galaxy cluster AWM4 with the Giant Meter wave Radio telescope (GMRT) and found evidence of AGN feedback associated with the central radio source.

3.3.2 Optical Observations

Although most of the AGN activity in clusters is associated with radio loud quasars there has been substantial evidence of radio quiet quasars being effective enough in influencing their environments. The broad absorption line (BAL) quasars (Turnshek 1984) can affect their environments by producing strong winds (e.g., Fabian 1999). The current fraction of BAL quasars among the radio quiet population may be as high as $(22 \pm 4)\%$ (e.g., Hewett & Foltz 2003; Reichard et al. 2003). Gallagher et al. (2006) studied the X-ray properties of BAL quasars and found evidence of strong outflow. Chartas et al. (2007) also studied X-ray properties of BAL quasars and determined the fraction of the total bolometric energy released by the quasars into the intergalactic medium (IGM). Although there have been

various observational probes of the interaction of AGNs with their environments, it is fair to say that there is not a well established unified theory that will be sufficient to model the outflows and heating mechanisms in AGNs. In the next Section, I will describe some aspects of theoretical modeling of heating of cluster environments by AGNs. These theoretical models are not relevant in describing outflows from radio quiet quasars but assume the radio loud mode inherently. Different models associated with the generation of quasar winds in BAL quasars are described in deKool (1997).

3.4 THEORETICAL MODELS OF AGN FEEDBACK

I will discuss three representative models for AGN heating (see McNamara & Nulsen for a review).

3.4.1 Cavity Heating

From X-ray observations of galaxy clusters it has been shown that X-ray cavities are formed due to AGN activity. The total energy required to inflate the cavity is given by $H = E + PV$, where H is defined as the enthalpy of the system, E is the internal energy, and PV is the work required to displace the X-ray emitting gas. If the radio lobe within the X-ray cavity is filled with ideal gas (with a ratio of constant specific heat (γ)) we can write the total enthalpy of the system as $H = \frac{PV}{\gamma-1} + PV = \frac{\gamma}{\gamma-1}PV$. For different values of γ there will be different enthalpy profiles of the gas inside the cavity. As a buoyant cavity raises through the cluster atmosphere (e.g., Reynolds et al. 2002; Bruggen & Kaiser 2002) some X-ray gas moves inward to fill the space. If the cavity rises a distance δR and if M is the mass of the displaced gas, we can write the change in potential energy as

$$\delta U = Mg\delta R = -\frac{MdP}{\rho} = -V\delta P, \tag{3.1}$$

where g is acceleration due to gravity. Here we used the assumption of hydrostatic equilibrium. Using the first law of thermodynamics expressed in terms of enthalpy, we can write

an isentropic (adiabatic) process as

$$dH = TdS + VdP = VdP. \tag{3.2}$$

Thus we see that the kinetic energy created in making the bubble rise is equal to the loss of its enthalpy. The kinetic energy dissipates due to the viscosity of the surrounding gas in the form of heat. Using Eq. 3.2 we can write the enthalpy of a cavity as

$$H = H_0(P/P_0)^{(\gamma-1)/\gamma}, \tag{3.3}$$

where we have used the adiabatic equation of state PV^γ = constant to do the integral. H_0 is the initial enthalpy of the cavity and P_0 is the initial pressure of the surrounding gas. If the mean power injected by an AGN as cavity enthalpy is L_b we can write the mean heating rate per unit volume averaged over a sphere of radius R as (see McNamara & Nulsen 2007 for more discussion)

$$\Pi_b = -\frac{L_b}{4\pi R^2}\frac{d}{dR}\left(\frac{P}{P_0}\right)^{(\gamma-1)/\gamma}. \tag{3.4}$$

This model is described as the 1D effervescent heating model of AGN feedback (e.g., Begelman 2001; Roychowdhury et al. 2004; Guo, Peng, & Ruszkowski 2008). 3D simulations involving anisotropic cavity heating have been undertaken by Quilis et al. (2001) and Dalla Vecchia et al. (2004).

3.4.2 Shock Heating

Voit & Donahue (2005) have observed several clusters which have peaky entropy profiles in the centers and do not harbor strong radio sources. These samples of clusters show no evidence of AGN activity. They suggested that the high entropy signature is due to powerful shocks that were generated by AGNs in the past. Voit & Donahue (2005) showed that the entropy profiles of the clusters are consistent with shock heating within tens of kpc of the cluster center. In the outskirts there is more agreement with enthalpy heating (see McNamara & Nulsen 2007 and references therein). Shock heating tends to play an important role close to the AGN (e.g., Fabian et al. 2005). Shocks are believed to be generated due to instabilities in the accretion disc. The entropy created by dissipation of shock fronts is

proportional to the cube of the shock strength characterized by pressure instability (Landau & Lifshitz 1987). The equivalent heating rate is

$$\Pi_s = \frac{(\gamma+1)}{12\gamma^2}\frac{\omega_p}{2\pi}\left(\frac{\delta P}{P}\right)^3, \tag{3.5}$$

(McNamara & Nulsen 2007), where ω_p is the interval between shocks. In real observations the generation of shocks could be aperiodic. Evidence of weak shocks has been observed in some clusters (e.g., Forman et al. 2005; McNamara et al. 2005).

3.4.3 Sound Damping

Fabian et al. (2003) showed that viscous damping of sound waves generated by repeated outbursts of AGN may produce a significant amount of heating (see McNamara & Nulsen 2007 for references). The heating rate from sound damping can be written as (Landau & Lifshitz 1987)

$$\Pi_d = \left[\frac{2\mu}{3\rho} + \frac{(\gamma-1)^2\kappa T}{2\gamma P}\right]\frac{\omega^2\rho}{\gamma^2}\left(\frac{\delta P}{P}\right)^2, \tag{3.6}$$

where ρ, T, P, γ, κ, ω, and μ are density, temperature, pressure, ratio of specific heats of the gas, thermal conductivity, angular frequency, and viscosity, respectively.

In practice the non-gravitational energy coming from an AGN is propagated within the cluster environment by a combination of the three mechanisms described above. By comparing the heating rates, it is now known that the ratio of shock heating to sound damping decreases with radius. This makes shock heating confined to the regions near the AGN. The comparison of the theoretical rates show that cavity heating tends to be more centrally concentrated compared to shock heating but in practice cavity heating stays ineffective inside the radius where the cavity is formed. This makes shock heating the most centrally concentrated heating mechanism near the AGN. Cavity heating takes over the role outside the cavity (Voit & Donahue 2005). It appears that the mechanism of heating varies with radius and no single process can be considered the most significant.

3.5 THE SZ EFFECT AS A PROBE

It is also important to note that the overall level of feedback will depend on the source type. If it is within the radio-quiet mode (BAL quasar), the outflow will be dominated by winds. If it is in the jet mode, there will be shock heating and cavity heating. In clusters we mostly tend to observe the jet mode of feedback, and earlier studies claimed that radio loud AGNs tend to be found in dense environments compared to radio quiet ones (e.g., Ellingson, Yee, & Green 1991). However later studies showed that radio quiet AGNS are found in the same proportions as radio loud ones in galaxy clusters (e.g., Bahcall et al. 1997; McLure & Dunlop 2001). Theoretically a 'two-mode' model for AGN feedback has been recently proposed by Sijacki et al. (2007). These two modes are termed as "quasar mode" and "radio mode". The quasar mode corresponds to high accretion stages of the black hole with a radiatively efficient thin disc accretion (Shakura & Sunyaev 1973). The radio mode corresponds to low accretion phases of a black hole with geometrically thick radiatively inefficient accretion. The quasar mode radiates energy isotropically and the radio mode transfers energy in the form of anisotropic jets.

In our theoretical modeling and simulation work of AGN feedback in the next two Chapters, we have assumed spherical symmetry which will mostly be representative of the quasar mode of feedback. We note that although the transport mechanisms and the AGN types will be extremely important in describing AGN activity, the amplitude of feedback energy is the most relevant quantity in cosmological applications. The SZ effect which is sensitive to the total amount of feedback energy from the AGN will hence give a correct order of magnitude estimate of the signal. Since the SZ effect is an effective tool for studying accumulations of hot gas in the universe, regardless of the redshift of the source producing the hot gas, we propose to study the hot gas in AGN environments by studying its SZ distortion in the CMB. This SZ signal will be in addition to the SZ signal that we expect from virialized gas in galaxy clusters. This gives us a new observational tool to study feedback energy from active galaxies and put constraint on theories of galaxy formation.

4.0 ANALYTIC MODEL OF AGN FEEDBACK

In this Chapter, the calculation of SZ distortion from analytic modeling of AGN feedback is discussed. We have assumed a one dimensional Sedov-Taylor model of energy ejection and we analytically calculate the y distortion from it. We obtain the power spectrum of y distortion in multipole space and show its dependence on some of the free parameters in the model. Finally, we calculate the observational signal for SZ distortion from the power spectrum using a Gaussian beam. In §4.1 the Sedov-Taylor model and the equations used for modeling the feedback process are discussed. In §4.2 the mathematical formalism and the derivation of the y distortion are shown. In §4.3 the method for calculating the power spectrum is described. In §4.4 the dependence of the power spectrum on various parameters of the model is shown, and finally, in §4.5 the calculation of the observational signal from our model is illustrated.

4.1 AGN OUTFLOW MODEL

In our analytic model of AGN feedback we assume that an AGN injects a substantial amount of energy into the surrounding gas while it is active. Following Scannapieco & Oh (2004), we assume the black hole powering the AGN shines at its Eddington luminosity and returns around 5% of this energy to the galactic gas, eventually disrupting its own fuel source after a dynamical time of the cold gas surrounding the black hole, $t_{\rm dyn} \simeq 4 \times 10^7 (1+z)^{-3/2}$ yr (Barkana & Loeb 2001). The Eddington luminosity is the maximum luminosity beyond which radiation pressure prevents gas accretion. The Eddington luminosity can be evaluated by equating the radiative repulsive force on a free electron to the gravitational attractive

force on an ion in the plasma (Eddington 1926). The Eddington luminosity is given by $L_{ED} = (4\pi GcM_{BH}\mu_e m_p)/\sigma_T = 1.45\times10^{46}(M_{BH}/10^8 M_\odot)$ ergs/s. The dynamical time comes from the following ratio $M_{BH}/(dM_{BH}/dt)$. Using $\dot{M}_{BH} = \epsilon_0 L/c^2$ we can write the dynamical time as $t_{\rm dyn} \simeq 4\times10^7(\epsilon_0/0.1)(L/L_{ED})^{-1}$ yr, where ϵ_0 is the radiative efficiency. The feedback efficiency factor is assumed to be 5% (Scannapieco & Oh 2004). This is consistent with the theoretical estimate of Wyithe & Loeb (2003), where they assumed a self-regulatory accretion model and showed that (5%) is the limit within which a self-regulatory growth is achieved. The duration of the blast, $t_{\rm dyn}$, is much shorter than the expansion time of the resulting bubble of hot gas (on the order of 10^9 years). Therefore, we assume an instantaneous point source injection of energy into the intergalactic medium. The total energy output is just the product of the luminosity, the efficiency factor (ϵ_k), and the duration ($t_{dyn} = 5\times10^7(1+z)^{-3/2}$ years) of the explosion. The M_{bh}-σ relation (Merritt & Ferrarese 2001; Tremaine et al. 2002)and the $v_c - \sigma$ relation (Ferrarese 2002; Shields et al. 2003) can be used to connect the black hole luminosity with the mass of the host halo where σ and v_c are the velocity dispersion and the circular velocity of the host halo respectively.

$$M_{BH} = (1.66 \pm 0.32)\times10^8 M_\odot \left(\frac{\sigma}{200 kms^{-1}}\right)^{4.58\pm0.52}. \tag{4.1}$$

$$log_{10}\left(\frac{v_c}{300 kms^{-1}}\right) = (0.84\pm0.09) log_{10}\left(\frac{\sigma}{200 kms^{-1}}\right) + (0.55+0.19). \tag{4.2}$$

Combining Eq. 4.1 and 4.2 we get the following relation between black hole mass and circular velocity

$$M_{BH} = 1.4\times10^8 M_\odot F\left(\frac{v_c}{300 kms^{-1}}\right)^5, \tag{4.3}$$

where F is a constant free parameter taken as 0.6 (Scannapieco & Oh 2004). The circular velocity can be written as

$$v_c = 140 kms^{-1} M_{12}^{1/3}(1+z)^{1/2}, \tag{4.4}$$

where $M_{12} \equiv M_{\rm halo}/10^{12}M_\odot$. Using Eq. 4.3 and 4.4 we obtain the total energy injected from an AGN turning on at redshift z in a halo of mass $M_{\rm halo}$ as a function of $M_{\rm halo}$ and z. The relation is given as

$$E = \epsilon_k M_{BH} c^2 t_{dyn} = 0.06 M_{12}^{5/3}(1+z), \tag{4.5}$$

where $\epsilon_k = 0.05$ and c is the speed of light. E is shown in units of 10^{60} ergs. For simplicity, we assume that after the energy injection, a hot bubble evolves adiabatically and expands into a medium of uniform overdensity. The one-dimensional Sedov-Taylor solution is used to model the radius and temperature of the region contained by the blast wave (Scannapieco & Oh 2004).

The Sedov-Taylor model (e.g., Shu 1992) describes the theory of strong point like explosion in a uniform medium. Let us consider an amount of energy E being released into a static medium that has uniform density ρ_1. Let t be the time considered after the initial explosion. To know, how the radius (r_{sh}) of the energy ejecta (blast wave) grows in time we consider a dimensionality analysis. Let us consider r_0 to be a dimensionless quantity such that

$$r_0 = r_{sh} t^l \rho_1^m E^n. \tag{4.6}$$

This gives the following relations involving l, m, and n. $1 - 3m + 2n = 0$, $l - 2n = 0$ and $m + n = 0$. Using these relations we have

$$r_{sh} = r_0 (E t^2 / \rho_1)^{1/5}. \tag{4.7}$$

The velocity of the blast wave will be

$$U_{sh} = \frac{dr_{sh}}{dt} = \frac{2}{5}\frac{r_{sh}}{t}. \tag{4.8}$$

In a frame fixed to the center of the explosion, the Rankine Hugoniot jump condition gives relation between the pre shock (denoted by suffix 1) and post shock (denoted by suffix 2) quantities.

$$\rho_2 = (\frac{\gamma + 1}{\gamma - 1})\rho_1, \tag{4.9}$$

$$P_2 = (\frac{2}{\gamma + 1})\rho_1 U_{sh}^2, \tag{4.10}$$

where ρ and P are density and pressure of the medium, $\gamma = 5/3$, and $r_0 = 1.17$ (Shu 1992). Using the relation $P_2 = T_2 \rho_2 K_B / m_2$, where m_2 is the mean particle mass behind the shock, we use Eq. 4.9 and 4.10 to get the expression for the post shock temperature

$$T_2 = 3 m_2 U_{sh}^2 / 16 K_B. \tag{4.11}$$

From Eq. 4.7 we obtain the scaling of the radius of the blast wave.

$$R_s = r_{sh} = 1.7 E_{60}^{1/5} \delta_s^{-1/5} (1+z)^{-3/5} t_{\rm Gyr}^{2/5} \text{ Mpc} \tag{4.12}$$

where E_{60} is the energy of the blast (E) in units of 10^{60} ergs, δ_s is the ratio of the density of the surrounding medium to the mean cosmic baryon density, and $t_{\rm Gyr}$ is the expansion time of the bubble in units of 10^9 years. The variation of R_s as a function of redshift is shown in the top panel of Fig. 4.1. The velocity of the shock is given from Eq. 4.8 as

$$v_{sh} = U_{sh} = 1500 R_s^{-3/2} E_{60}^{1/2} \delta_s^{-1/2} (1+z)^{-3/2} \text{ kms}^{-1}. \tag{4.13}$$

Using Eq. 4.11 and 4.13 we get the scaling of temperature of the bubble as a function of time.

$$T_s = 13.6 \times U_{sh}^2 \text{ K} \tag{4.14}$$

$$T_s = 3.1 \times 10^7 E_{60} \delta_s^{-1} (1+z)^{-3} \left(\frac{R_s}{1\,\text{Mpc}} \right)^{-3} \text{ K}. \tag{4.15}$$

E_{60} can be computed using Eq. 4.5. The density of the gas inside the bubble is assumed to be uniform and equal to the density of the gas outside the bubble. We assume $\delta_s = 1$ in Eq. 4.12. This makes the density of the medium surrounding the bubble to be equal to the cosmic baryon density. This is a simplified assumption since it is widely seen in theoretical simulations that AGNs tend to favor dense environments. We note that the signal will weakly scale as a function of δ_s and so this simplified assumption will still be reasonably valid. Also the actual density profile within the bubble varies with radius (e.g., Shu 1992), but not strongly, and for simplicity we assume a constant density. The temperature profile within the bubble will also have a spatial variation but again we adopt a uniform temperature for the sake of simplicity and closed form solutions. The variation of temperature of the bubble with redshift is shown in the bottom panel of Fig. 4.1. We further assume that all the AGNs eject their energy at a single redshift z_{in}.

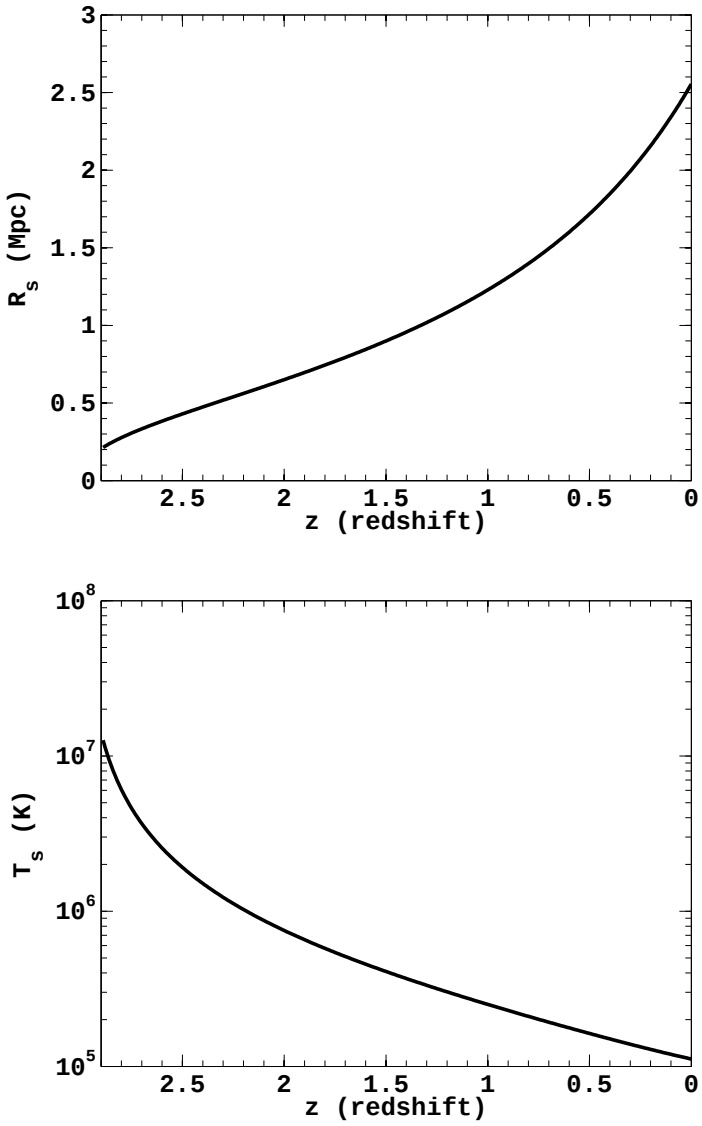

Figure 4.1: The radius (top panel) and temperature (bottom panel) of the bubble is shown as a function of redshift. The profiles are shown for a halo mass of $10^{12} M_{\odot}$ and $\delta_s = 1$. The profiles correspond to Eq. 4.12 and 4.15.

4.2 CALCULATION OF THE Y DISTORTION

The y distortion in Eq. 2.54 is given as the integrated line of sight pressure of the gas in the bubble. To calculate the y distortion we assume the bubble to be spherically symmetric. With the assumption of spherical symmetry, constant temperature, and constant number density of electrons inside the hot bubble surrounding the AGN, the y-distortion $y(\theta)$ on the sky will be azimuthally symmetric, depending only on the angle θ between the bubble center and a particular line of sight. The line of sight distance is given as $l = 2(R_s^2 - D_A^2\theta^2)^{1/2}$, where R_s is the radius of the bubble and $D_A(z)$ is the angular diameter distance to redshift z. We can write the y distortion as (after integrating Eq. 2.54)

$$y(\theta) = \frac{4\sigma_T K_B}{m_e c^2} T_e n_e R_s \left[1 - \frac{D_A^2\theta^2}{R_s^2}\right]^{1/2} . \tag{4.16}$$

The profiles of y distortion at redshifts 1.0 and 3.0 are shown in Fig. 4.2. The y distortion profiles in galaxy clusters follow an isothermal β profile. The profiles in galaxy clusters are shown in Appendix D. With a small angle approximation we can write the angular Fourier transform of the y-distortion as (cf. Peebles 1980; see Appendix D for derivation)

$$y_l = \frac{8\pi K_B \sigma_T}{m_e c^2} T_e n_e R_s \int \theta d\theta \left[1 - \frac{D_A^2\theta^2}{R_s^2}\right]^{1/2} J_0\left[\left(l + \frac{1}{2}\right)\theta\right], \tag{4.17}$$

where J_0 is the cylindrical Bessel function of order 0. With further simplifications we get,

$$y_l(m,z) = \frac{8\pi K_B \sigma_T}{m_e c^2} \frac{T_e n_e R_s^3}{D_A^2} \int_0^1 (1-s^2)^\mu J_\nu(bs) s^{\nu+1} ds, \tag{4.18}$$

where $s^2 = D_A^2\theta^2/R_s^2$, $\mu = 1/2,$, $\nu = 0$, and $b = (l + 1/2)R_s/D_A$. This integral can be performed analytically (Gradshteyn & Ryzhik 1980) and is given as

$$I = 2^{1/2}\Gamma(3/2) b^{-3/2} J(b). \tag{4.19}$$

From Eq. 4.18 and 4.19 we get,

$$y_l(M,z) = \frac{16\sigma_T K_B T_e n_e R_s^{3/2}}{D_A^{1/2}} \left(\frac{\pi}{2l+1}\right)^{3/2} J_{3/2}\left[\left(l + \frac{1}{2}\right)\frac{R_s}{D_A}\right]. \tag{4.20}$$

We note that T_e and R_s depend on both the halo mass M and the redshift z, and n_e depends on z. Equation 4.20 gives the analytic form of the y distortion in multipole space.

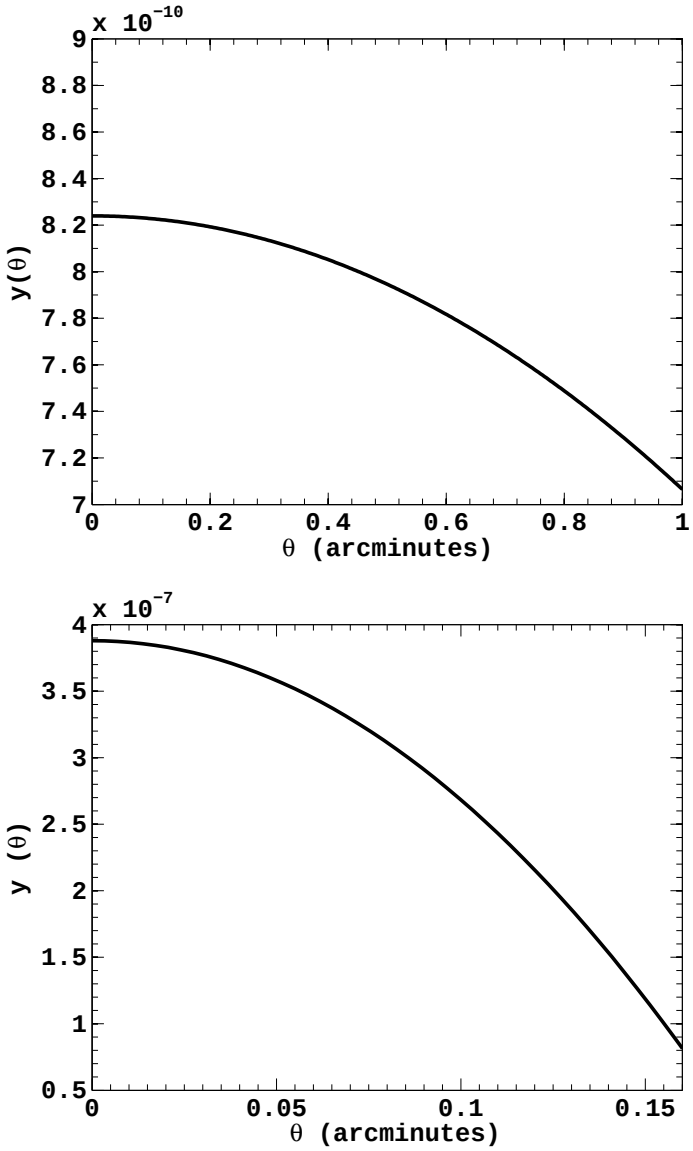

Figure 4.2: Profile of y distortion within the bubble radius at redshift 1.0 (top panel) and redshift 3.0 (bottom panel). The size of the bubble is smaller (see top panel of Fig. 4.1), but the temperature of the bubble is higher (bottom panel of Fig. 4.1) at higher redshift. This makes the signal higher at higher redshift. The halo mass is assumed to be $10^{12} M_{\odot}$, with $\delta_s = 1$.

4.3 CALCULATION OF THE POWER SPECTRUM

The y-distortion on the sky can be conventionally expanded in terms of the spherical harmonics as $y(\hat{\mathbf{n}}) = \sum_{lm} a_{lm} Y_{lm}(\hat{\mathbf{n}})$. The angular power spectrum is then obtained as $C_l = \langle |a_{lm}|^2 \rangle$, an ensemble average over the coefficients. The power spectrum has two components (e.g., Cole & Kaiser 1988, see Cooray & Sheth 2002 for a review), $C_l^{yy} = C_l^p + C_l^c$, where C_l^p is the contribution from Poisson noise of the random galaxy distribution, and C_l^c comes from the correlation between galaxies. The two terms are given as (e.g., Komatsu & Kityama 1999; Majumdar, Nath, & Chiba 2001)

$$C_l^p = \int_0^{z_{in}} dz \frac{dV}{dz} \int_{M_{min}}^{M_{max}} dM \frac{dn(M, z_{in})}{dM} \left| y_l(M, z) \right|^2 , \tag{4.21}$$

$$C_l^c = \int_0^{z_{in}} dz \frac{dV}{dz} P_m(k_l(z)) \left(\int_{M_{min}}^{M_{max}} dM \, \Phi_l(M, z) \right)^2 , \tag{4.22}$$

where

$$\Phi_l(M, z) = \frac{dn(M, z_{in})}{dM} b(M, z_{in}) y_l(M, z), \tag{4.23}$$

$k_l(z) \equiv l/D_A(z)$ is the wave number corresponding to the multipole angular scale l at redshift z, dV/dz is the comoving volume element, $dn(M, z)/dM$ is the differential mass function, $P_m(k, z)$ is the matter power spectrum, and $b(M, z)$ is the linear bias factor. The expression for the correlated piece uses the Limber approximation (see Peebles 1980). The upper limit of the redshift integral z_{max} is assumed to be the redshift (z_{in}) at which all the AGNs eject there energy. As mentioned before (end of §4.1) we use a simplified assumption in which all the AGNs eject their energy at a single redshift.

We used the following quantities to compute the power spectra defined in Eq. 4.21 and 4.22. The comoving volume term is given in Hogg (1999) as

$$\frac{dV_c}{d\Omega dz} = \frac{D_H^3}{E(z)} \left(\int_0^z \frac{dz'}{E(z')} \right)^2 , \tag{4.24}$$

where $E(z) = (\Omega_m (1+z)^3 + \Omega_\Lambda)^{1/2}$ and $D_H = 3000 h^{-1} Mpc$ is the Hubble distance. Ω_m and Ω_Λ are cosmological parameters defined in Table 1.1. Throughout the work we assume a standard LCDM cosmology with $\Omega_m = 0.31$, $\Omega_b = 0.044$. To calculate the power spectrum

of fluctuations we need to find the number density of AGNs since we need to integrate over the mass function. To do this, we associate the number density of AGNs with the number density of dark matter halos at redshift z_{in} when the AGNs eject their energy, and we use the Sheth-Tormen function ($f(\nu)$) (Sheth & Tormen 1999; Seljak 2000) to calculate the number density of halos. We also assume a halo mass to black hole mass ratio of 10^4, roughly a factor of 500 from the bulge-black hole mass ratio (e.g., Marconi & Hunt 2003) and a factor 20 from the bulge-halo mass ratio (e.g., Dubinski, Mihos, & Hernquist 1996). If the minimum mass black hole needed to power an AGN is taken as $\simeq 10^7 M_\odot$, the minimum relevant halo mass is around $\simeq 10^{11} M_\odot$, which we take as a lower mass cut-off for the halos. We note that the effect we are calculating is from field AGNs (corresponding to the mass limits of halos described above) and not of AGNs that reside in cluster centers. In Chapter 5, we will use numerical simulations to show the effect of AGN feedback in galaxy groups (mass of the largest halos in the simulation corresponds to group size halos) and how it will contribute to the SZ signal. After we integrate the Sheth-Tormen function $f(\nu)$ over the solid angle we get the following equation (Seljak 2000):

$$\frac{dn}{dM} = 4\pi f(\nu) d\nu \frac{\bar{\rho}}{M}. \tag{4.25}$$

$$f(\nu) = \frac{(1+\nu'^p)\nu'^{1/2} e^{-\nu'/2}}{\nu},$$

$$\nu' = a\nu,$$

where, $a = 0.707$, $p = 0.3$

$$\nu = (\frac{\delta_c}{\sigma(M)D(z)})^2,$$

$\bar{\rho}$ is the mean density of the universe and δ_c is the value of a spherical overdensity at which it collapses at a given redshift z. For a de-Sitter model $\delta_c = 1.68$. To compute the linear growth factor $D(z)$ we assume the following form (Dodelson 2002)

$$D(z) = 2.5 \left(\int_0^{1/(1+z)} \frac{da}{(\frac{\Omega_m}{a^3} + \Omega_\Lambda)^{1.5}} \right) \Omega_m (\Omega_m (1+z)^3 + \Omega_\Lambda)^{1/2} \tag{4.26}$$

To calculate $\sigma(M = \frac{4}{3}\pi R^3\bar{\rho})$ in Eq. 4.25 we use the following equation $\sigma_R = \int P(k)W_R(k)k^2dk$. $W_R(k) = \frac{3}{k^3R^3}(\sin(kR) - kR\cos(kR))$ is the tophat window function. We also assume a Harrison-Zeldovich primordial power spectrum $P(k) = k$ and the matter power spectrum is computed using the transfer function fits given by Eisenstein & Hu (1999). The power spectrum is normalized to the WMAP3 value of $\sigma_8 = 0.77$ (Spergel et al. 2007). The linear bias is given by (e.g., Seljak 2000),

$$b(\nu) = 1 + \frac{\nu - 1}{\delta_c} + \frac{2p}{\delta_c(1 + \nu'^p)}. \tag{4.27}$$

The Sheth-Tormen mass function is normalized such that $\int_0^\infty f(\nu)d\nu = 1$. Using Eq. 4.24 and 4.25 we can compute the integrals in Eq. 4.21 and 4.22.

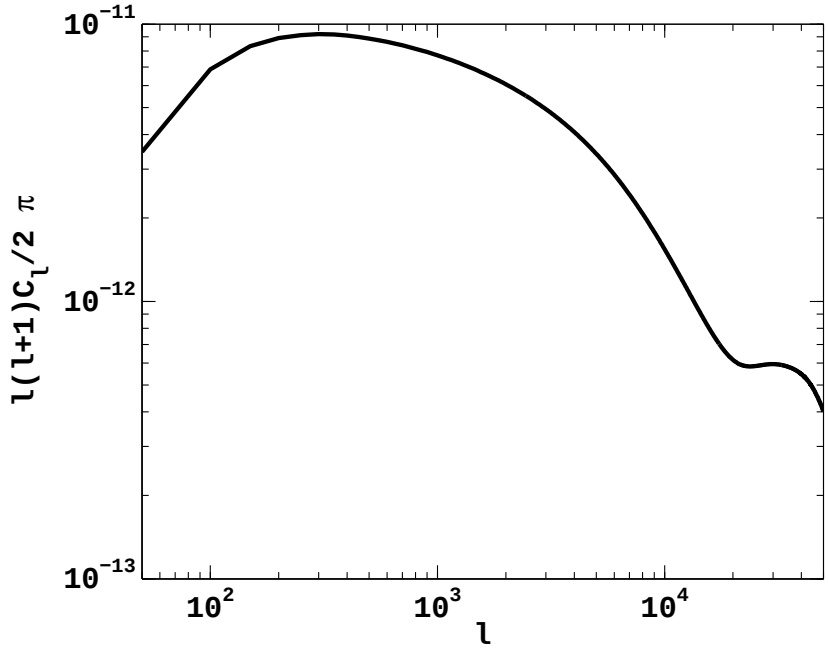

Figure 4.3: The y-distortion power spectrum, for $M_{\rm max} = 2 \times 10^{12} M_\odot$, $M_{\rm min} = 10^{11} M_\odot$, and $z_{in} = 3.0$. The signal is a combination of the correlation term (which peaks at $l = 290$) and the Poisson term (peaking at $l = 3.6 \times 10^4$).

Figure 4.3 shows the power spectrum of y distortion. The correlated term dominates for $l \leq 10^4$, with a broad, relatively flat contribution between $l = 100$ and $l = 2000$,

corresponding to angular scales from 2 degrees down to 5 arcminutes (the angular scales on which large scale structure is evident). The Poisson term contributes the secondary peak around $l = 3 \times 10^4$, at an angular scale of around $20''$ (the characteristic separation of galaxies). In this case $M_{max} = 2 \times 10^{12} M_\odot$, $M_{min} = 10^{11} M_\odot$, and $z_{in} = 3.0$. The y-distortion power spectrum can be converted to an effective temperature power spectrum at a given frequency via Eq. 2.56 and 2.57.

4.4 PARAMETER DEPENDENCE OF THE POWER SPECTRUM

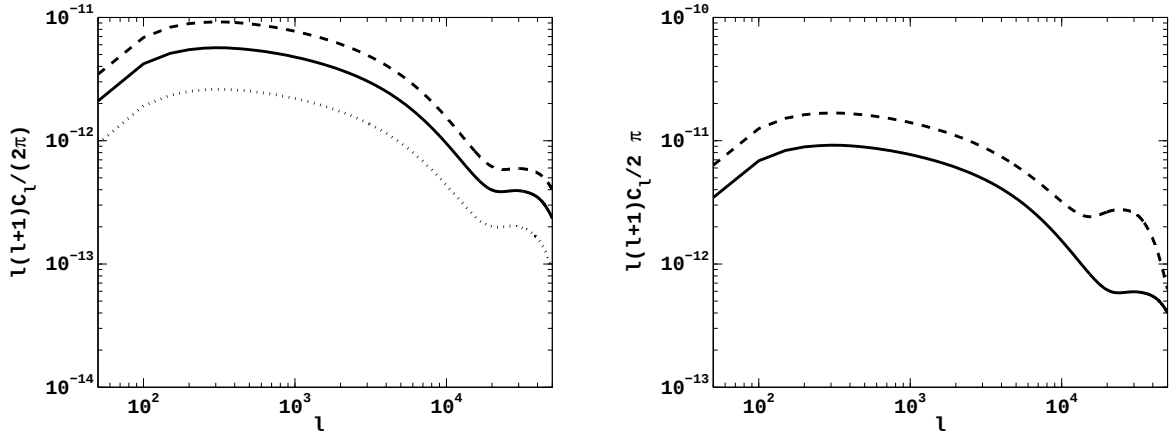

Figure 4.4: The left column of the figure shows the variation of the power spectrum with z_{in}. The three lines from bottom to top are for $z_{in} = 2.5$ (dotted), 2.8 (solid), and 3 (dashed) for a fixed $M_{\rm max} = 2 \times 10^{12} M_\odot$ and $M_{\rm min} = 10^{11} M_\odot$. The right column of the figure shows the dependence of the y distortion power spectrum on M_{max}. The dashed curve is for $M_{max} = 10^{13} M_\odot$ and the solid curve is for $M_{max} = 2 \times 10^{12} M_\odot$. Both the curves are shown at $z_{in} = 3.0$ and $M_{min} = 10^{11} M_\odot$.

The model relies on several free parameters such as $M_{\rm max}$, $M_{\rm min}$, z_{in}, δ_s, ϵ_k, and F. We show the dependence of the amplitude of the power spectrum on two parameters, namely M_{max} and z_{in} which are related to the maximum mass of the black hole and the initial redshift of energy injection. The left column of Fig. 4.4 shows the variation of the amplitude

of the power spectrum as a function of z_{in}. The three lines from bottom to top are for z_{in} = 2.5, 2.8, and 3.0 respectively. The right column of Fig. 4.4 shows the variation of the power spectrum amplitude with M_{max} (or M_{BH} thereof). From Fig. 4.4 we see that change in z_{in} from 3 to 2.5 reduces the power spectrum by roughly a factor of 2, with the Poisson term and the correlated term being affected equally. The dependence on maximum mass $M_{\rm max}$ is

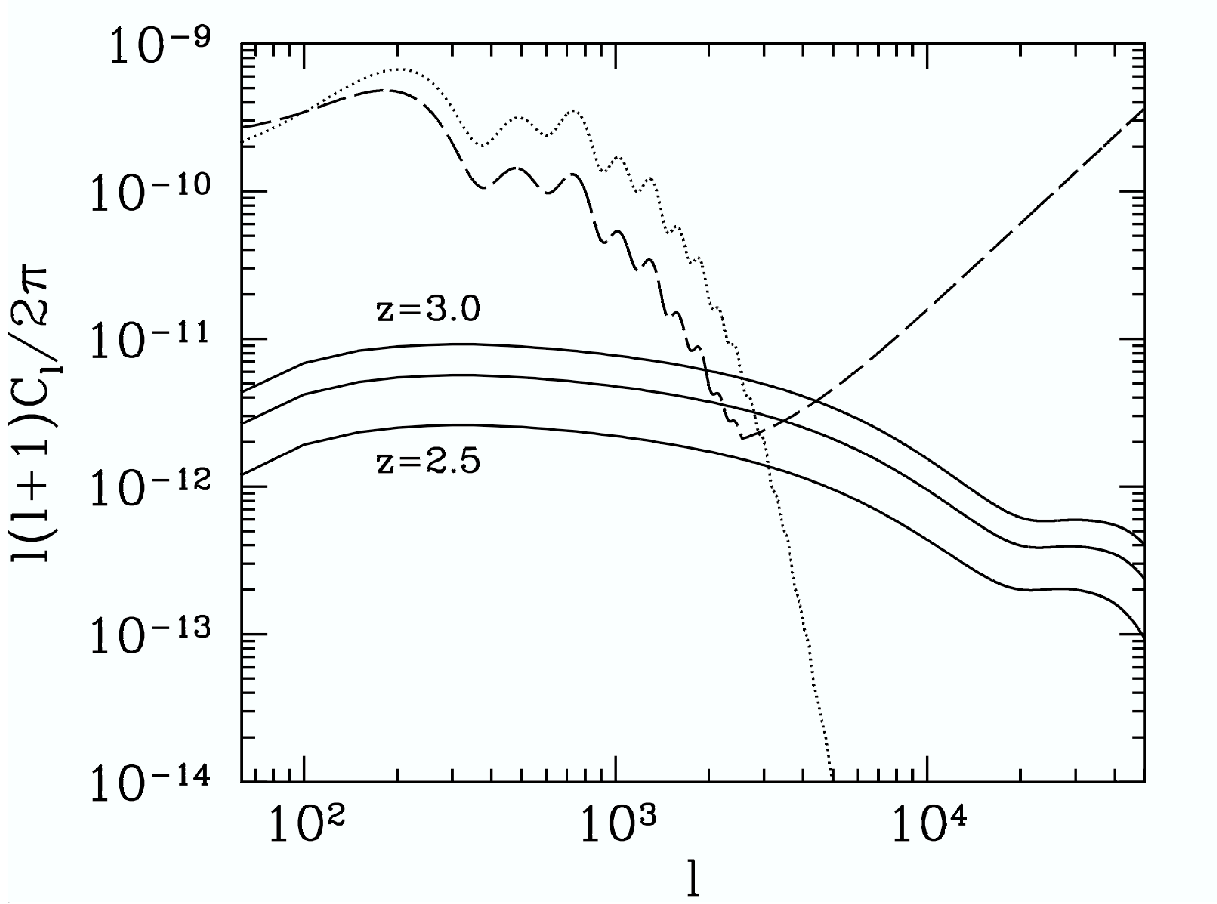

Figure 4.5: The y-distortion power spectrum with reference primary anisotropy (dotted line) and the noise level per l value (dashed line) for an ACT-like model experiment covering 400 square degrees with 1 arcminute resolution and a pixel noise of 2 μK (target pixel noise for ACT in the original proposal). In this case $M_{max} = 2 \times 10^{12} M_{\odot}$, $M_{min} = 10^{11} M_{\odot}$, and $z_{in} = 3.0$.

relatively weak: the power spectrum amplitude increases only by a factor of around 60% if the maximum mass is increased by a factor of 5. The other parameters in the model can also alter

the signal to a substantial degree. For example the signal scales linearly with the feedback efficiency. It also depends on the underlying assumptions of density and temperature in our model where a blast wave solution might not represent the exact morphology and dynamics of energy injection. Models discussed in Chapter 3 will provide more sophisticated description of AGN feedback but will lack the simplicity of the Sedov-Taylor model and its analytic closed form solutions. We emphasize that the magnitude of the signal will roughly remain the same even with a simple Sedov-Taylor scaling of a blast wave. Fig. 4.5 shows the angular power spectrum in comparison with the primary microwave background anisotropy, and the noise per l value for a model ACT-like experiment. We assume that the telescope maps 400 square degrees at one arcminute resolution and has a noise of 2 μK per pixel. We compute the noise per multipole using the approximate formula in Jungman et al. (1996)

$$\sigma_l = \left[\frac{2}{(2l+1)f_{sky}}\right]^{1/2} [C_l + (W_l f_{sky}^{-1} e^{l^2\sigma^2})], \tag{4.28}$$

where W_l is the window function (assumed to be Gaussian), f_{sky} is the fractional sky coverage, and σ is beam width. The signal from AGNs is above the noise level for a range in l $(4000 - 8000)$ but there will still be significant contributions from other sources at those angular scales.

4.5 CALCULATION OF SIGNAL

The mean square temperature fluctuation smoothed over a Gaussian beam is given as (see Peacock 1999)

$$\left\langle \frac{\delta T}{T}^2 \right\rangle = \frac{1}{4\pi} \sum_l (2l+1) W_l^2 C_l, \tag{4.29}$$

$$W_l = \exp(-l^2\sigma^2/2).$$

Root-mean-square temperature fluctuations are obtained by converting from y-distortion to temperature power spectrum at a given frequency, and then convolving with a Gaussian beam profile. We chose three different beam widths: an ACT-like beam of 1 arcminute, and

two Atacama Large Millimeter Array (ALMA [5]) resolutions of 15 and 5 arcseconds. The results are shown in Table 4.1, for the power spectrum with $z_{in} = 3$, $M_{\rm max} = 2 \times 10^{12} M_\odot$, and $M_{\rm min} = 10^{11} M_\odot$. The results show a signal of 2 μK in an arcminute beam. We will discuss the prospects of detecting this signal in Chapter 6.

Frequency (GHz)	Resolution (arcseconds)	Temperature (μK)
145	60	2.18
220	60	0.09
265	60	1.63
145	15	2.32
220	15	0.11
265	15	1.75
145	5	2.35
220	5	0.11
265	5	1.78

Table 4.1: Root-mean-square temperature fluctuations at ACT frequencies and three angular resolutions.

[5] http://www.alma.nrao.edu/

5.0 NUMERICAL WORK ON SUNYAEV-ZELDOVICH DISTORTION FROM AGN FEEDBACK

In this Chapter, I will discuss the numerical simulation of the SZ effect from AGN feedback. We use data from the simulations carried out by Di Matteo et al. (2008). The simulation uses a feedback model which is different from the analytic model described in Chapter 4. So this work is complimentary to the results discussed in Chapter 4 and gives us an opportunity to compare our analytic results with the numerical results. In §5.1 I will describe the numerical simulation that we have used to do the work. In §5.2 I will describe the y-distortion maps that are constructed from the simulation. In §5.3 I will discuss the angular profiles of the y distortion maps. Section 5.4, will be devoted to describing the scaling relation between y distortion and black hole mass that has been derived from the simulation. In Section 5.5, I will compare my numerical results with the analytic results obtained in Chapter 4.

5.1 NUMERICAL SIMULATION

We have used the simulation carried out by Di Matteo et al. (2008). The simulation is an N-body plus hydrodynamical cosmological simulation that includes radiative gas cooling, star formation, and for the first time a self-consistent treatment of black hole growth and feedback. I will briefly discuss the various aspects of this simulation with a special emphasis on the modeling of black hole growth and feedback.

The numerical code uses a LCDM cosmological model with cosmological parameters from the first year WMAP results (Spergel et al. 2003). A Gaussian initial condition is used with a scale invariant primordial power spectrum of spectral index, $n_s = 1$. The normalization

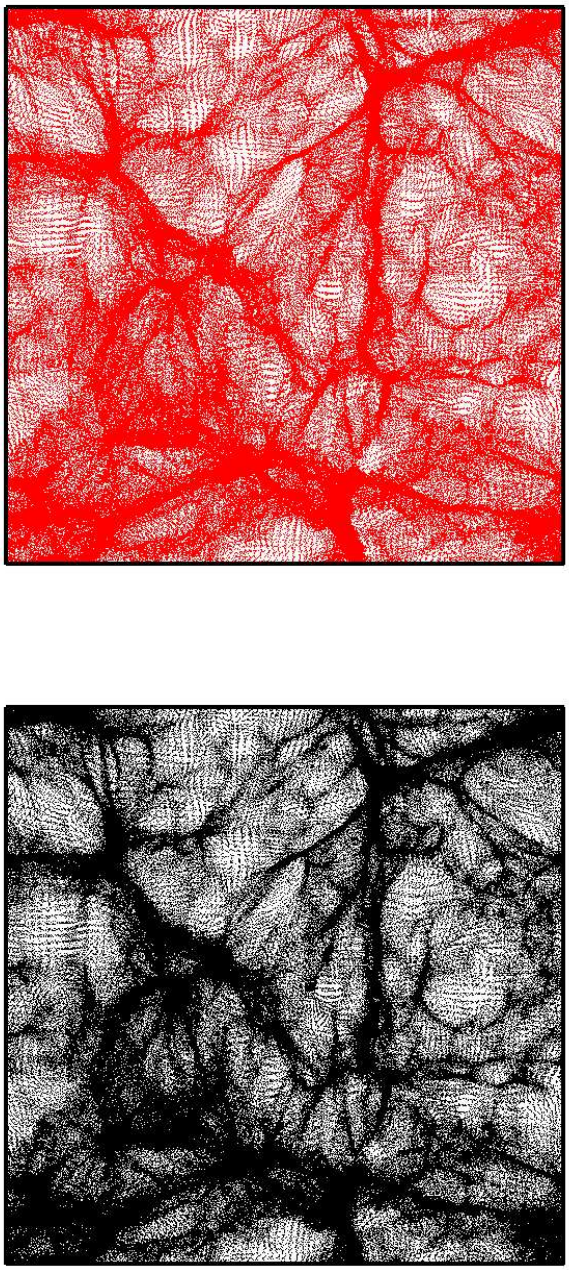

Figure 5.1: The distribution of dark matter (top panel) and gas (bottom panel) in the simulation at redshift 1.0. The simulation is the D4 run which is the lower resolution version. We have used this version for our analysis. The filamentary structures are evident from the map. The gas distribution follows closely the dark matter distribution. The box is $33.75h^{-1}$ Mpc on each side.

of the power spectrum is done with a σ_8 of 0.9. (While a lower value of σ_8 will affect the total number of black holes in a given volume, it should have little impact on the results for individual black holes presented here.) The simulation uses an extended version of the parallel cosmological Tree Particle Mesh-Smoothed Particle Hydrodynamics code (TreePM SPH) GAlaxies with Dark matter and Gas intEracT 2 (GADGET2; Springel 2005). The Tree PM algorithm is used for carrying out the evolution of the dark matter dynamics and the Lagrangian SPH method is used to follow gas dynamics. The distribution of dark matter and gas in the simulation is shown in Fig. 5.1.

5.1.1 N Body Dynamics

The Tree PM (Xu 1995; Bode, Ostriker, & Xu 2000; Springel, Yoshida & White 2001; Bagla 2002) code is a hybrid scheme involving the Tree code (Barnes & Hut 1986) and the Particle Mesh (PM) (e.g, Efstathiou et al. 1985) code. In a Tree code a hierarchical tree like structure is obtained for all the particles in a cell like structure unless a cell contains a sub cell or at least one particle. A cell that is sufficiently far away can be treated as a point source of mass within the cell and hence the force is computed using a multipole approximation. Depending on the distance of the cell from the current position, the multipole expansion is truncated. In a PM code the force is treated as a field quantity. The force is evaluated on a meshgrid and Fourier techniques are applied on it to calculate the Poisson equation. Both the PM method and the Tree algorithm have advantages over the direct particle particle (PP) scheme in terms of time. The main shortcoming of the PM code is that it is resolution limited (spatial resolution of the mesh) and it is difficult to handle with non uniform particle distribution. The tree code has the disadvantage of storage space. The hybrid TreePM code is a combination of both the schemes where a Tree algorithm is used for regions with higher densities, and a PM approach is used otherwise. This overcomes the limitation of resolution and storage or time in using the expensive tree code at regions with higher densities and using the PM code otherwise to save computing time. Other such existing hybrid schemes are the particle-particle-particleMesh code, (P^3M) (e.g, Couchman 1991), the adaptive mesh refinement (ART) (Kravtsov, Klypin, & Khokhlov 1997) method etc.

5.1.2 Gas Dynamics

Combining dark matter dynamics with gas dynamics (hydrodynamics) has made simulations more realistic and this allows simulations to link with observations. To do hydrodynamics, two kinds of approaches are popular. One involves an Eulerian or grid based formalism (Cen et al. 1990), where the frame of reference is space fixed. The other employs the Lagrangian description (Smoothed Particle Hydrodynamics (SPH)) (see Monaghan 1992 for a review), where the frame of reference is body or particle fixed. In a grid based method the gas properties are defined in a mesh grid whereas in SPH techniques the gas parameters at a point in the simulation are obtained by averaging the contributions from all the particles within a smoothing length. New adaptive mesh refinement codes to do hydrodynamics have been developed by e.g., Truelove et al. (1998); Norman & Bryan (1998). There are relative advantages and disadvantages for using these schemes to do hydrodynamics. Kang et al. (1994) and Frenk et al. (1999) does a comparison study of many of the available SPH and grid codes for cosmological applications. It is now believed that the SPH codes never produce shocks due to their intrinsic smoothing nature and are generally poorly behaved in low density regions compared to grid codes (Kang et al. 1994). However for high density regions and galaxy formation simulations the SPH techniques behave much better since the grid codes do not tend to conserve angular momentum although the cost of doing SPH simulations is more than grid codes. In the present simulation SPH is adopted since it involves galaxy merger simulations.

5.1.3 Supernova and Star-formation

Approximate schemes are employed to model the relevant physics of star formation and the associated supernova feedback. A hybrid multiphase model for the interstellar medium (ISM) (Springel & Hernquist 2003) has been used for this case. The modeling of star formation is described in Appendix E.

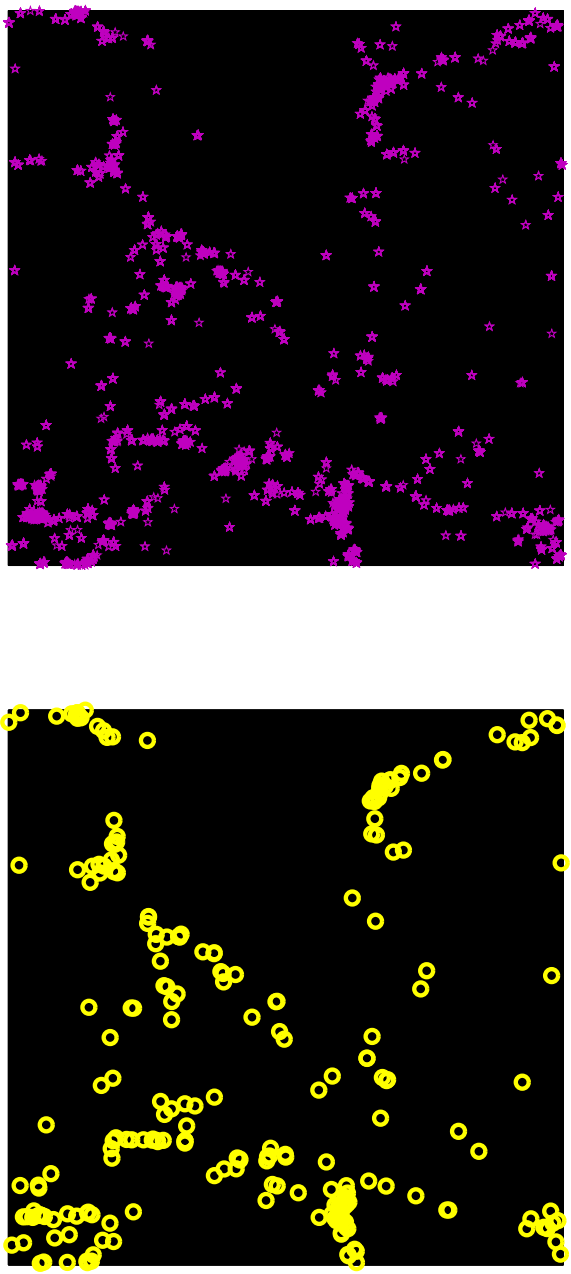

Figure 5.2: The distribution of stars (top panel) and black holes (bottom panel) in the simulation for the D4 run. The box is $33.75h^{-1}$ Mpc on each side.

5.1.4 Black Hole Feedback

A detailed description of the implementation of black hole accretion and the associated feedback model is given in Di Matteo et al. (2008). Black holes are represented as collisionless "sink" particles that can grow in mass by accreting gas or by merger events. The Bondi-Hoyle relation (Bondi 1952; Bondi & Hoyle 1944; Hoyle & Lyttleton 1939; see Appendix F) is used to model the accretion rate of gas onto a black hole. The accretion rate is given by $\dot{M}_{BH} = 4\pi[G^2 M_{BH}^2 \rho]/(c_s^2 + v^2)^{3/2}$, where ρ and c_s are density and speed of sound of the local gas, v is the velocity of the black hole with respect to the gas, and G is the gravitational constant. The radiated luminosity is taken to be $L_r = \eta(\dot{M}_{BH} c^2)$, where $\eta = 0.1$ is the canonical efficiency for thin disk accretion. It is assumed that a small fraction of the radiated luminosity couples to the surrounding gas as feedback energy E_f, such that $\dot{E}_f = \epsilon_f L_T$ with the feedback efficiency ϵ_f taken to be 5%. This number is same in magnitude to the feedback efficiency we assumed in our analytic model described in Chapter 4. The feedback energy is put directly into the gas smoothing kernel at the position of the black hole (Di Matteo et. al 2008). The efficiency ϵ_f is a free parameter in our AGN feedback model, and is chosen to reproduce the observed normalization of the $M_{BH} - \sigma$ relation (Di Matteo, Springel, & Hernquist 2005).

The feedback energy is assumed to be distributed isotropically for the sake of simplicity; however the response of the gas can be anisotropic. This model of AGN feedback as isotropic thermal coupling (representative of the quasar mode of feedback described in Chapter 3) to the surrounding gas is likely a good approximation to any physical feedback mechanism which leads to a shock front which isotropizes and becomes well mixed over physical scales smaller than those relevant to our simulations and on timescales smaller than the dynamical time of the galaxies (see Di Matteo et al. 2008 and Hopkins & Hernquist 2006 for more detailed discussions). In actual active galaxies, the accretion energy is often released anisotropically through jets. This difference needs to be investigated with further simulations, but the overall detectability of the signal depends primarily on its amplitude and characteristic angular scale, which are determined mainly by the total energy injection as a function of time. The results for the signals and detectability presented here are unlikely to differ significantly due to more

detailed modeling of the energy injection morphology. The formation mechanism for the seed black holes which evolve into the observed supermassive black holes today is not known. The simulation creates seed black holes in halos which cross a specified mass threshold. At a given redshift, halos are defined by a friends-of-friends group finder algorithm run on the fly. For any halo with mass $M > 10^{10}h^{-1}M_{\odot}$ which does not contain a black hole, the densest gas particle is converted to a black hole of mass $M_{BH} = 10^{5}h^{-1}M_{\odot}$; the black hole then grows via the accretion prescription given above and by efficient mergers with other black holes (Di Matteo et al. 2008). The distribution of stars and black holes in the simulation are shown in the top and bottom panels of Fig. 5.2 respectively. The total number of black holes at redshifts 3, 2 and 1 are listed in Table 5.3. A different simulation and feedback model has recently been used by Scannapieco, Thacker, & Couchman (2008) to study the same issues. They used the feedback model described in Chapter 4. In contrast, our simulation tracks the time-varying feedback from a given black hole due to changing local gas density as the surrounding cosmological structure evolves.

The simulations used in this work have a box size of $33.75h^{-1}$ Mpc with periodic boundary conditions. The simulation box with the distribution of all the particles are shown in Fig. 5.3. The characteristics of the simulation are listed in Table 5.1, where N_p is the total number of dark matter plus gas particles in the simulation, m_{DM} and $m_{\rm gas}$ are their respective masses, ϵ gives the comoving softening length, and $z_{\rm end}$ is the final redshift of the run. For redshifts lower than 1, the fundamental mode in the box becomes nonlinear, so large-scale properties of the simulation are unreliable after $z = 1$. The current results are derived for the D4 run with 2×216^3 particles. We will present brief comparisons with the higher-resolution D6 (BHCosmo) run to demonstrate that our results are reasonably independent of resolution.

5.2 THE Y DISTORTION MAPS

Figures 5.4 and 5.5 show y-distortion maps centered around two representative black holes in the simulation at redshifts 3, 2 and 1. The two black holes are the most massive (Fig. 5.4) and the second most massive black hole at redshift 3.0 (Fig. 5.5) in the simulation. We

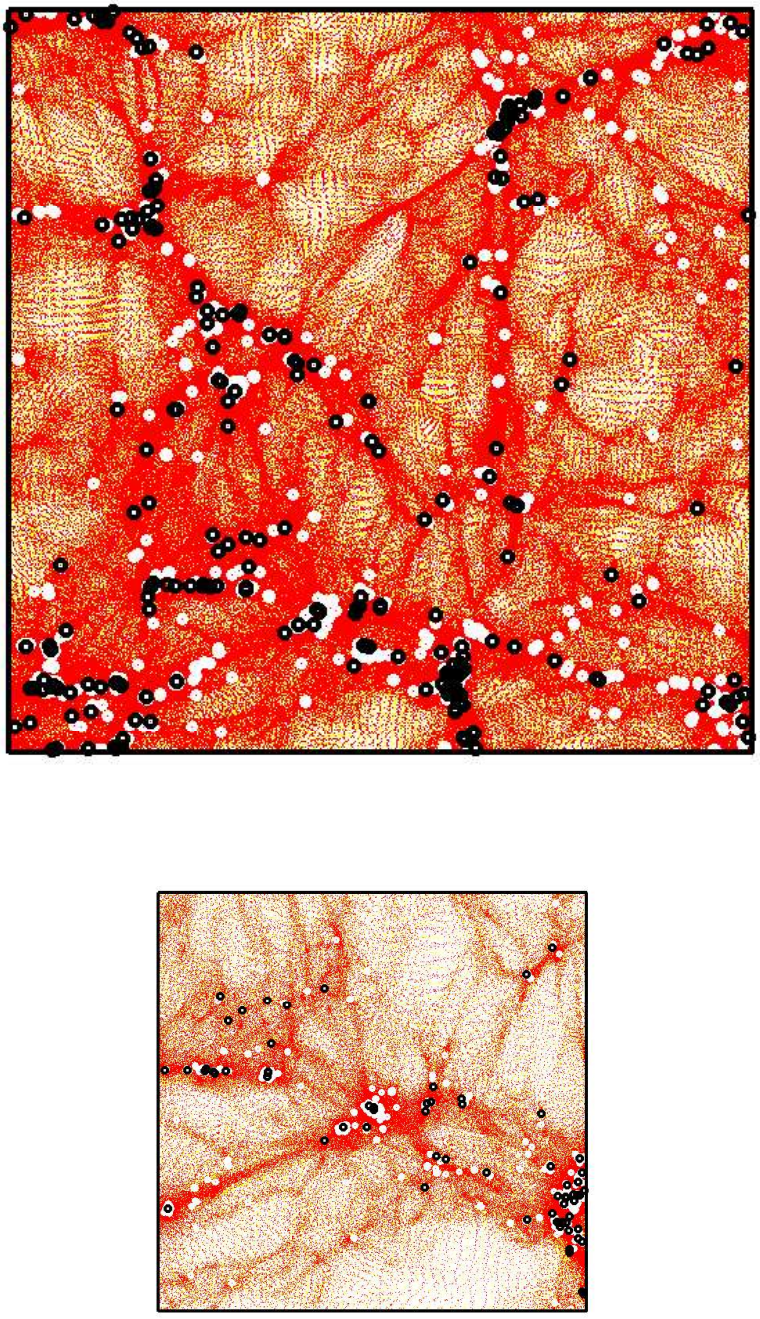

Figure 5.3: The simulation box with the distribution of dark matter (yellow), gas (red), stars (white), and black holes (black) at redshift 1.0. The maximum halo mass in the simulation is $4.71 \times 10^{13} M_{\odot}$. The box is $33.75 h^{-1}$ Mpc on each side. Due to spatial scales the star particles tend to be near the black holes. The bottom panel shows a zoomed in view of the distribution within a $13.5 h^{-1}$ Mpc box.

Run	Boxsize (h^{-1} Mpc)	N_P	m_{DM} ($h^{-1}M\odot$)	m_{gas} ($h^{-1}M\odot$)	ϵ (h^{-1} Kpc)	z_{end}
D4	33.75	2×216^3	2.75×10^8	4.24×10^7	6.25	0.00
D6 (BHCosmo)	33.75	2×486^3	2.75×10^7	4.24×10^6	2.73	1.00

Table 5.1: The numerical parameters in the simulation. For the current study we have used the low-resolution version because we have a matching simulation with no black holes; resolution effects are discussed in §5.2.1. N_p, m_{DM}, m_{gas}, ϵ and z_{end} are defined as the total number of particles, mass of the dark matter particles, mass of the gas particles, gravitational softening length, and final redshift run respectively.

have chosen the two most massive black holes in the simulation since the amplitude of the SZ distortion from the most massive black holes is relevant within the realm of current and future experiments. These maps were made by evaluating the line-of-sight integral in Eq. 2.54 through the appropriate portion of the simulation box. The y distortion is evaluated using the following approximation,

$$\begin{aligned} y &= \frac{K_B \sigma_T}{m_e c^2} \int_0^L \sum_i^N \rho(i) T_e(i) W(r_{ij}, h) dl, \\ &\simeq \frac{K_B \sigma_T}{m_e c^2} \sum_i^N \rho(i) T_e(i) \int_0^L W(r_{ij}, h) dl, \end{aligned} \tag{5.1}$$

where W is the smoothing kernel and h is the smoothing length. The smoothing kernel is given as

$$\begin{aligned} W(r,h) &= \frac{8}{\pi h^3}(1 - 6(r/h)^2 + 6(r/h)^3), 0 \leq \frac{r}{h} \leq \frac{1}{2} \\ &= \frac{8}{\pi h^3}(2(1 - r/h)^3), \frac{1}{2} \leq \frac{r}{h} \leq 1 \\ &= 0, O.W \end{aligned} \tag{5.2}$$

where $r(i,j)$ is defined as the distance between the ith and the jth particle. The above kernel is called the B spline kernel and has certain advantages, for example a continuous second derivative. In Eq. 5.1 we just approximate the 2D kernel with the 3D kernel for simplicity.

First black hole			Second black hole		
Redshift	N_{BH}	$\dot{M}_{BH}$, $M_\odot/yr$	Redshift	N_{BH}	$\dot{M}_{BH}$, $M_\odot/yr$
3.0	0	0.034	3.0	0	0.240
2.0	3	0.003	2.0	2	0.013
1.0	4	0.013	1.0	1	0.005

Table 5.2: The accretion rates and the number of neighboring black holes within a radius of 100 Kpc, for the two black holes in Fig. 5.4 and Fig. 5.5. The first black hole corresponds to the most massive black hole in the simulation. The other black hole is the second most massive black hole at redshift 3.0. The Eddington accretion rates are given as $\dot{M}_{ED} = 0.25 M_\odot (M_{BH}/10^8 M_\odot)$ /yr.

In order to characterize the large scale structure and associated y-distortions surrounding the black holes, we show a large region of the simulation within a comoving radius of 2.5 Mpc of the black hole in question, displayed with a comoving box size of 5 Mpc (left columns for Fig. 5.4 and Fig. 5.5) as well as a zoom into the central 200 Kpc box (right columns for Fig. 5.4 and Fig. 5.5). The smaller region (200 Kpc) is the relevant scale of interest when looking at the direct impact of the central black hole to its surrounding gas. The mass of the central black hole is $7.35 \times 10^8 M_\odot$ at $z = 3$, $2.76 \times 10^9 M_\odot$ at $z = 2$, and $4.32 \times 10^9 M_\odot$ at $z = 1$ (Fig. 5.4) and $7.11 \times 10^8 M_\odot$ at $z = 3$, $8.2 \times 10^8 M_\odot$ at $z = 2$, and $2.11 \times 10^9 M_\odot$ at $z = 1$ (Fig. 5.5). The feedback energy associated with black hole accretion creates a hot bubble of gas surrounding the black hole, which, as shown in the figures, grows significantly in size as redshift decreases. The growing hot bubble is roughly spherical by $z = 1$, in agreement with the assumption of the analytic spherical blast wave model which is described in Chapter 4.

In order to further characterize this expanding hot bubble, Fig. 5.6 and Fig. 5.7 display maps of the difference between the two simulations with black hole modeling and without, in the same 200 Kpc regions of Fig. 5.4 and Fig. 5.5. Fig. 5.6 shows the difference maps for the most massive black hole at $z = 3$ (left column) and $z = 1$ (right column) respectively.

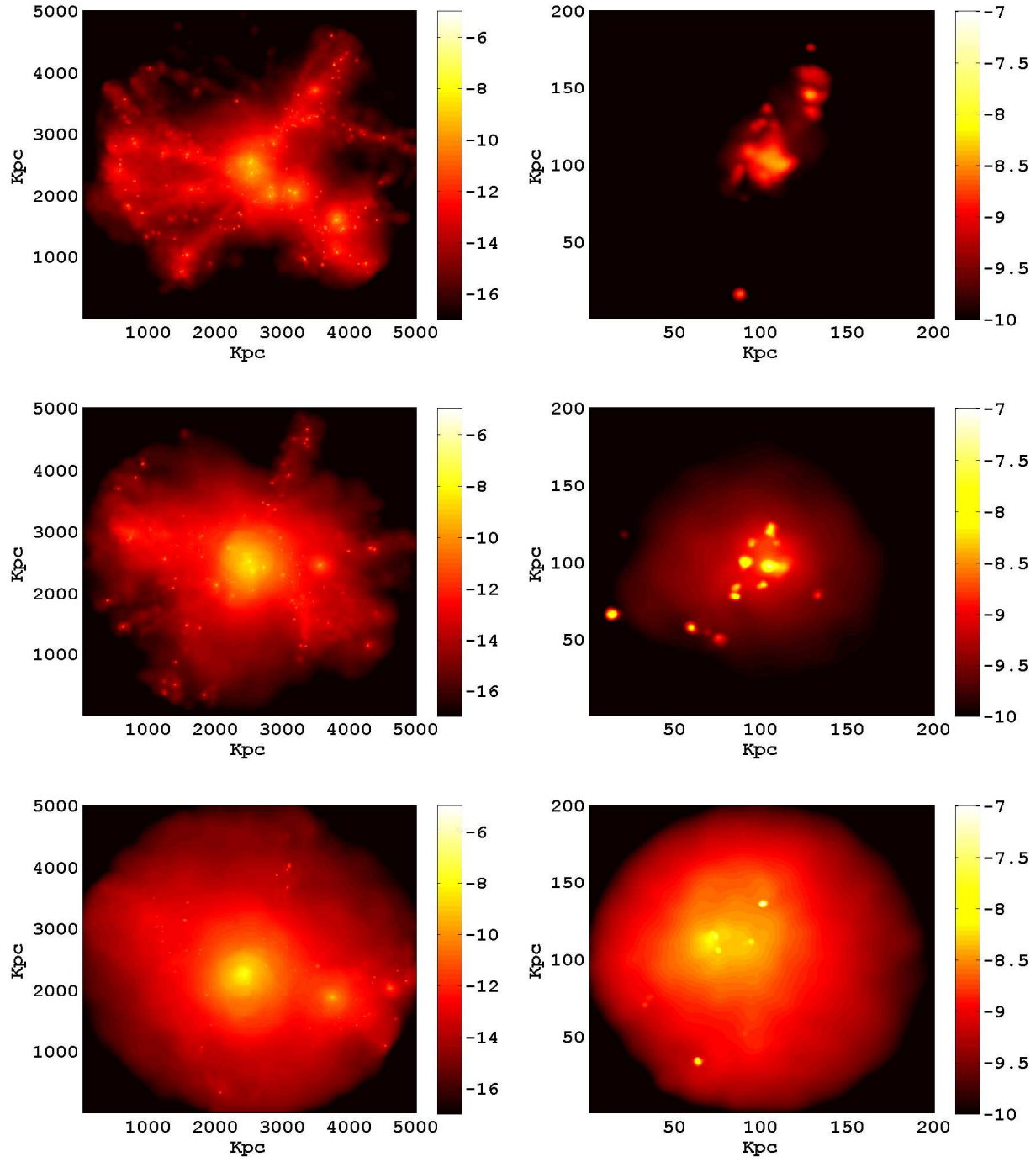

Figure 5.4: Simulated y-distortion maps around the most massive black hole in the simulation at three different redshifts $z = 3$ (top), $z = 2$ (middle), and $z = 1$ (bottom). The mass of the black hole is $7.35 \times 10^8 M_\odot$, $2.76 \times 10^9 M_\odot$ and $4.26 \times 10^9 M_\odot$ at redshifts 3, 2, and 1 respectively. The left column shows y in a 5 Mpc square region centered on the black hole and the right row zooms in to a 200 Kpc square. The peak value of y is between 10^{-7} and 10^{-6}.

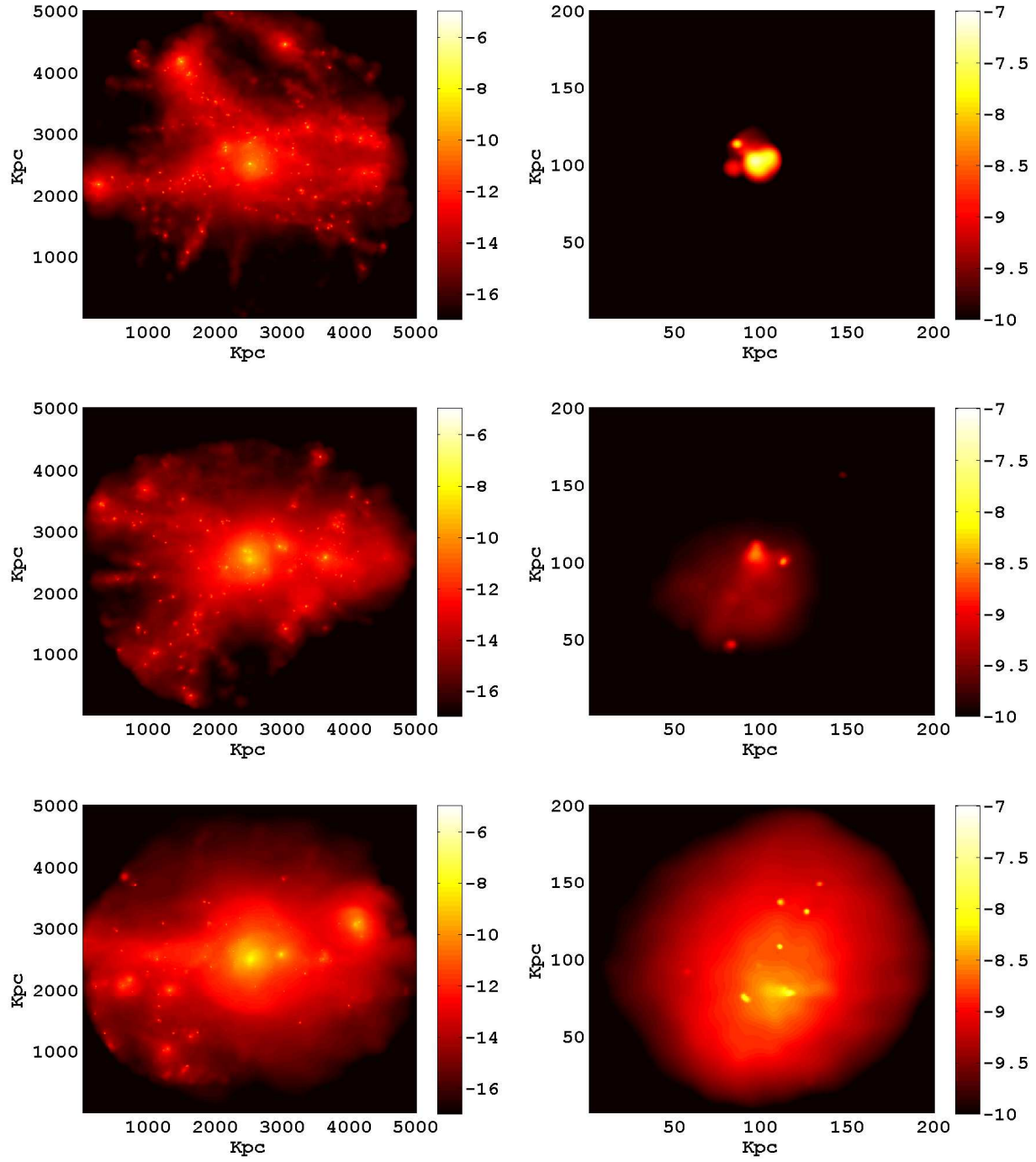

Figure 5.5: Simulated y-distortion maps around the second (second most massive black hole at redshift 3.0) black hole at three different redshifts $z = 3$ (top), $z = 2$ (middle), and $z = 1$ (bottom). The masses are $7.15 \times 10^8 M_\odot$, $8.2 \times 10^8 M_\odot$ and $2.11 \times 10^9 M_\odot$ at redshifts 3, 2, and 1. The left column shows y in a 5 Mpc square region centered on the black hole and the right column zooms in to a 200 Kpc square. The peak value of y is between 10^{-7} and 10^{-6}.

The left and right columns of Fig. 5.7 show the second black hole at the same redshifts. In both the figures, the top panel shows the logarithm of the y distortion, the middle panel is the logarithm of temperature in units of Kelvin and the bottom panel is the logarithm of projected electron number density in units of cm^{-2}. At $z = 3$, a residual y distortion is evident and concentrated around the black hole, with little effect further out; the peak y distortion due to the black hole is on the order of 10^{-7}, corresponding to an effective temperature shift of the order of 1 μK. By $z = 1$, the energy injected into the center has propagated outwards, forming a hot halo around the black hole. Table 5.2 shows the respective black hole accretion rates at different redshifts for the two black holes in Figs. 5.4 and 5.5. It is evident that the highest amplitude of y distortion is associated with the most active, high-redshift epochs of accretion, when large amounts of energy are coupled to the surrounding gas via the feedback process. At $z = 1$ the black hole accretion rate has dropped so the y distortion has a smaller amplitude but has spread over a larger region (Fig. 5.6 & Fig. 5.7).

5.2.1 Resolution Test

In the previous Section we have made use of the D4 (Table 5.1) simulations from our analysis. At this resolution we have two identical realizations, with and without black hole modeling, allowing us to carry out comparisons of the effects of AGN feedback. We now wish to assess possible effects due to numerical resolution by making use of the D6 (BHCosmo) run. Additional resolution tests with this simulation has been shown in Di Matteo et al. (2008), Croft et al. (2008) and Bhattacharya, Di Matteo, & Kosowsky (2008). Figure 5.8 shows the y distortion maps for the most massive black hole at redshifts 3, 2, and 1. The left column is for the higher-resolution BHCosmo run and the right column is for the lower-resolution run (D4). Our results at the lower resolution appear reasonably well converged, though with some differences. The central black hole masses in the two runs differ somewhat. At $z = 1$, 2, and 3, the black hole masses in the D4 and BHCosmo runs are ($4.29 \times 10^9 M_\odot$, $2.96 \times 10^9 M_\odot$), ($2.76 \times 10^9 M_\odot$, $1.85 \times 10^9 M_\odot$) and ($7.35 \times 10^8 M_\odot$, $8.56 \times 10^8 M_\odot$) respectively. It is clear that the difference in resolution is affecting the black hole mass as expected from modest

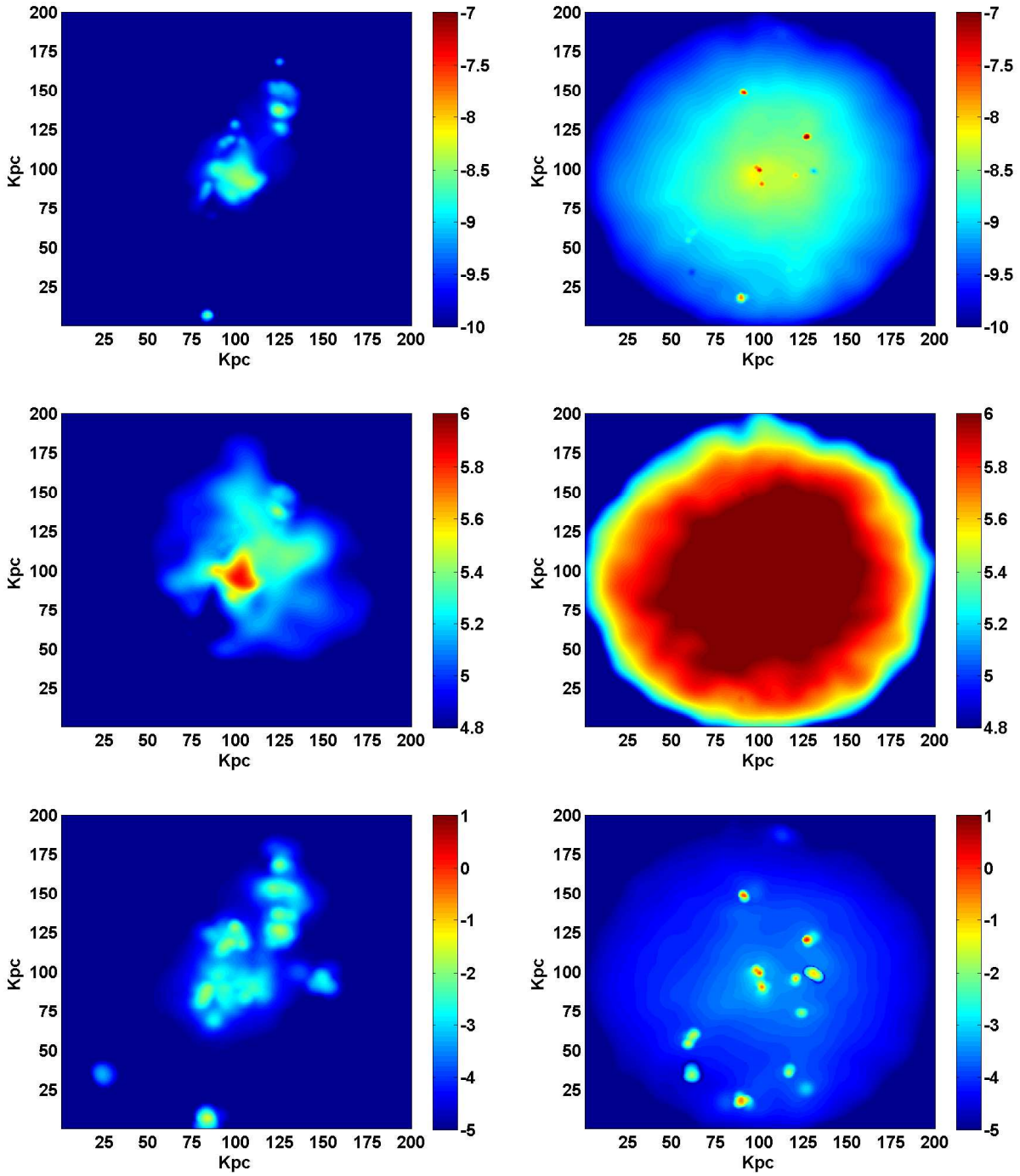

Figure 5.6: The difference in y-distortion between a simulation with black hole feedback and a simulation without, for the same region of space shown in Fig. 5.4. The two simulations have identical resolution and initial conditions. The left column corresponds to the most massive black hole at $z = 3$ and the right column at $z = 1$. The top panel shows y, the middle panel shows the log of the average temperature in units of Kelvin. The bottom panel shows the log of the electron number surface density in units of cm^{-2} .

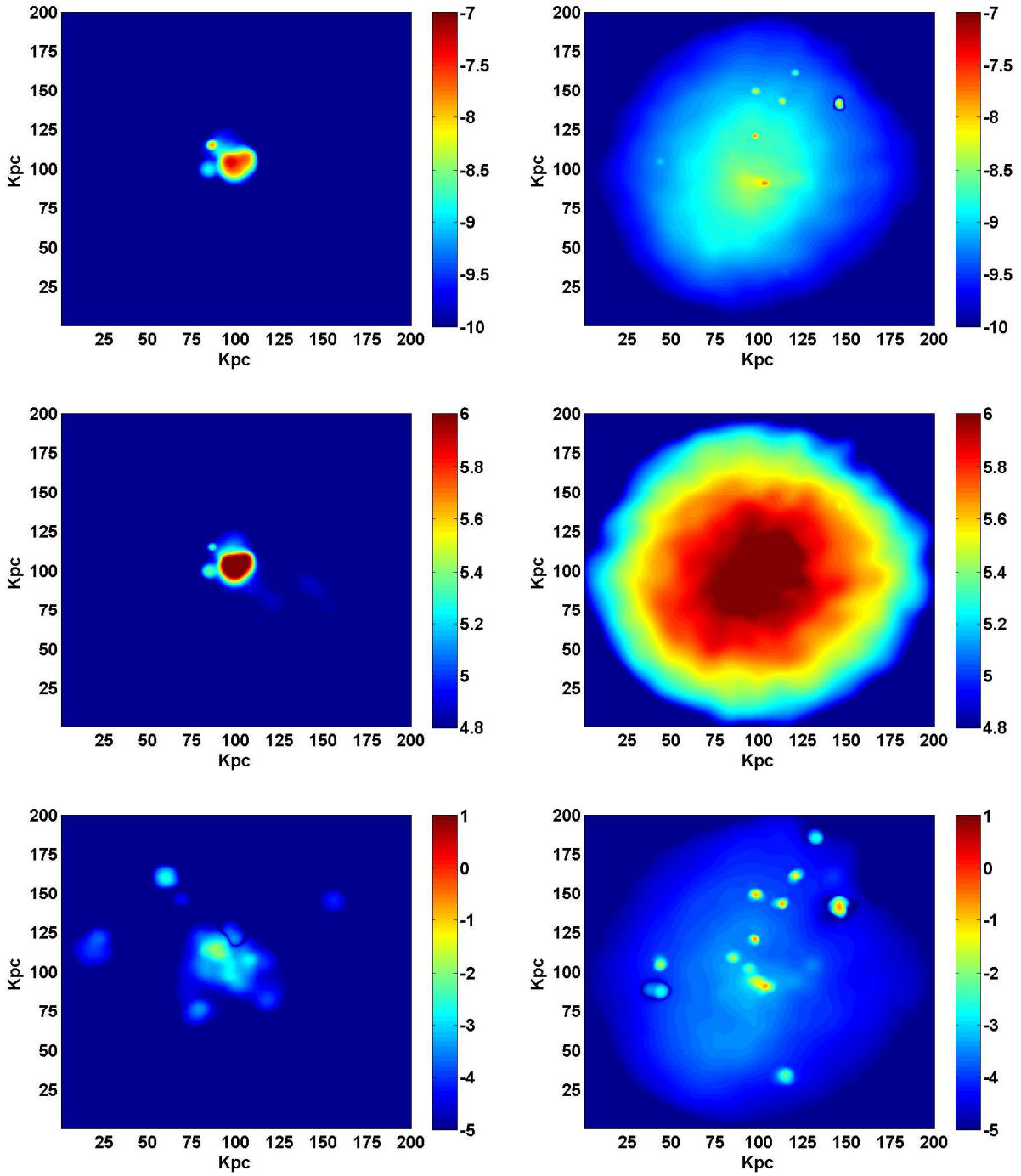

Figure 5.7: The difference in y-distortion between a simulation with black hole feedback and a simulation without, for the same region of space shown in Fig. 5.5. The two simulations have identical resolution and initial conditions. The left column corresponds to the second most massive black hole at $z = 3$ and the right column at $z = 1$. The top panel shows y, the middle panel shows the log of the average temperature in units of Kelvin. The bottom panel shows the log of the electron number surface density in units of cm^{-2} .

changes in mass accretion rates (which is sensitive to the gas properties close to the black hole). Also, more small scale structure in the gas distribution is evident at higher resolution, as expected. This affects the amplitude of the total SZ flux which is enhanced by about 6% at $z = 2$ and by about 22% at $z = 3$ (when it is most peaked around the black hole) in the higher resolution run.

5.3 THE ANGULAR PROFILES

For the two black holes shown in Figs. 5.4 and 5.5 we see an overall enhancement in the SZ signal due to AGN feedback. This agrees with the simulations done by Scannapieco, Thacker, & Couchman (2008). To further quantify the effects of AGN feedback we average the SZ signal in annuli around the black hole and examine the angular profile of the resulting y from the hot bubble in Figs. 5.4, 5.5, 5.6, and 5.7. Figure 5.9 shows the average angular profiles of the total y distortion around the two objects in the maps in Figs. 5.4 and 5.5. The black dashed, blue dot-dashed and red solid lines are for $z = 1$, $z = 2$, and $z = 3$ respectively. In both cases y increases with time between ~ 10 to 25 arcsecond separation from the black hole. At $z = 3$ the y profile is steeper in the central regions with a significant peak (in particular for the second black hole) at scales below 5 arcseconds. The bumps in the profiles are due to concentrations of hot gas or occasional other black holes which are included in the total average signal. y typically reaches its highest central peaks at time when the AGN is most active (the black hole accretion rate is high - see Table 5.2), and hence large amounts of energy are coupled to the surrounding gas according to our feedback prescription. For example, the $z = 3$ curve in the right panel shows the black hole at a particularly active phase; the central y distortion corresponds to a temperature difference of over 4 μK. At $z = 2$ this central distortion is smaller by a factor of 20, while it is larger by a factor of 10 at an angular separation of 10 arcseconds. Figure 5.9 shows the total SZ effect in the direction of an AGN resulting from the superposition of the SZ signature from AGN feedback plus the SZ distortion from the rest of the line of sight due to the surrounding adiabatic gas compression, which is expected to form an average background level in the

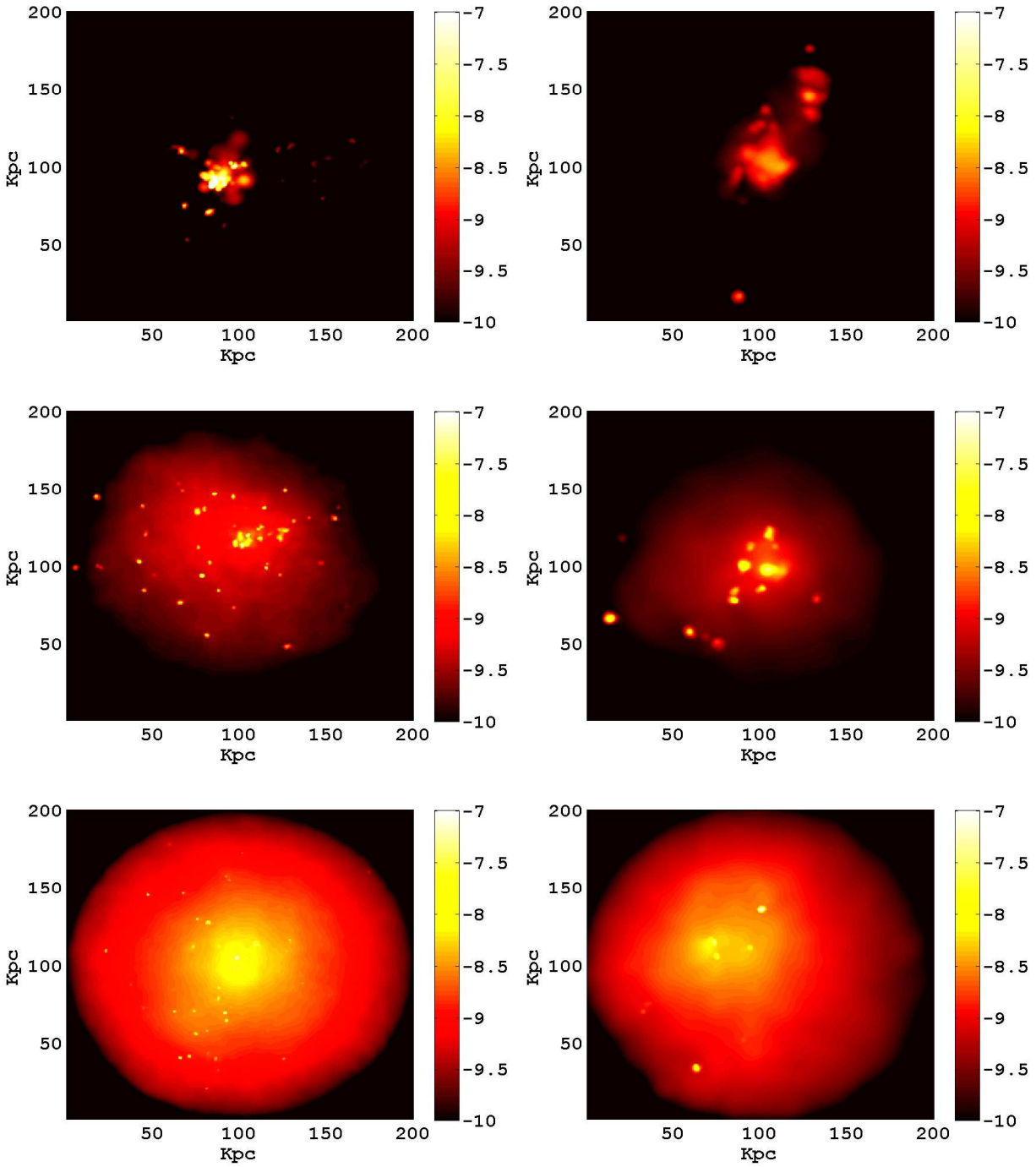

Figure 5.8: The left column shows y-distortion maps of the most massive black hole at $z = 3$ (top), $z = 2$ (middle) and $z = 1$ (bottom) in a higher-resolution (D6) simulation. The right column shows the same objects for a lower-resolution (D4) run. The difference in peak y value for D4 and D6 varies from 22% ($z = 3$) to 6% ($z = 2$) and it is higher for the D6 simulation at all three redshifts.

immediate vicinity of the back hole.

In order to clearly disentangle the contribution due to AGN feedback, in Fig. 5.9 (bottom panel), we plot the fractional change in y distortion between the simulation with and without black hole modeling, at two different redshifts. These are the profiles corresponding to the maps shown in Figs. 5.6 and 5.7. It is clear that the local SZ signature is largely dominated by the energy output from the black hole, giving a factor between 300 to over 3000 (for the second black hole at $z = 3$ in right panel) increase in y near the black hole. Our results are also consistent with the expected y distortion from the thermalized gas in the host halos containing these black holes (which are on the order $10^{12} M_{\odot}$ to $10^{13} M_{\odot}$) and in the range 10^{-9} to 10^{-7} (see also Komatsu & Seljak 2002). The largest peak in y distortion enhancement due to AGN feedback generally lies within 5 arcseconds of the black hole.

5.4 THE MASS SCALING RELATIONS

Since the SZ effect from the region around the black holes we analyzed in the previous Section is dominated by AGN feedback, we investigate whether a correlation between black hole mass and y distortion exists for the population as a whole. The left column of Fig. 5.10 plots the mean y distortion, computed over a sphere of radius 200 Kpc/h (i.e. the same as in the maps, corresponding to 20 arcseconds) versus black hole mass for all black holes in the simulations with $M_{BH} > 10^7 M_{\odot}$ at $z = 1, 2$ and 3 (from bottom to top respectively). The size of the region is chosen to sample the entire region of distortion due to AGN feedback, while minimizing bias from the local environment. The mass cut-off is chosen to (a) minimize effects due to lack of appropriate resolution in the simulations as well as (b) produce SZ distortions that may be detectable by current or upcoming experiments. Simple power law fits to the y distortion as a function of black hole mass show a redshift evolution with the scaling becoming steeper with decreasing redshift. Table 5.3 summarizes our results from the fits. The trends show a close correspondence between the mean y parameter and the total feedback energy as measured from y.

In order to further investigate the reason for $y - M_{BH}$ relations, in the right panel of Fig.

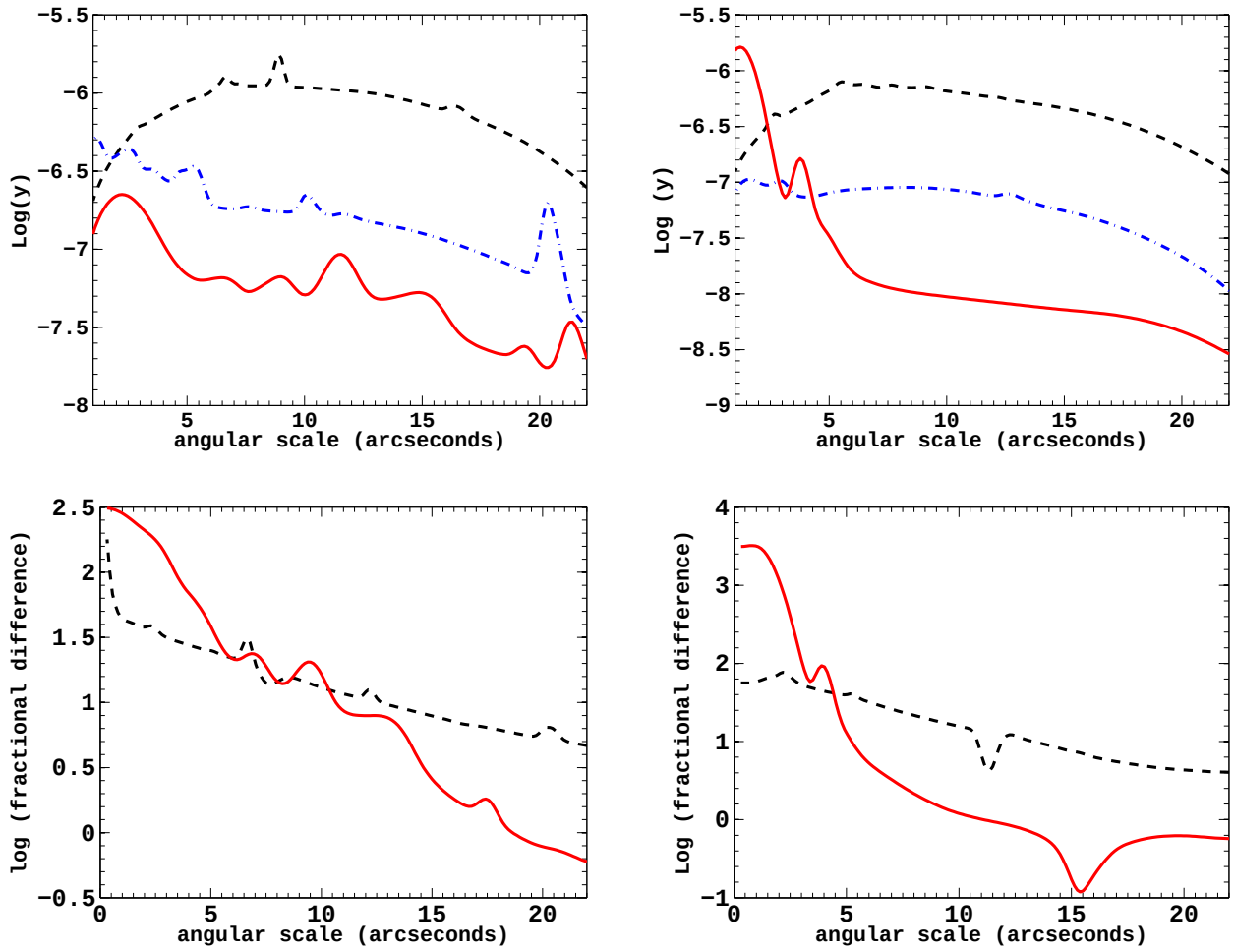

Figure 5.9: The top two panels of the figure show the angular profiles of the y distortion for the two black holes shown in Fig. 5.4 and 5.5 at three different redshifts. The solid, dot-dashed and dashed lines are for redshifts 3, 2, and 1 respectively. The top left panel shows the most massive black hole and the top right panel is the other black hole (second most massive black hole at redshift 3.0). The bottom two panels of the figure show the fractional difference in the y-distortion radial profile with and without black hole feedback, for the two black holes. The bottom left panel is for the most massive black hole and the bottom right panel is for the second black hole (second most massive black hole at redshift 3.0). For each, the dashed line is the fractional change in the y distortion with respect to the no black hole case at $z = 1$; the solid line is at $z = 3$.

z	N_{BH}	$N_{BH} \geq 10^7 M_\odot$	Fits for y	Fits for $\dot{M}_{BH}$
3.0	2378	127	$\log y = 0.56 \log(\frac{M_{BH}}{M_\odot}) - 9.8$	$\log(\dot{M}_{BH}) = 0.74 log(\frac{M_{BH}}{M_\odot}) - 8.1$
2.0	3110	336	$\log y = 1.00 \log(\frac{M_{BH}}{M_\odot}) - 14$	$\log(\dot{M}_{BH}) = 0.65 log(\frac{M_{BH}}{M_\odot}) - 8.4$
1.0	3404	404	$\log y = 1.90 \log(\frac{M_{BH}}{M_\odot}) - 22$	$\log(\dot{M}_{BH}) = 1.4 log(\frac{M_{BH}}{M_\odot}) - 15$

Table 5.3: Numerical values used in Fig. 5.10. Column 2 shows the total number of black holes in the simulation at redshifts 3, 2, and 1, while Column 3 shows the total number of black holes above a mass of $10^7 M_\odot$. Columns 4 and 5 show the scaling relations displayed in Fig. 5.10. The mass accretion rate is in units of $M_\odot$/yr.

5.10 we plot the accretion rates versus black hole mass at redshifts 3, 2, and 1 for the same sample as in the left column and perform similar power-law fits (see Table 5.3). The trends in accretion rate versus M_{BH} are qualitatively similar to the left column, demonstrating the connection of the y distortion due to AGN feedback with the black hole accretion rate and black hole mass. In particular, at $z = 1$ the relations get steeper as expected if the largest fraction of black holes are accreting according to the Bondi scaling (e.g., $\dot{M} \propto M_{BH}^2$), where as at higher redshifts there could be growth due to merging with other black holes. Of course, the accretion rate depends not only on black hole mass but also on the properties of the local gas and is also regulated by the large scale gas infall driven by major mergers, which peak at higher redshifts (Di Matteo et al. 2008). The fits for the mass scaling relation has sufficient scatter and therefore it is hard to predict the significance of the difference. The ratio of the slopes (accretion rate to y distortion) for the fits shown in Table 5.3 are 1.32, 0.65 and 0.73 at redshifts 3.0, 2.0 and 1.0 respectively. This shows the agreement of the left and right columns in Fig. 5.10, and the close connection between accretion history and SZ distortion. We show that the SZ effect tracks closely AGN feedback and is a promising probe of black hole accretion. The largest amplitudes of SZ signal from AGN is expected from $z \sim 2 - 3$ at a time close to the peak of the quasar phase in galaxies.

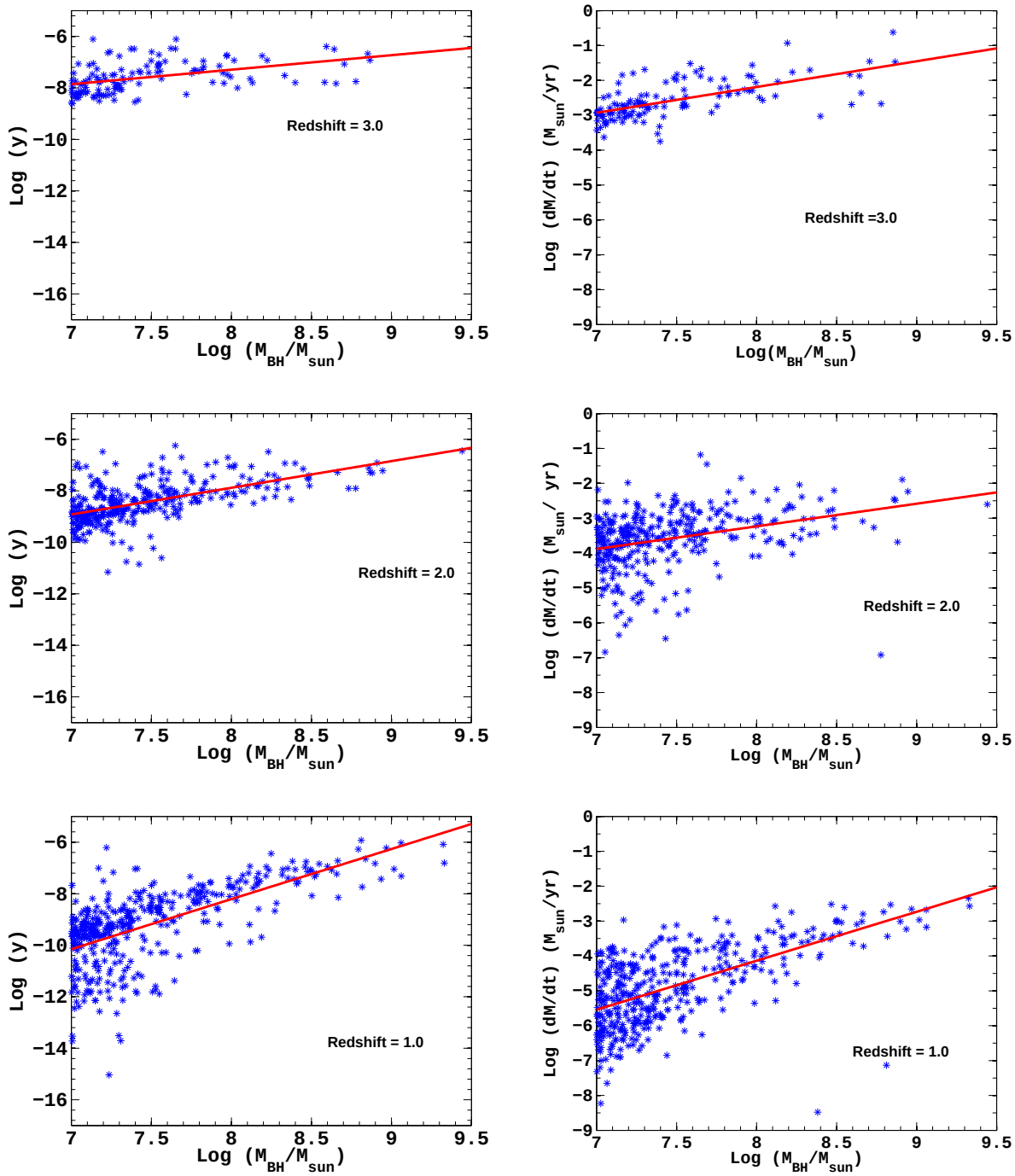

Figure 5.10: The left Column shows the mean y distortion within a comoving 200 Kpc region around the black hole as a function of black hole mass, for redshifts 3, 2 and 1 from top to bottom. The right Column shows the mass accretion rate as a function of black hole mass, for the same redshifts. The points are the numerical data and the solid lines are power-law fits. All black holes in the plotted mass range are included. The qualitative similarity between the left and right Columns shows the association of the y-distortion with accretion rates.

5.5 COMPARISON WITH ANALYTIC MODEL

In this Section, I will compare the numerical results with the analytic results obtained in Chapter 4.

5.5.1 Amplitude of y-distortion

We perform the following integration over the angular size of the source to get the average y distortion from our analytic model.

$$\Delta T = T_{CMB} \frac{\int_0^{\theta_{max}} y(\theta)\theta d\theta}{\int_0^{\theta_{max}} \theta d\theta}. \tag{5.3}$$

The integral can be solved analytically by the following substitution $\theta = \sin xR_s/D_A$. The result gives an average y of

$$\langle y \rangle = \frac{8\sigma_T K_B T_e n_e R_s}{3m_e c^2}, \tag{5.4}$$

where terms are described in equations 4.12 through 4.16. This gives an average y of 4.5×10^{-9} at redshift 1.0 and 3×10^{-7} at redshift 3.0. This is qualitatively similar with our numerical results. From the bottom panels of Fig. 5.9 we see that the signal is enhanced at redshift 3.0 compared to that at redshift 1.0 by a factor 1-2. However if we compute the average signal at these two redshifts from our numerical simulation we would roughly get a similar signal at these two redshifts. This is different from the results obtained with the analytic model. The peak amplitude of the signal is $10^{-6.5} - 10^{-7}$ at redshifts 3.0 and 1.0 in our numerical simulation (see Fig. 5.9). This amplitude agrees with the results from the analytic model at redshift 3.0 (bottom panel of Fig. 4.2) but is different for redshift 1.0 (top panel of Fig. 4.2).

5.5.2 Scale of the Bubble

The top panel of Fig. 4.1 shows the size of the bubble as a function of redshift in our analytic model. We assume that the bubble is formed at redshift 3.0. At redshift 1.0 the size of the bubble is about 1.3 Mpc. From Fig. 5.9 we can estimate the scale of the bubble in our

simulation at redshift 1.0. A bubble is about half an arcminute in size at redshift 1.0. This gives a physical scale of 480 kpc. This is three times smaller than the result obtained from the analytic calculation. It is important to note that the scale of the bubble can change depending on the free parameters in our analytic model.

5.5.3 Mass Scaling Relation

The mass scaling relation in our analytic model does not depend on redshift. Using Eq. 4.3, 4.4, 4.5, 4.12, 4.15, and 4.16 we can obtain the mass scaling of the y-distortion. This gives the y-distortion to be proportional to $M^{5/3} = M^{1.66}$ in our analytic model. From Table 5.3 we see that the mass exponent varies from 0.56 -1.9 from redshifts 3.0 -1.0 for the fits to the numerical data. It is important to note that the data has substantial amount of scatter (Fig. 5.10). The scatter is more prominent at redshift 1.0. The exponent for the analytic model is close to the exponent at redshift 1.0 obtained from the fits to the numerical data. However the resultant y distortion from our analytic model at redshift 1.0 is predicted to be much lower than what we get from our numerical results. The variation could be coming from the assumptions of the gas distribution around an AGN.

6.0 OBSERVATIONAL TECHNIQUES

In this Chapter, I will describe the techniques that can be used to measure the SZ distortion due to feedback from AGNs.

6.1 OBSEVATIONAL TECHNIQUES

Observationally, AGN feedback is directly detectable by resolving Sunyaev-Zeldovich peaks on small angular scales of tens of arcseconds with amplitudes up to a few μK above the immediately surrounding region. The combination of angular scale and small amplitude make detecting this effect very challenging, at the margins of currently planned experiments. The necessary sensitivity requires large collecting areas, while the angular resolution requires an interferometer in a compact configuration, or a large single-dish experiment. Since the SZ signal is manifested as a peak over the surrounding background level, a region substantially larger than the SZ peak must be imaged. This requires a telescope having sufficient resolution to resolve the central peak in the SZ distortion in an SZ image and enough field of view so that the peak can be identified. The other possible route for detecting this signal is through cross-correlation of microwave maps with optically selected quasars. The cross-correlation analysis of SDSS quasars and WMAP CMB maps is described in Chapter 7. It is important to note that all these methods have significant systematics which make the detection of this effect substantially difficult. The systematics are also described in Chapter 7.

6.2 DIRECT OBSERVATIONS

To do a direct detection, we need a high resolution interferometric experiment in a compact configuration. An example of such an instrument is the compact configuration of ALMA[5], known as the Atacama Compact Array (ACA). It is composed of twelve 7-meter dishes. The ALMA sensitivity calculator shows that the synthesized beam for this array is about 14 arc-seconds, and the integration time required to attain 1 μK sensitivity per beam at a frequency of 145 GHz and a maximum band width of 16 GHz is on the order of 1000 hours (ALMA sensitivity calculator). A very deep survey with this instrument can potentially detect the SZ effect from individual black holes. In Table 6.1 the ALMA sensitivity calculations are shown. However these numbers do not include the atmospheric effect. The atmosphere is a source of contamination in the millimeter-wave band. The atmosphere contains water vapor. Water vapor has a strong dipole component and the rotational transitions couple to millimeter wave radiations (see Lay & Halverson 2000). The sensitivities will be reduced significantly when atmospheric effects are considered. The 50-meter Large Millimeter-Wave Telescope (LMT

Frequency (GHz)	Resolution (arcseconds)	Baseline (km)	Sensitivity (μK)
145	15	0.0284	2.41
145	5	0.0853	21.74
220	15	0.0187	1.76
220	5	0.0562	15.84
265	15	0.0156	1.63
265	5	0.0467	14.63

Table 6.1: ALMA continuum brightness sensitivities for a one-hour observation. The limits are calculated using the ALMA sensitivity calculator. The limits do not include atmospheric effect. The sensitivities will be significantly reduced if atmospheric effects are considered.

[6]) instrumented with the AzTEC bolometer array detector will have a somewhat similar

[6]http://www.lmtgtm.org/

sensitivity. The LMT mapping time is $\approx 500\mu K/\sqrt(s)$. This needs an integration time of 17 hours to reach a 1 σ detection of the signal. The Cornell-Caltech Atacama Telescope (CCAT [7]), a 25-meter telescope, is estimated to have a sensitivity of 310 μK s$^{1/2}$ at 150 GHz. The angular resolution at this frequency will be 26 arcseconds. A thirty hour observation with CCAT can give a 1μK sensitivity. The resolution of the pixels will not be sufficient to resolve the hot halo around a black hole, but might be enough to detect the difference in signal due to black hole activity, compared to its surrounding.

Aside from raw sensitivity and angular resolution, a serious difficulty with direct detection is the confusion limit from infrared point source emission; these sources are generally high-redshift star forming galaxies with a high dust emission. CCAT estimates show that their one-source-per-beam confusion limit will be around 6 μK at 150 GHz. This will present substantial difficulties for detecting a 1 μK temperature distortion if accurate. We note that the observations in the sub-millimeter band is limited by confusion noise and so another possibility of direct detection of this signal is through radio telescopes. Massardi et al. (2008) shows that the confusion due to dusty galaxies is lower at 10 GHz then at 100 GHz. Massardi et al. (2008) claims that for detecting a galactic scale SZ effect, the optimum frequency range is 10 to 35 GHz. However substantial confusion from radio galaxies at these low frequency observations would still be a challenging issue in the direct detection of the signal. Table 6.2 shows the configurations necessary for an ideal interferometric instrument to detect this signal. This will equally apply to single dish experiments.

The scale associated with the peak of the distortion will limit the scale of the synthesized beam in an interferometer. The design of the experiment is based on the numerical results presented in Chapter 5. The second Column of Table 6.2 shows the synthesized beam size of the experiment relevant to the scale of peak SZ distortion (as shown in Fig. 5.5). The fourth Column in Table 6.2 shows the baselines that will be needed to do the observations at the frequencies specified in Column 3. From the physical dimension of the baselines it is clear that a compact configuration or a single dish experiment will be better in probing the signal. Also, to see a potential SZ effect around a black hole, one needs a reasonable observation of the background which requires a large primary beam of size 10-20 times the

[7] http://www.submm.org

Relevant scale arcseconds	Synthesized beam arcseconds	wavelength GHz	Baseline meters	Primary beam arcseconds	Array meters
5-20	$\geq 1-2$	145	$\leq 400-900$	$\geq 10-40$	$\leq 40-20$
5-20	$\geq 1-2$	220	$\leq 400-900$	$\geq 10-40$	$\leq 40-20$
5-20	$\geq 1-2$	265	$\leq 400-900$	$\geq 10-40$	$\leq 40-20$

Table 6.2: Optimum Instrumental configuration for detecting the signal for an interferometric experiment. The specifications equally apply to a single dish experiment.

size of the synthesized beam (Bruce Partridge, private communication). This limits the size of the primary beam to be $\geq 10-40$ arcseconds. From the size of the primary we can determine the array sizes at specified frequencies in Column 3. Column 6 shows the physical scale of the array that is required for the experiment.

7.0 CROSS-CORRELATION ANALYSIS

In this Chapter, I will describe the results that have been obtained by cross-correlating CMB temperature maps from WMAP and SDSS quasars. In §7.1 I will describe the datasets. In §7.2 I will describe the methodology. In §7.3 I will discuss the systematics involved in the problem. Section 7.4 will be devoted to describing the results obtained from this analysis. In §7.5 I will compare my results with theory.

The cross-correlation function and its Fourier transform, the cross-power (Peebles 1980) has been used as a powerful technique in cosmology to study different physical effects throughout the thermal history of the universe. The cross-correlation of CMB data sets with galaxy surveys has been a promising tool for studying secondary effects in the CMB (e.g., Refregier, Spergel, & Herbig 2000; Peiris & Spergel 2000; Fosalba, Gaztanaga, & Castander 2003; Afshordi, Loh, & Strauss 2003; Padmanabhan et al. 2005b; Ho et al. 2008, Giannantonio et al. 2008; Hirata et al. 2004; Smith, Zahn, & Dore 2007; Diego, Silk, & Sliwa 2003; Cheng, Wu, & Cooray 2006; Croft, Banday, & Hernquist 2006; Hernandez-Monteagudo et al. 2006; Ho, Dedeo, & Spergel 2009). In the current work we use the cross-correlation technique to detect SZ distortion from quasars.

7.1 DATA SETS

Our data sets are described in the four subsections which include the CMB temperature maps, the SDSS quasar and luminous red galaxy (LRG) catalogs, and the NVSS radio catalog.

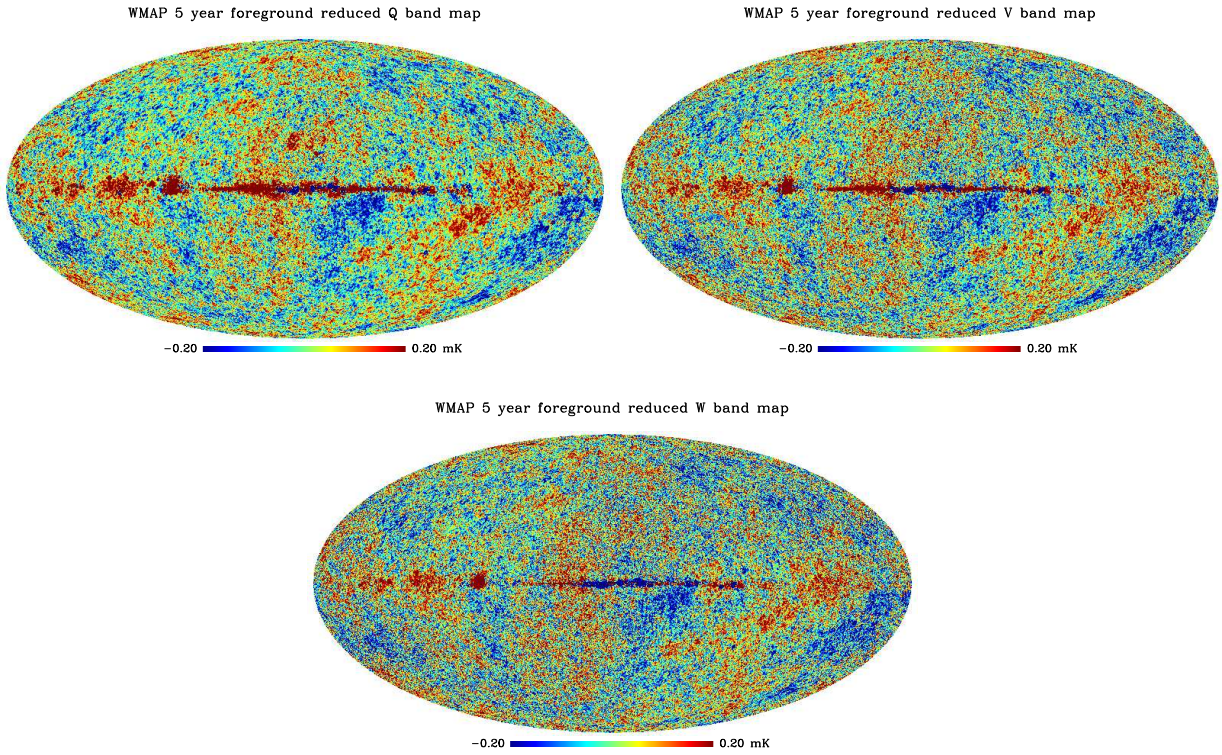

Figure 7.1: Mollweide projections in galactic coordinates (the galactic plane lies along the equator) of the sky in Q, V and W bands. The temperature units are in mK. These are the foreground reduced 5 year temperature maps. Data credit: Gold et al. (2009) (WMAP science team). The raw maps for all the bands are shown in Fig. 2.2 and are taken from Hinshaw et al. (2009). Courtesy: NASA arxiv: LAMBDA[1].

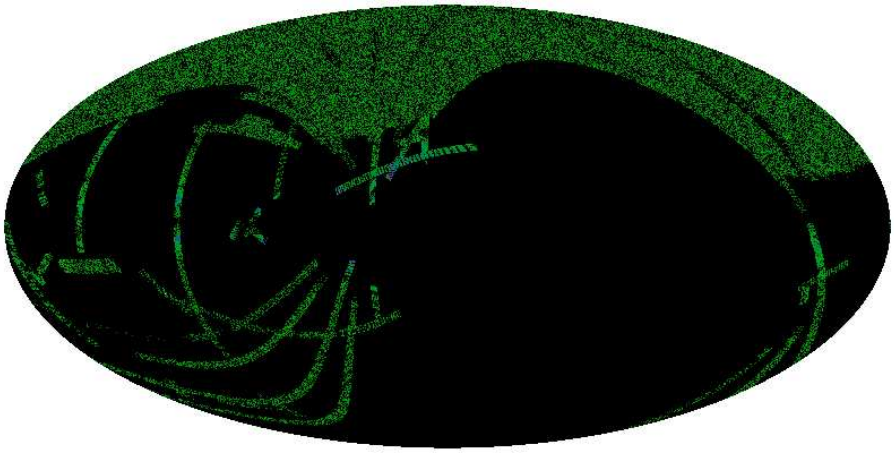

Figure 7.2: Mollweide projection (in galactic coordinates) of the positions of the quasars on the sky. Data credit: SDSS team: Catalog taken from Ho et al. (2008).

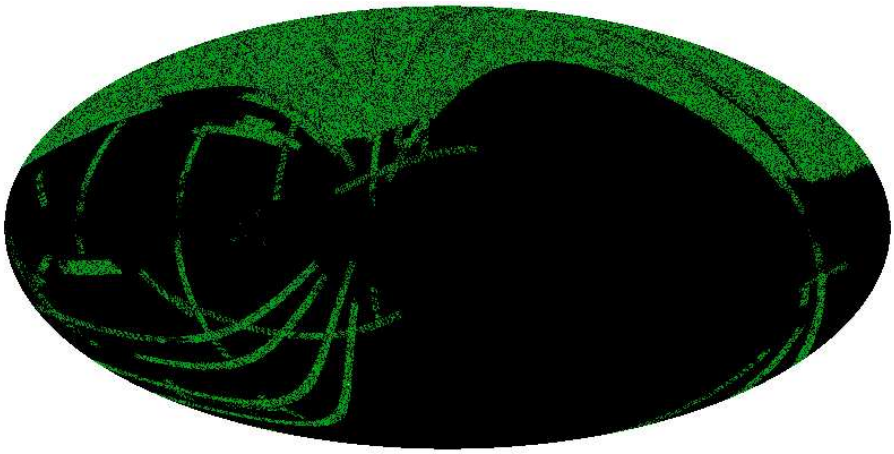

Figure 7.3: Mollweide projection (in galactic coordinates) of the positions of the LRGs on the sky. Data credit: SDSS team: Catalog taken from Ho et al. (2008).

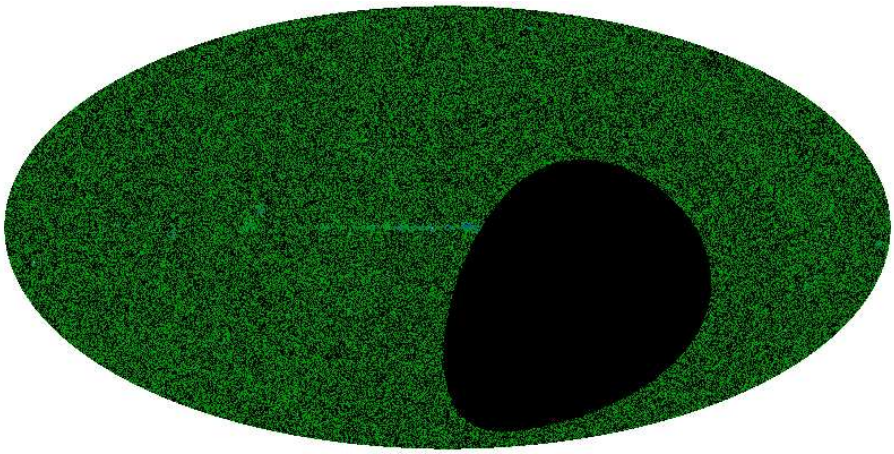

Figure 7.4: Mollweide projection (in galactic coordinates) of the positions of the NVSS objects on the sky. Data credit: Condon et al. 1998. Courtesy: NRAO

7.1.1 WMAP Temperature Maps

The WMAP satellite made a map of the microwave sky in 5 frequency bands with an angular resolution ranging from 0.88 degrees to 0.22 degrees. These correspond to approximate l values ranging from 250 to 900. We have used the WMAP 5 year maps for K (23 GHz), Ka (33 GHz), Q (41 GHz), V (61 GHz), and W (94 GHz) bands. These maps use the HEALPix pixelization scheme developed by Gorski et al. (2000). We have used the resolution 9 HEALPix maps for our analysis. This corresponds to a total of 3145728 pixels with each pixel being 47.2 square arc minutes in area. The maps are for each differencing assembly (DA) (Bennett et al. 2003) configuration and we combine them to get the full frequency maps. The number of DA(s) for K and Ka bands are one, Q and V bands are two and W band is four. The CMB temperature maps are shown in Fig. 7.1 in galactic coordinates in Mollweide projection. A Mollweide projection is a pseudocylindrical map projection used for global or sky representation.

7.1.2 SDSS Quasar Catalog

SDSS has done 5 band (u (3500 Å), g (4800 Å), r (6250 Å), i (7700 Å), z (9100 Å)) photometry (Fukugita et al. 1996) of about 10000 square degrees of sky area. We use the catalog developed by Ho et al. (2008). Three additional maps of (i) a Full Width Half Maxima (FWHM) map of the point spread function (PSF), (ii) a stellar density map (iii) A stellar density map, using the red stars with a (g-r) greater than 1.4, were used to clean the dataset from stellar contamination and mask out regions that are affected due to poor seeing. The quasars are selected photometrically using a prescription similar to Richards et al. (2006). The selection was done by generating a candidate quasar catalog of Ultra-Violet excess (UVX) objects. The observed g magnitudes of these objects are fainter than 14.5 and the extinction corrected g magnitudes are brighter than 21.0. The $u - g$ magnitude is less than 1.0. The catalog was made by matching the DR3-quasar catalog with the DR3-UVX objects (See Ho et al. 2008 for details). In the current data set the PSF magnitudes are used for the quasars. The redshifts of the quasars lie between $0.08 - 2.82$ with a median redshift of 1.4 (see Ho et al. 2008 for the redshift distribution). In Fig. 7.2 the Mollweide projection of the quasars on the sky in galactic coordinates are shown.

7.1.3 SDSS Luminous Red Galaxy Catalog

The LRGs are useful mass tracers in the universe. The catalog we used here is described in Ho et al. (2008). The catalog is constructed using the prescription given in Padmanabhan et al. (2005a). The exact redshifts of the objects were estimated using photometric redshifts and the corresponding error distribution of the sample (Ho et al. 2008). Table 7.1 gives a brief description of the LRG catalog and the quasar catalog that are used for the current analysis. The magnitudes of the LRGs are model magnitudes which are different from the quasar magnitudes. The redshifts of the LRGs lie between $0.4 - 0.6$ with a median redshift of 0.5 (see Ho et al. 2008 for the redshift distribution). Fig. 7.3 shows the Mollweide projection of the LRGs on the sky in galactic coordinates.

Catalog	Redshift	Area (deg^2)	Objects
Quasar catalog	0.08-2.82	6039	586435
LRG catalog	0.4-0.6	6641	911686
NVSS	0-3.0	27361	1104983

Table 7.1: Description of the SDSS and NVSS catalogs. Column 2, Column 3, and Column 4 show the redshift ranges, sky coverages, and the total number of objects in the catalogs.

7.1.4 NVSS Catalog

NVSS is a 1.4 GHz continuum sky survey with the VLA. It covers the region that lies north of $\delta = -40^{\circ}$. The entire area is about 82 % of the celestial sphere. The catalog has about 2×10^6 discrete objects with a full width half maximum of $45^{''}$ and a nearly uniform sensitivity. The error in the right ascension (RA) and the declination (DEC) varies from $< 1^{''}$ for 15 mJy sources and above at 1.4 GHz, to about $7^{''}$ for sources nearing the survey limit (2 mJy at 1.4 GHz) (Condon et al. 1998). The redshifts of the NVSS sources lie between $0 - 3.0$ with a median redshift of 1 (see Ho et al. 2008 for the redshift distribution). In Fig. 7.4 we show the Mollweide projection of the positions of the NVSS objects in galactic coordinates.

7.2 METHODOLOGY

7.2.1 Cross-Correlation Amplitude

The Compton y-parameter, given in Eq. 2.54, characterizing the SZ spectral distortion is proportional to the line-of-sight integral of the electron pressure. The effective temperature distortion at a frequency ν is given in Eq. 2.56. The corresponding intensity change is given in Eq. 2.58. Since the SZ effect can be used as a tool to measure electron density weighted temperature of the intracluster medium, we use it as a diagnostic to detect feedback effects

Band GHz	Conversion factor Jansky/Steradian
K (23)	1.65×10^7
Ka (33)	3.37×10^7
Q (41)	5.13×10^7
V (61)	10.63×10^7
W (94)	22.35×10^7

Table 7.2: Conversion factors between flux and temperature. The constant $i_0 = 2.7 \times 10^{-15}$ ergs/sec/cm^2/Hz/Steradian and 1 Jansky = 10^{-23} ergs/sec/cm^2/Hz

from quasars. We stack the quasars in the WMAP temperature maps, and the estimated amplitude of the signal from quasars (ΔT_{quasar}) is given as follows:

$$\Delta T_{quasar} = \frac{\sum_i N_i T_i}{\sum_i N_i}, \tag{7.1}$$

where T_i is the temperature of the ith pixel in the temperature maps and N_i is the number of quasars in the ith pixel. We expect an anti-correlation between quasar number in a pixel and the corresponding average temperature signal at WMAP frequencies since they are all below the null frequency of the SZ spectrum (see Fig. 2.5). This manifests as a cold spot in the temperature maps.

7.2.2 Temperature to Flux

The temperature values in the maps are thermodynamic temperatures. To go from the thermodynamic temperature to flux we need to do the following conversion using Eq. 2.55.

$$\Delta I = i_0 \frac{x^4 e^x}{(e^x - 1)^2} \frac{\Delta T_{quasar}}{T_{CMB}}, \tag{7.2}$$

where $x = h\nu/(K_B T_{CMB}) = 0.0176\nu$ (in GHz). The conversion factors are shown in Table 7.2. In Fig. 7.5 we show the spectrum of the cross-correlation estimator (Eq. 7.1) using the raw WMAP maps shown in Fig. 2.2.

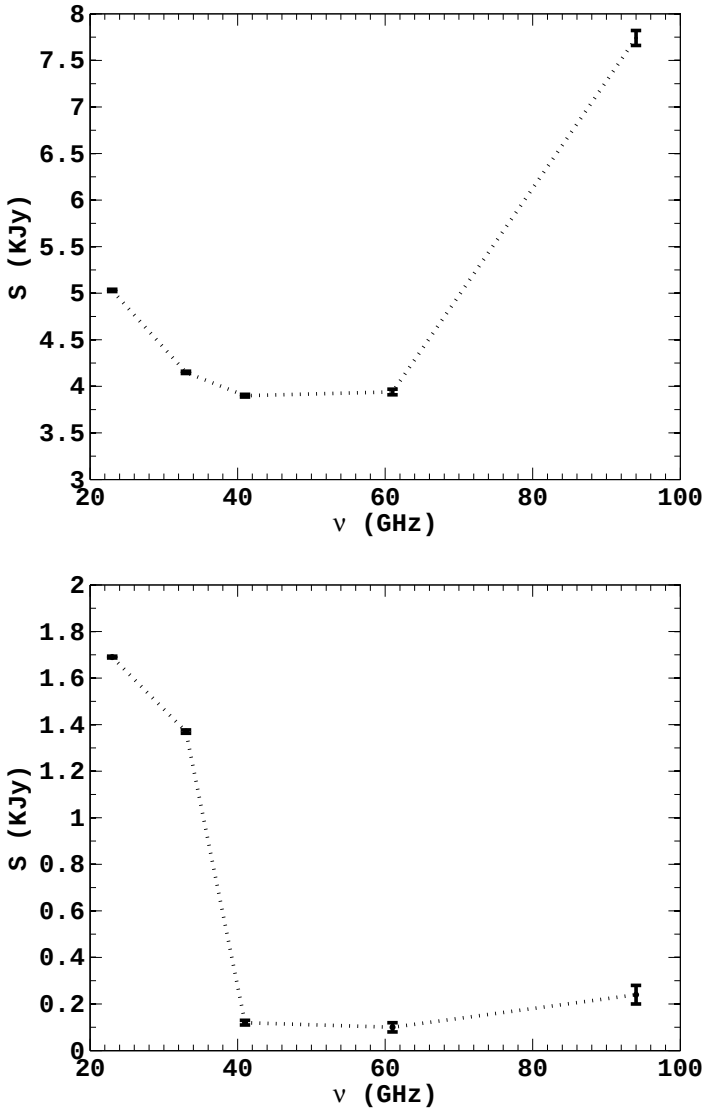

Figure 7.5: The cross-correlation spectrum using the raw WMAP 5 year maps. The top panel of the figure shows the level of foregrounds in the CMB temperature maps. WMAP foregrounds are described in Section 7.3.1. At lower frequencies there will be contribution from Galactic synchrotron ($S \propto \nu^{-1}$). At high frequencies emissions from dust will be predominant ($S \propto \nu^{4}$). The another prominent source of contamination is free-free emission from charged particles ($S \propto \nu^{-0.1}$). These effects are evident from the shape of the spectrum. The bottom panel shows the same spectrum after applying the dust mask described in Section 7.3.2.

7.3 SYSTEMATICS

We identify a number of systematic effects in the expected SZ signal as is evident from Fig. 7.5.

7.3.1 WMAP Foregrounds

The primary foregrounds in the WMAP temperature maps come from Galactic radio emissions. These radio emissions arise largely from three sources. "Non-thermal" synchrotron emission from relativistic electrons in the presence of magnetic fields, free-free emission from charged particles, and the rotational, and vibrational emissions from dust molecules (see Gold et al. 2009). At lower frequencies, synchrotron emission ($S \propto \nu^{-1}$) is important with flux decreasing at higher frequencies following a power law. The free-free has almost a frequency independent spectrum ($S \propto \nu^{-0.1}$), and hence it becomes more relevant at higher frequencies. At frequencies higher than 60 GHz the emissions from vibrational modes of dust molecules contribute significantly and are prominent at frequencies around 90 GHz ($S \propto \nu^{4}$) (Gold et al. 2009). From Fig. 7.5 we see these trends in the spectrum. All these emissions will positively bias the signal and lead to an underestimate of the decrement from the SZ effect. We use the foreground reduced maps to reduce Galactic foreground contaminations (see Gold et al. 2009, for the detailed description of foreground reduction). The foreground reduced maps are available for Q, V and W bands. Table 7.3 gives the flux values for the foreground reduced cases.

7.3.2 Effect of Dust

Dust systematically affects our signal and we need to correct for this. The effect of dust is two-folded. Regions in SDSS with higher dust extinction will lead to a selection bias of the sample. On the other hand, dust emission in WMAP bands will also contaminate our signal (as described in Section 7.3.1). The foreground reduced maps will correct for the dust extinction but we need to mask out regions in SDSS which are heavily affected by dust. To do this we use the prescription described in Ho et al. (2008). Using the SFD

Band GHz	Raw map kJy	Foreground Reduced kJy
Q (41)	3.90 ± 0.015	0.68 ± 0.01
V (61)	3.94 ± 0.03	1.00 ± 0.02
W (94)	7.74 ± 0.08	1.77 ± 0.05

Table 7.3: The values of the cross-correlation estimator for the SDSS quasars, using the foreground reduced maps. The second Column gives the corresponding values for the raw maps and the third Column shows the values for the foreground reduced maps.

(Schlegel, Finkbeiner, & Davis 1998) extinction map we construct E(B-V) masks. We apply the E(B-V) mask to our SDSS and NVSS samples. In Fig. 7.6 we show the SDSS and NVSS samples after applying the dust masks. The bottom panel of Fig. 7.5 shows the quasar cross-correlation spectrum after applying the dust mask.

7.3.3 Radio Emission from Quasars

Another source of contamination in the signal will come from the radio emissions due to radio point sources (e.g., radio loud quasars). The spectral index of these radio loud sources is ~ 0.7 (see Carlstrom, Holder, & Reese 2002) and so at lower frequencies the radio contamination is a big issue. To understand the effect of the radio contamination we have matched the objects in the SDSS quasar catalog with the NVSS radio catalogs to search for radio counterparts of the Sloan quasars. We have selected all the objects that have fluxes higher than 2 mJy (at 1.4 GHz) and have counterparts in SDSS. We identify 30128 NVSS counterparts in SDSS. We mask out pixels containing these quasars in estimating the cross-correlation signal. We also perform the same cross-correlation with the NVSS objects. Note that the radio sources identified in the NVSS survey are bright radio sources. There could be contamination from faint sources in our analysis. The results for the NVSS cross-correlation are shown in Fig. 7.7. The NVSS results (top panel of Fig. 7.7) show a similar trend as the SDSS objects (top

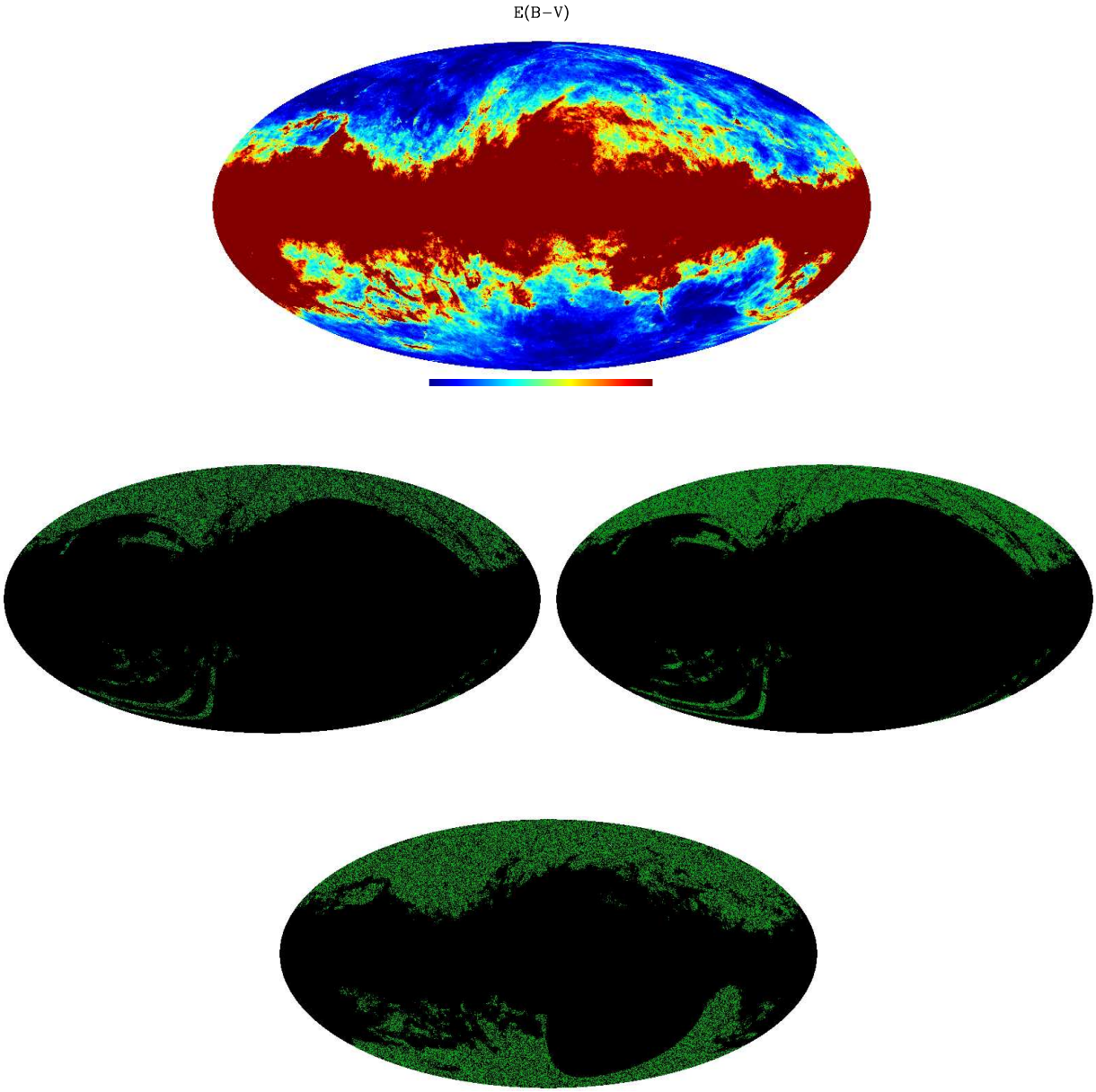

Figure 7.6: E(B-V) map (top panel) in Mollweide projection where red implies higher extinction. The middle left, middle right, and bottom panels show the quasar, LRG, and the NVSS catalogs, respectively, after we apply the $E(B-V) \geq 0.05$ mask. The data for the extinction map is taken from Schelgal, Finkbeiner, & Davis 1998. Courtesy: LAMBDA[1].

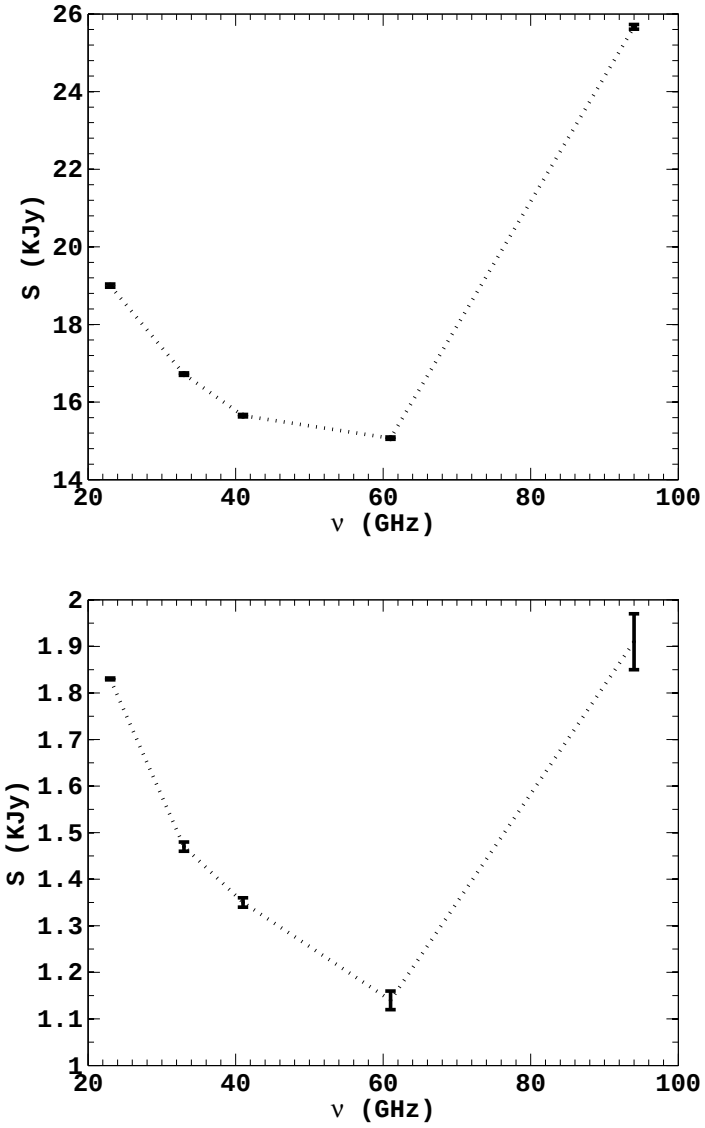

Figure 7.7: Cross-Correlation spectrum of the NVSS objects from the raw maps (top), and after applying the dust mask (bottom). Since the effect of dust is most pronounced around 90 GHz, it is quite evident from the figures that the dust mask reduces the systematic effects at 90 GHz. The top panel is similar to Fig. 7.5 (SDSS quasars) except for the absolute amplitude of the cross-correlation.

panel of Fig. 7.5). The bottom panel of Fig. 7.7 shows the NVSS cross-correlation spectrum after applying the $E(B-V) \geq 0.05$ mask. Once we use the dust mask the contamination in the 90 GHz channel is reduced substantially. The values for the estimator of the cross-correlation amplitude of the NVSS objects with the foreground reduced maps are shown in Table 7.4. We note that the foreground reduced maps show less flux in the 90 GHz band compared to Q and V bands. This is expected from the NVSS sources since they emit less at higher frequencies.

Band GH	Raw map kJy	Foreground Reduced kJy
Q (41)	15.65 ± 0.03	3.31 ± 0.01
V (61)	15.07 ± 0.03	3.32 ± 0.02
W (94)	25.67 ± 0.06	2.84 ± 0.04

Table 7.4: The values for the cross-correlation estimator are shown for the foreground reduced maps for the NVSS objects. The corresponding values for the raw maps are shown in Column 2.

7.3.4 Primary CMB and Detector Noise

One of the challenges in understanding this cross-correlation is the noise due to primary anisotropy and detector. The WMAP team used a spatial filter (Weiner filter) to obtain point source amplitudes from the temperature maps (Hinshaw et al. 2007). We use a similar filter to cut-off power at scales where primary CMB anisotropy and detector noise values are high. The filter is applied in harmonic space. The form of the filter is obtained with a maximum likelihood approach (Tegmark & de Oliveira-Costa 1998; Rashkov 2009: Thesis). The measured temperature at a position θ is given by $m(\theta)$, which can be written as a decomposition of the following components (after the other corrections described above):

$$m(\theta) = n(\theta) + \int s(\theta_1) W(|\theta - \theta_1|) d\theta_1 + P_0 W(\theta - \theta_p) \tag{7.3}$$

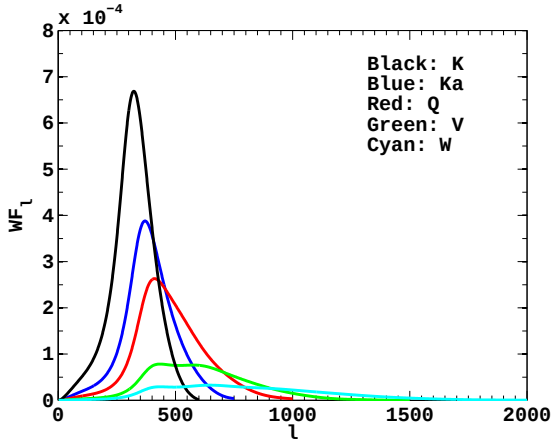

Figure 7.8: Forms of the filter functions given in Eqn. 7.9 in five frequency bands. The filter suppresses power at smaller (larger) and larger (smaller) angular scales (multipoles) to suppress detector noise and primary fluctuations.

where θ_p is the position of the point source with an amplitude P_0, and n, W, and s are the noise, beam and primary CMB signal values, respectively. The likelihood of having a point source amplitude P_0 is given by

$$\begin{aligned} -2Ln(L) &= (m(\theta_1) - P_0 W(\theta_1 - \theta_p))^T C(\theta, \theta_1)^{-1} \\ &\quad (m(\theta) - P_0 W(\theta - \theta_p)). \end{aligned} \tag{7.4}$$

We can write the beam in harmonic space as

$$W(\theta_1 - \theta_p) = \sum_{lm} Y^{\star}_{lm}(\theta_1) W_l Y_{lm}(\theta_p), \tag{7.5}$$

and the covariance term can be written as

$$C(\theta, \theta_1) = \sum_{lm} Y^{\star}_{lm}(\theta_1) C_l Y_{lm}(\theta), \tag{7.6}$$

where $C_l = s_l W_l^2 + n_l$. From Eq. 7.4, 7.5 and 7.6 we get

$$-2Ln(L) = \frac{\sum_{lm} |m_{lm} - P_0 W_l Y_{lm}(\theta_p)|^2}{C_l}. \tag{7.7}$$

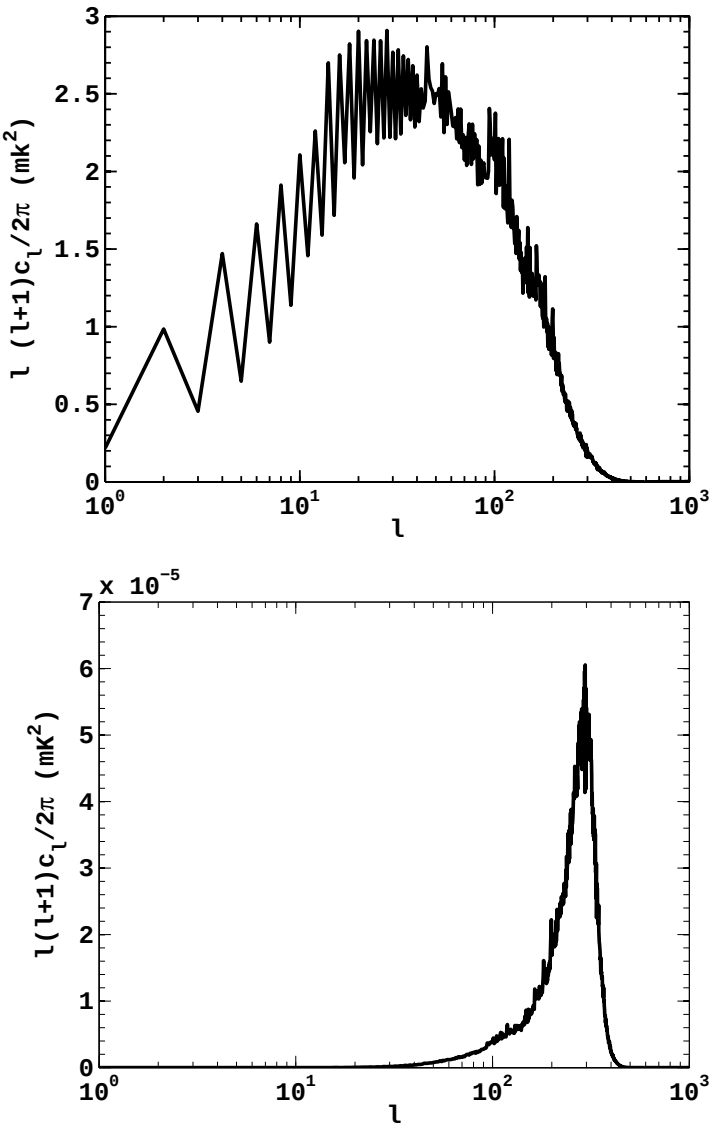

Figure 7.9: Effect of Weiner-filtering the CMB maps. The top panel shows the power spectrum (power as a function of multipoles (angular scales)) of the unfiltered map in K (23 GHz) band. The bottom panel shows the power spectrum of the filtered map. The goal of our filters is to minimize the contamination from primary CMB anisotropies at large angular scales (lower multipoles), and detector noise at smaller angular scales (larger multipoles). This effect is evident from the figure. The filters are of the form described in Eq. 7.9 (shown in Fig. 7.8)

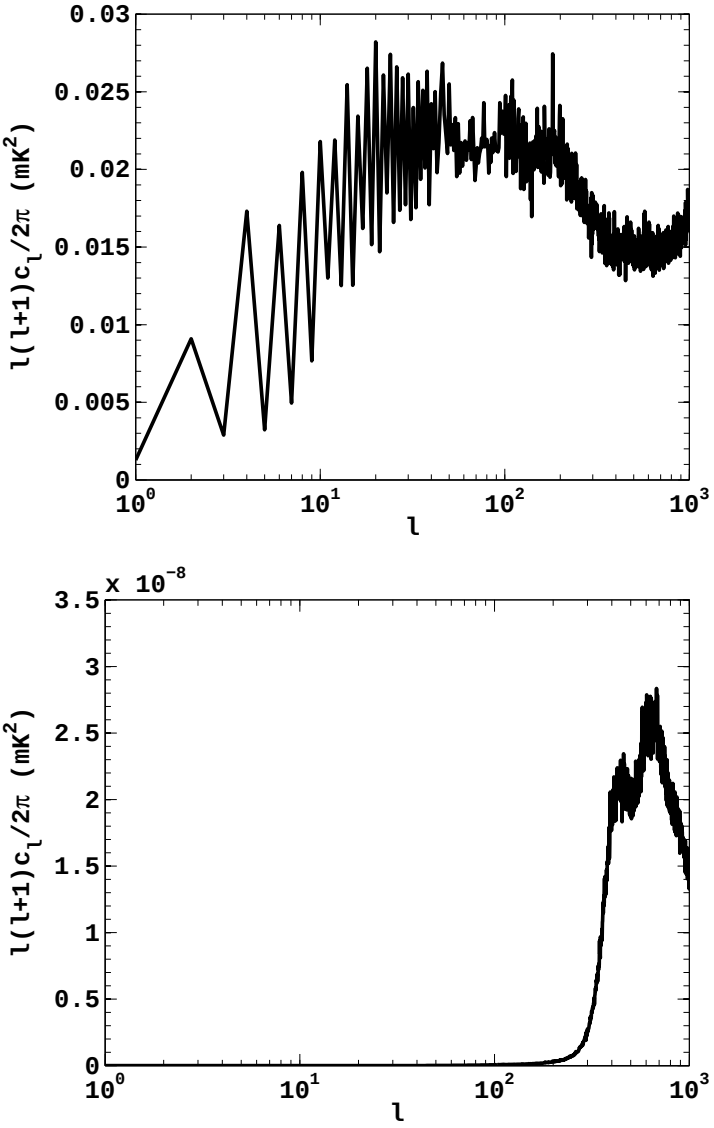

Figure 7.10: Effect of Weiner-filtering the CMB maps. The top panel shows the power spectrum (power as a function of multipoles (angular scales)) of the unfiltered map for the W (94 GHz) band. The bottom panel shows the power spectrum of the filtered map. The goal of our filters is to minimize the contamination from primary CMB anisotropies at large angular scales (lower multipoles), and detector noise at smaller angular scales (larger multipoles). This effect is evident from the figure. The filters are of the form described in Eq. 7.9 (shown in Fig. 7.8).

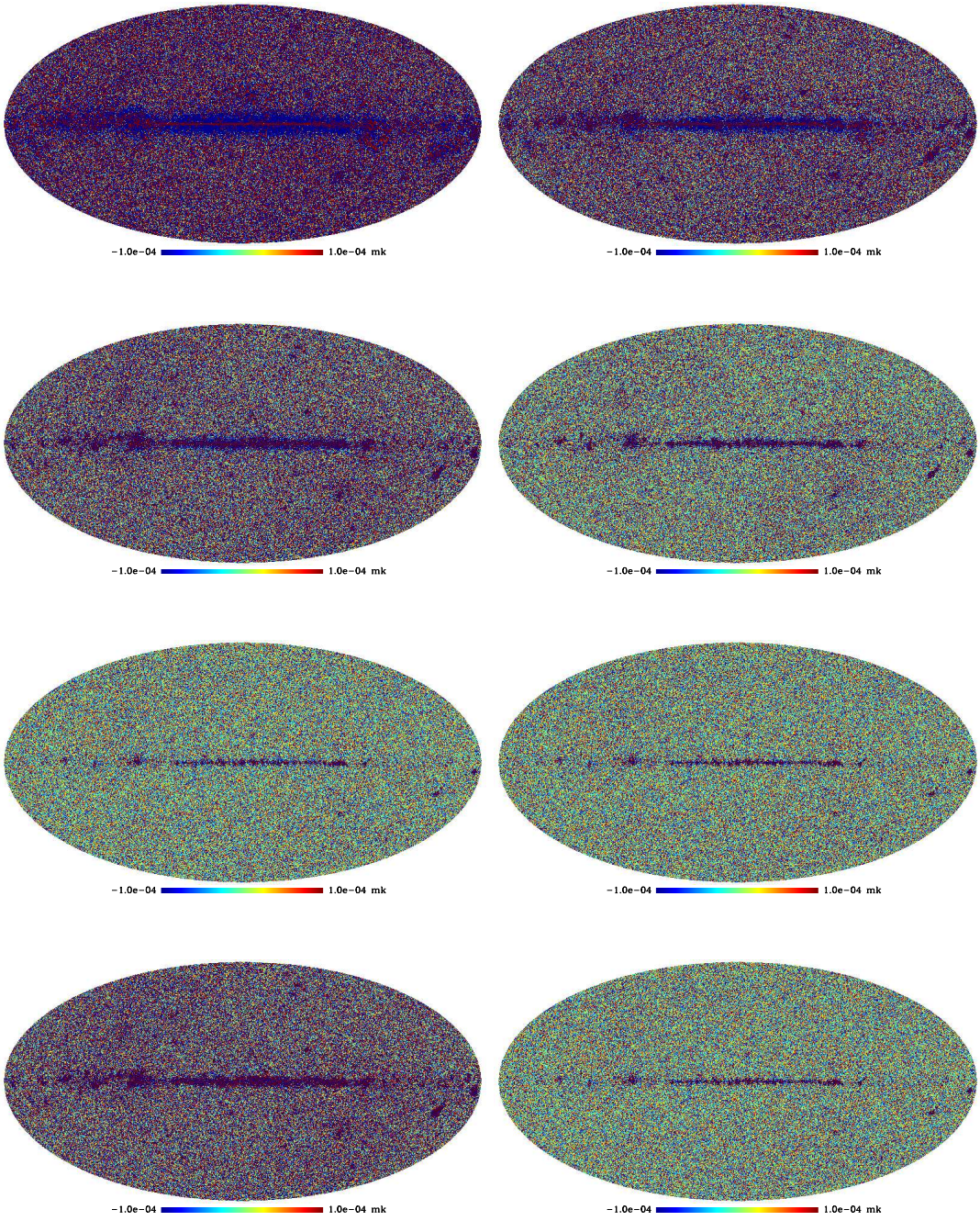

Figure 7.11: Filtered maps for the five bands. The maps are for K (top left), Ka (top right), Q (second left), V band (second right), and W (third left) bands. The filtered maps for the foreground reduced cases are also shown. The foreground reduced filtered maps are for the W band (third right), Q band (bottom left), and V band (bottom right). The units are in mK.

Differentiating with respect to P_0 and equating it to zero we get the estimate of the amplitude of the point source (quasars in our case) as

$$P_0 = \frac{\sum_{lm} \frac{m_{lm} W_l Y_{lm}(\theta_p)}{C_l}}{\sum_l \frac{W_l^2}{C_l} Y_{lm}(\theta_p) Y_{lm}(\theta_p)}. \tag{7.8}$$

With the orthonormality relation of the Spherical harmonics we have

$$\begin{aligned} P_0 &= \frac{4\pi \sum_{lm} \frac{m_{lm} W_l Y_{lm}(\theta_p)}{C_l}}{\sum \frac{(2l+1) W_l^2}{C_l}} \\ &= \sum_{lm} WF_l m_{lm} Y_{lm}(\theta_p). \end{aligned} \tag{7.9}$$

WF_l in Eq. 7.9 gives the form of the Weiner filter, where $C_l = c_l W_l^2 + n_l$, and c_l, W_l, and n_l are primary CMB, beam transfer function, and detector noise values respectively. The

Band GH	l_{max}	σ_0 mK	$\bar{N}$
K (23)	600	1.44	725.8
Ka (33)	750	1.47	725.6
Q (41)	1000	2.20	1817.2
V (61)	1500	3.13	2443.2
W (94)	2000	6.54	7339.5

Table 7.5: Noise values for WMAP. The noise per pixel is given as $n = \sigma_0/\sqrt{\bar{N}}$. The σ_0 values are shown for typical DAs (WMAP explanatory supplement: Limon et al. 2009[1]). To calculate the noise, the equivalent steradians of the pixel should be considered. Each HEALPix resolution-9 pixel is 47 square arc minute equal to 4×10^{-6} steradians. Column 2 also shows the l_{max} values used for constructing the filters for each band.

primary CMB c_l values are calculated using CAMB (Lewis, Challinor, & Lasenby 2000). The detector noise is calculated using the noise values for WMAP ($n = \sigma_0/\sqrt{\bar{N}}$) and the beam transfer functions (W_l) are taken from Page et al. (2003). The noise values should be converted into steradians to be consistent. The values are given in Table 7.5 (Rashkov 2009:

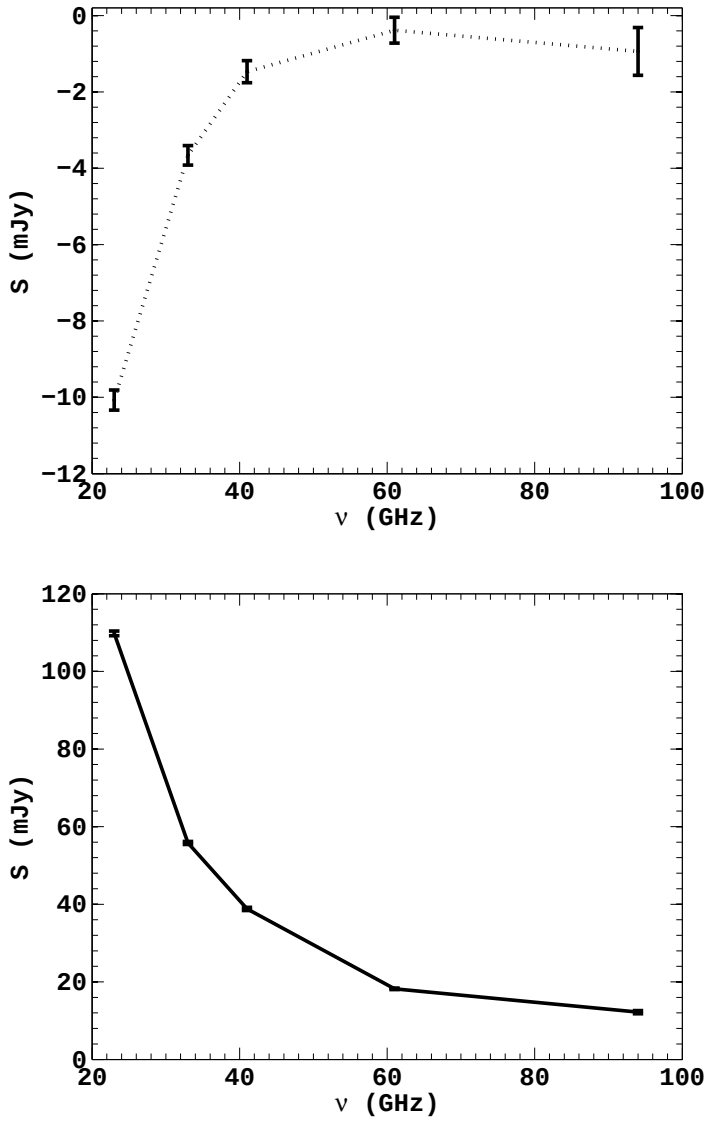

Figure 7.12: The cross-correlation spectrum from the filtered maps. The top panel shows the spectrum for the SDSS quasars, and the bottom panel shows the same cross-correlation spectrum for the NVSS objects. The results are shown for the raw maps. The flux for the NVSS sources fall-off with frequency. The flux corresponding to the quasars (top panel) show deficit, which is expected if we are detecting SZ effect. However the spectrum does not correspond to SZ decrement and we need to analyze further to investigate this effect.

Thesis). The maximum l values (shown in Table 7.5) that we have used for constructing the filters for different frequencies depend on the angular resolutions of the corresponding bands. Fig. 7.8 shows the shapes of the filter functions (WF_l) in five frequency bands. Figures 7.9 and 7.10 show the effect of the filter function on the power spectrum. We compute the power spectrum from the raw maps and the filtered maps to see the effect of the filters. It is quite evident from Figs. 7.9 and 7.10 that the filter suppresses power at lower and higher angular scales. The results are shown for the K band (Fig. 7.9) and the W band (Fig. 7.10). Figure 7.11 shows the filtered maps. Note that the maps are not normalised. To get the correct amplitude of temperature for the power spectrum and the maps in Figs. 7.9, 7.10, and 7.11 we need to multiply the values by the beam normalisation $\sum_l (2l+1)W_l$ (see Rashkov 2009 thesis).

7.4 RESULTS

7.4.1 Cross-Correlation Spectrum

In Fig. 7.12, we show the cross-correlation spectrum obtained from the filtered maps for the SDSS quasars (top) and NVSS objects (bottom). The fluxes of the sources are typically mJys at WMAP frequencies. This result is consistent with the typical fluxes of WMAP point sources described in Hinshaw et al. (2007) and Wright et al. (2009). The spectrum of the NVSS sources fall-off with frequency. The fluxes for the SDSS quasars tend to be negative. Although we expect decrement due to SZ effect at these frequencies for the quasars, we prefer to investigate further to see if the negative flux signature is coming from the SZ distortion or it is coming from some random fluctuations.

We now apply the dust mask and the radio mask (SDSS objects only) to our objects to see the effect on the cross-correlation spectrum. The results are shown in Fig. 7.13. The top panel shows the spectrum for the SDSS quasars and the bottom panel shows the spectrum for the NVSS sources. The dashed line shows the fit to the spectrum for SZ (Eq. 2.52) and the solid line shows the fit with dust ($\sim \nu^4$) and SZ. The fits for the parameters, reduced χ^2

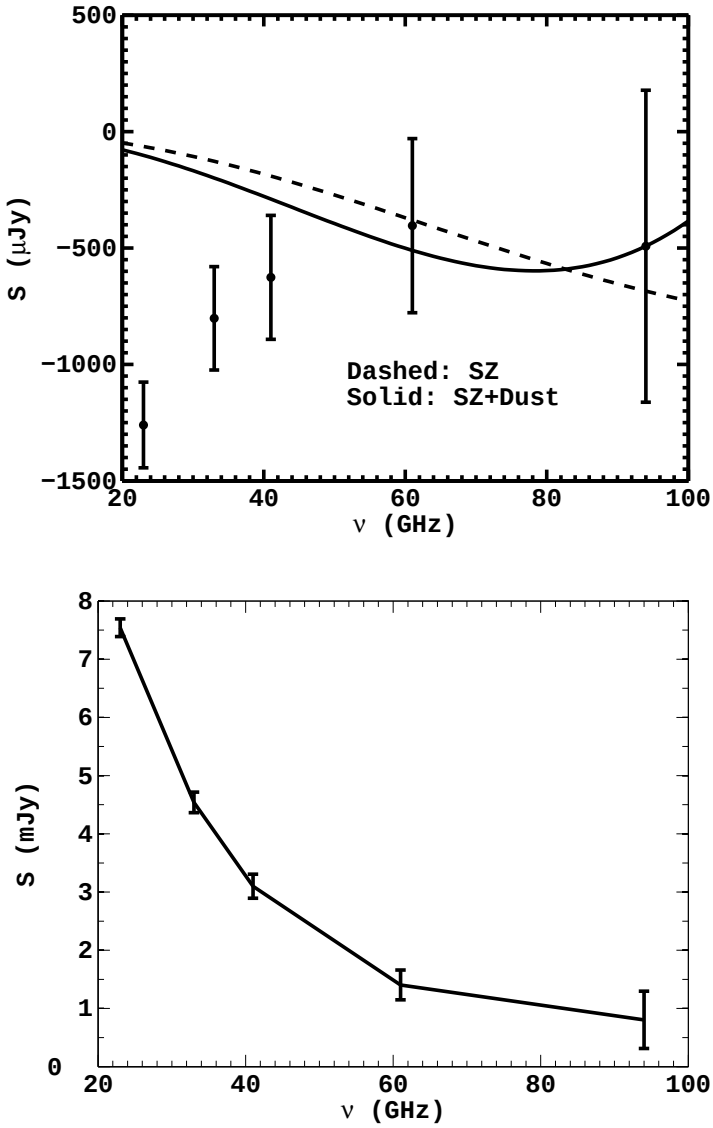

Figure 7.13: The cross-correlation spectrum from the filtered maps using masks. The top panel shows the spectrum for the SDSS quasars where we have used the dust and radio masks described in §7.3. The bottom panel shows the spectrum of the NVSS sources after applying the dust mask on the filtered maps. The dashed and solid lines in the top panel are fits for two models to the spectrum. The dashed line corresponds to SZ and the solid line is a two-component fit involving dust and SZ. The best-fit values of the parameters and the reduced χ^2 values are listed in Table 7.6. The first two rows in Table 7.6 correspond to the fits shown in the top panel of this figure.

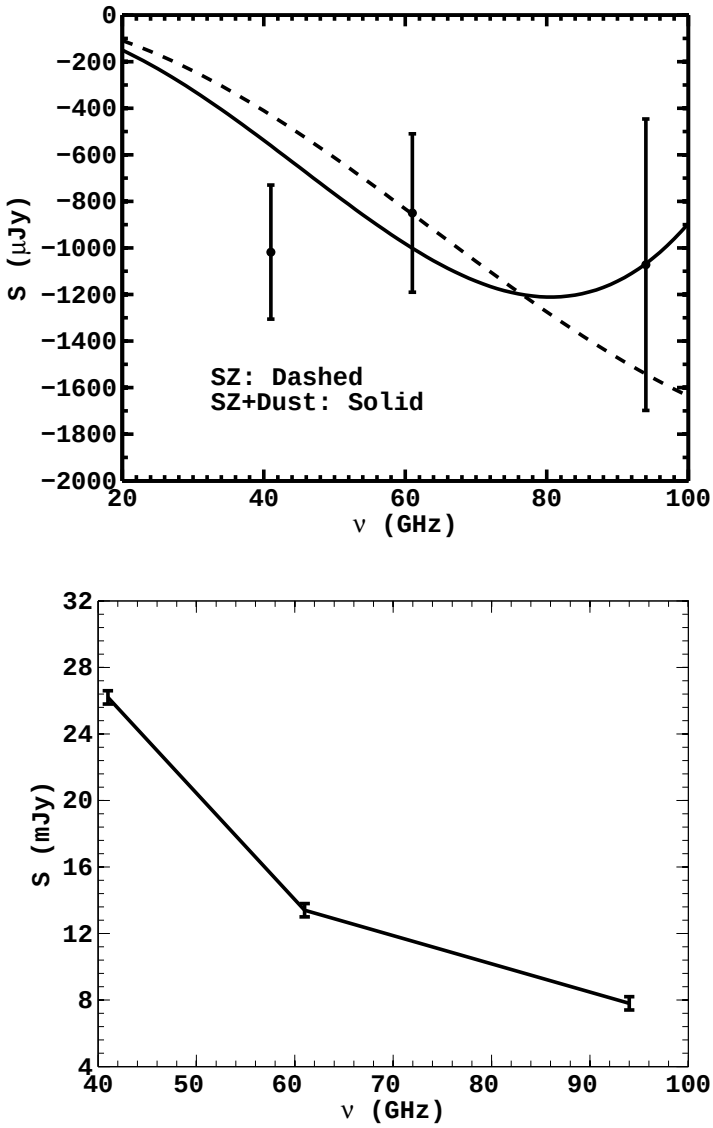

Figure 7.14: The cross-correlation spectrum from the foreground reduced filtered maps using masks. The top panel shows the spectrum for the SDSS quasars and the bottom panel shows the spectrum of the NVSS sources. The dashed and solid lines in the top panel are fits for two models to the spectrum. The dashed line corresponds to SZ and the solid line is a two-component fit involving dust and SZ. The best-fit values of the parameters and the reduced χ^2 values are listed in Table 7.6. The third and fourth rows in Table 7.6 correspond to the fits shown in the top panel of this figure.

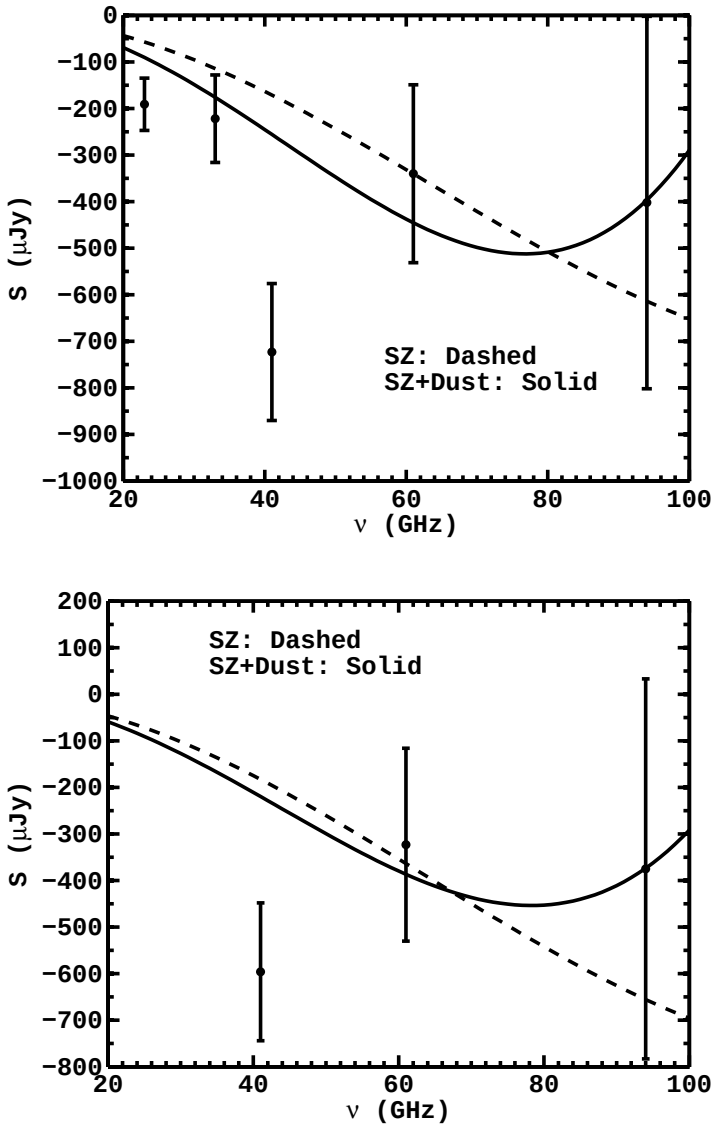

Figure 7.15: Cross-correlation spectrum for the SDSS quasars after removing the pixels with higher values of temperature distortion. The figure shows the same cross-correlation as shown in the top panels of Figs. 7.13 and 7.14 after removing pixels with higher values of temperature. The top panel shows the spectrum from the raw maps with the masks and the bottom panel shows it for the foreground reduced maps using similar masks. The dashed line corresponds to a fit for SZ and the solid line is a two component fit involving SZ and dust. The best-fit values of the parameters and the reduced χ^2 values are listed in Table 7.6. The fifth and sixth rows in Table 7.6 correspond to the fits shown in the top panel of this figure, and the seventh and eighth rows in Table 7.6 correspond to the fits shown in the bottom panel of this figure.

Sample	Model	Fits (μJy)	χ^2 Reduced	BIC
Top panel of Fig. 7.13	SZ	$i_0y = 200.1 \pm 176.3$	13.56	58.70
	SZ+Dust	$i_0y = 327.5 \pm 197.5$ $A = 84 \pm 12$	16.23	51.90
Top panel of Fig. 7.14	SZ	$i_0y = 450.3 \pm 294.2$	2.76	6.93
	SZ+Dust	$i_0y = 628.6 \pm 199.3$ $A = 144.7 \pm 18.1$	2.01	3.82
Top panel of Fig. 7.15	SZ	$i_0y = 179.3 \pm 143.4$	5.36	27.85
	SZ+Dust	$i_0y = 290.5 \pm 101.6$ $A = 79.8 \pm 6.3$	4.62	17.08
Bottom panel of Fig. 7.15	SZ	$i_0y = 191.5 \pm 174.8$	4.15	10.50
	SZ+Dust	$i_0y = 248.1 \pm 106.4$ $A = 63.5 \pm 5.2$	6.55	8.75

Table 7.6: Fits for the y parameter. To evaluate the errors on the parameters we resimulate the data with a Gaussian distributions of errors and an RMS value centered on the original values of the errors. We then fit these random realizations and calculate the standard deviation of the parameters to quote the error on a given parameter. The comparison of these values with the theoretical models are described in §7.4.2. The first two rows correspond to fits for the filtered raw maps with the masks. The third and fourth rows correspond to the fits for the foreground reduced cases. The last four rows correspond to the fits after removing pixels that have high values ($\geq 10\mu$K and $\leq -10\mu$K) of temperature distortion. The first Column in the table points to the relevant figure of interest. The reduced χ^2 values are extremely high for the first two rows. The fits for the foreground reduced case looks reasonable (third and fourth rows). The Bayesian Information Criterion (BIC) values reduces for the two-component fits which justifies the inclusion of the dust parameter.

values, and the Bayesian Information Criterion (BIC = $\chi^2 + k\log(n)$; k: degrees of freedom; n: number of data points; Liddle, Mukherjee, & Parkinson 2006) values are displayed in Table 7.6. The errors on the fit parameters are generated in the following way. We resimulate the data by drawing an error from a Gaussian distribution with root-mean-squared values given by the standard errors in the estimated signal for each band calculated from the variance in ΔT and number of pixels used for averaging. The error-bars on the fit parameters are the 1σ values obtained from the fits to the simulated datasets. The BIC values are lower for the two-component fits which suggest that inclusion of dust improves the fits significantly. The fluxes of the NVSS objects fall-off with frequency. This result is consistent with Boughn & Partridge (2008). We also show the spectrum for the foreground reduced maps in Fig. 7.14. For the foreground reduced cases the χ^2 values improve significantly. The BIC values also indicate that the inclusion of the dust parameter improves the fits. We also calculate the

Band GH	Correlation values μJy	Mean of random values μJy
K (23)	-1260.2	223.8
Ka (33)	-802.4	44.0
Q (41)	-626.4	-82.3
V (61)	-404.8	-16.2
W (94)	-492.2	52.7
QF	-1018.3	5.1
VF	-850.6	-38.4
WF	-1072.4	-15.9

Table 7.7: Mean values of the cross-correlation estimator for the five frequency bands for a thousand random realizations of the quasar positions. QF, VF, and WF represent the foreground reduced cases. Column 2 shows the values of the estimator for the quasars and Column 3 shows the mean values of the estimator for a thousand random realizations of quasar positions.

probability of getting χ^2 values higher than the ones we obtain from our fits by calculating

the probability density functions (PDF). We use the inbuilt IDL function $CHISQR_{PDF}$ to calculate the probabilities. All the possibilities are ruled out except for the case shown in Fig. 7.14 (Row 4 of Table 7.6), where the fits are consistent with the data. To investigate the high negative values in K and Ka bands, we employ the following technique. We mask out pixels that have temperature values greater than $10\mu K$ and less than $-10\mu K$ in our temperature maps at all frequencies. This reduces our sample size by 14%. We then estimate the cross-correlation. The results are shown in Fig. 7.15. The top panel shows the spectrum for the raw maps with the dust and radio masks and the bottom panel shows the plot for the foreground reduced maps with the dust and radio masks. The fits are shown in Table 7.6.

7.4.2 Significance of Cross-Correlation

To see the significance of the correlation we randomize the positions of the quasar(s), and calculate the value of ΔT_{quasar} for a thousand realizations. We calculate the mean value of the anti-cross-correlation amplitude obtained from the thousand random realizations of quasar positions. The mean values are shown in Table 7.7. We also find that in $0.01-6\%$ cases (from K through W bands) the correlation amplitude is more prominent than the real sample. This shows that the quasars are significantly anti-correlated with WMAP temperature pixels.

7.4.3 SZ Signal from Galaxy Clusters

One of the major contamination to the signal is the SZ effect from galaxy clusters. There have been reported evidences of detection of this SZ effect in WMAP temperature maps (Bennett et al. 2003; Hernandez-Monteagudo et al. 2006; Spergel et al. 2007; Diego & Partridge 2009; Myers et al. 2004) and theoretically the signal is $2-3$ orders of magnitude higher than the SZ effect from quasars. To study the effect from galaxy clusters we stack SDSS LRGs and estimate the same cross-correlation using the filtered maps with the same masks. The cross-correlation spectrum is shown in Fig. 7.16. The amplitude and shape of the distortion is very similar to the quasar case shown in the top panels of Figs. 7.13 and 7.14. The similarities in the cross-correlation spectrums of quasars and LRGs suggest that both the signals might be coming from the same effect.

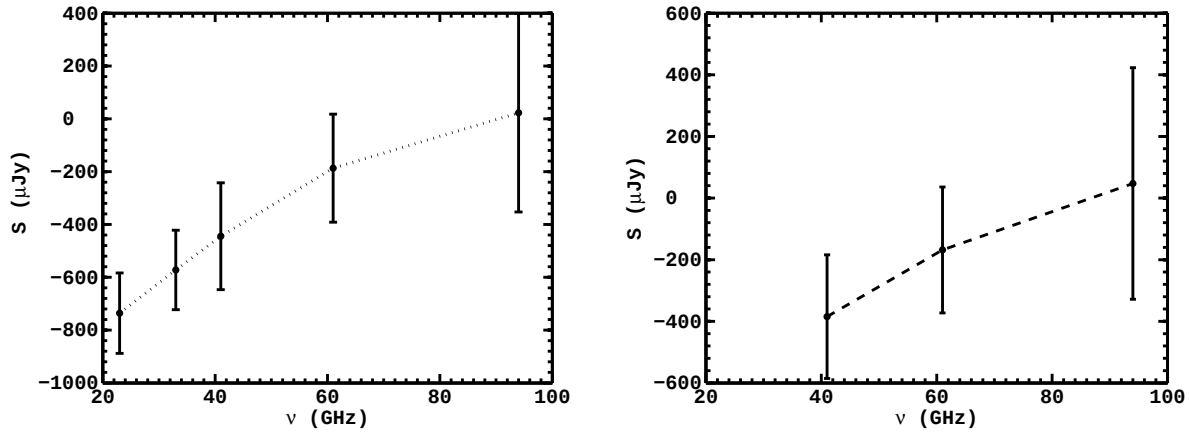

Figure 7.16: Cross-Correlation spectrum of the SDSS LRGs. The left panel shows the spectrum from the filtered raw maps and the right panel shows the spectrum obtained from the filtered foreground reduced maps. We apply the same masks for both the quasar (Fig. 7.13 and Fig. 7.14) and LRG cases. The LRG and the quasar cross-correlation spectra show similar amplitudes and shapes.

7.4.4 Effect of Systematics

To study the effect of systematics we investigate the change in the cross-correlation amplitude by changing the thresholds of our masks. Table 7.8 shows the effect on the cross-correlation amplitude from changes in the threshold of the dust mask . The signal varies significantly with the thresholds of the dust mask. We note that the anti-cross-correlation amplitude increases once we use more restrictive masks. However the sample size changes as we use different mask thresholds and so we chose to adopt the $E(B-V) \geq 0.05$ mask, which optimizes between sample size and systematic bias. We also investigate the response of the radio mask threshold. The changes are not significant when we change the mask thresholds for the radio mask (from 2mJy to 4mJy at 1.4 GHz). We also investigate the effect of radio sources by changing the size of our masks by masking out all pixels that are within a radius of 20 arcminutes from a radio source. We find that the cross-correlation amplitude does not change significantly if we vary the size of our mask.

Band GH	$E(B-V) \geq 0.01$ μJy	$E(B-V) \geq 0.05$ μJy	$E(B-V) \geq 0.1$ μJy
K (23)	-2191.8 ± 839	-1260.2 ± 184.2	-935.8 ± 193.6
Ka (33)	-2215.2 ± 917.6	-802.4 ± 222.4	-870.2 ± 200.6
Q (41)	-2069.2 ± 1279.1	-626.4 ± 266.8	-1113.6 ± 268.4
V (61)	-3090.4 ± 1305.4	-404.8 ± 374.4	-656.6 ± 256.8
W (94)	199.4 ± 2373.2	-492.2 ± 670.4	-247.6 ± 473.4
QF	-1973.6 ± 1274.4	-1018.3 ± 288.5	-889.2 ± 259.9
VF	-3059.4 ± 1305.1	-850.6 ± 340.7	-609.3 ± 256.7
WF	-2249.8 ± 1503.3	-1072.4 ± 626.5	-313.7 ± 47.2

Table 7.8: Effect of the dust mask on the cross-correlation estimator. The amplitude of the cross-correlation changes significantly once we change the thresholds of our masks.

7.5 INTERPRETATION OF RESULTS

We can now compare our results with theory. We adopt the fits shown in Fig. 7.14 from the foreground reduced maps for the comparison. We adopt the profile of y distortion described in Eq. 4.16. We assume the halo mass to be $3 \times 10^{12} M_{\odot}$ (from the quasar clustering studies of Coil et al. 2007). We adopt the mean redshift of our sample ($z = 1.6$) for comparing with theory. The theoretical values can be obtained from Eq. 5.4. The y distortion fits from Table 7.6 (3rd and 4th Columns) give $y = i_0 y / i_0$. This number should be divided by the pixel size in equivalent steradians (4×10^{-6}). We do not compare our theoretical results with the other sets shown in Table 7.6, since the fits are not significant. The comparison between theory and observation is shown in Table 7.9 The values obtained from the data are two orders of magnitude higher than the values predicted from theory (see Table 7.9). But we note that the theoretical signal is a strong function of redshift, halo mass, and other parameters in the model and can vary substantially depending on these parameters. Also, large scale structures (galaxy clusters for example) are unresolved at WMAP scales and so

Fitting Model	Observed values of y 10^{-7}	Theoretical values of y 10^{-7}
SZ+Dust	5.8 ± 1.8	.045
SZ	4.2 ± 2.28	.045

Table 7.9: Comparison between observed and theoretical values of the y parameter. The theoretical values are obtained from the model described in Chapter 4. Column 1 lists the models that are used to fit the spectrum.

it is hard to predict the real source of the signal.

WMAP is barely sensitive to the scale of galaxy clusters (e.g; Refregier, Spergel, & Herbig 2000). The observed correlation of flux decrement with the LRGs is similar to that for quasars. This suggests that the sources of the signals might be similar. LRGs are tracers of galaxy clusters and hence the SZ effect that we observe could be originating from galaxy clusters associated with quasars. Diego & Partridge (2009) finds the SZ signal from galaxy clusters to be in the range $(10-20)$ μK ($\approx$ tens of mJy at WMAP frequencies). The fluxes we get are of the order of 1 mJy. The theoretically predicted SZ signal from quasars is $(10-100)$ μJy (at WMAP frequencies), depending on the mass of the black hole (Chatterjee & Kosowsky 2007; Scannapieco, Thacker, & Couchman 2008). Our signal is at least an order of magnitude higher than the signal that we expect from quasars and an order of magnitude less than what is expected from massive galaxy clusters. Coil et al. (2007) have studied the clustering of quasars at redshift $0.7 < z < 1.4$ identified by the Deep Extragalactic Evolutionary Probe 2 Galaxy Redshift (DEEP2) (Davis et al. 2007) Survey and SDSS. The results show that at these redshifts quasars tend to reside in halos of masses $\approx 3 \times 10^{12} M_{\odot}$. The median redshift of the quasars in our sample is $1.3-1.4$. This implies that the quasars studied are mostly residing in lower mass halos than galaxy clusters. However if a small fraction of the total quasars reside in galaxy clusters then that could explain the magnitude of the signal that we get from our analysis. If 10% of the quasars reside in $10^{14} - 10^{15}$ $M_{\odot}$ halos we would get a signal of $\approx$ 1 mJy. This is comparable to what has been observed

in the current analysis. The other possibility is that the SZ signal from quasars is higher (Natarajan & Sigurdsson 1999) than what is obtained from the simulations used to predict the SZ amplitude.

7.5.1 Projections for ACT

If we assume the size of the source to be 10 arcseconds then the SZ signal in a beam of size θ (in arcsecond) will be roughly $\Delta T \times (10/\theta)^2$, where ΔT is the theoretical signal described in Chapters 4 and 5. The beam size for WMAP W band is 12 arcminutes. So for a ΔT of 1 μK the signal will be 0.2 nK. The noise from WMAP is roughly 30 μK. With $500,000$ sources this gives a signal-to-noise of .003. Although, by filtering the maps we have increased the signal-to-noise by a sufficient amount but we are still limited by statistics. It is shown in Chapter 4 that the signal is a strong function of redshift, halo mass and other parameters. Within the uncertainties in the modeling parameters, if we assume a theoretical signal to be about 1 μK, then our estimate shows the signal for ACT to be roughly .03 μK. ACT plans to attain a nominal noise of 10 μK per pixel. This gives a signal-to-noise of 0.003. Data from SDSS contain around 30 quasars with photometric redshifts per square degree (Richards et al. 2006). With a 400 square degrees of sky coverage we can get a 3σ detection of the signal. However we will still be limited by systematic effects and confusion due to SZ signal from galaxy clusters.

8.0 CONCLUSIONS

In this Chapter, I will summarize the results of this thesis work. In §8.1 I will give the summary of results. In §8.2 I will describe some of the issues that needs further attention, and in §8.3 I will suggest some future extensions of this work.

8.1 SUMMARY OF RESULTS

The main goal of this thesis is focused on using the CMB to understand the physics of AGNs. This involves characterizing the hot gas in AGN environments, via their SZ signatures in the CMB. Probing black hole energy feedback via SZ distortions gives us a new observational tool to study the role of AGN feedback in structure formation.

In Chapter 2, I derived the SZ spectral distortion in the CMB from a thermalised distribution of electrons, under the non-relativistic and small energy transfer limit of the Boltzmann Equation. This effect was first discovered by Sunyaev & Zeldovich (1969), and the same results have been reproduced in this thesis. I have also discussed the theoretical and observational aspects of the CMB with particular emphasis on the SZ effect.

In Chapter 3, I have discussed some theoretical models and observational evidences of AGN feedback and its role on formation of structures.

In Chapter 4 of this thesis we calculated the SZ distortion from an AGN, using a simple one-dimensional Sedov-Taylor model of energy outflow. We obtained the profiles of y distortion using simplified assumptions about the source geometry and the redshift distribution of energy input from the AGNs. The typical temperature of this hot bubble is 10^6K with sizes ranging from a few hundred kpcs to a few Mpcs. Using a halo model formalism, we

calculated the angular power spectrum of the temperature distortion. The power spectrum has two peaks. The primary peak occurs at $l = 400$, which is the correlation scale of large scale structures. The secondary peak occurs around $l = 3 \times 10^4$, at an angular scale of $\sim 20''$ (the characteristic size of a hot bubble at higher redshifts). We investigated the dependence of the power spectrum on free parameters of the model. Reducing the energy input redshift z_{in} from 3 to 2.5 reduces the power spectrum by roughly a factor of 2. The dependence on maximum mass $M_{\rm max}$ is relatively weak: the power spectrum amplitude increases only by 60% if the maximum mass is increased by a factor of 5. Using a Gaussian beam we calculated the signal for a model ACT-like experiment. The signal has an amplitude of the order of one micro-Kelvin. This signal will be at the noise limit of current arcminute-scale microwave background experiments, including ACT and SPT.

In Chapter 5, we further characterized the signal from cosmological-hydrodynamical simulations with black hole feedback. We simulated high resolution maps of the SZ distortion in the CMB due to the feedback energy from accretion onto supermassive black holes. These simulations address the rapid accretion phases of black holes (see Hopkins, Narayan, & Hernquist 2006; Di Matteo et al. 2008). The result is heating of the gas surrounding the black hole. The results show that with the turn on of AGN feedback the SZ signal gets enhanced largely and the enhancement is predominant at angular scales of 5 arcseconds. The signal from the largest black holes has a characteristic amplitude of sub μK to a few μK. We obtained a scaling relation between the black hole mass and their SZ temperature decrement, which in turn is a measure of the amount of feedback energy output. We also investigated the correspondence between y distortion and accretion rates. The correspondence between the y distortion and the accretion rates is not exact but there is a close association which shows the correlation between feedback energy output and black hole activity.

In Chapter 6, we designed an experiment using the maps presented in Chapter 5 to directly detect the signal. The combination of angular scale and small amplitude make detecting this effect very challenging, at the margins of currently planned experiments. We show that a very deep observation with ALMA can potentially detect this signal. We also discuss the technique of detecting this signal by stacking microwave images centered on known quasars.

In Chapter 7, we estimated the cross-correlation signal from the SZ distortion produced by hot gas in the environments of AGNs by stacking CMB temperature maps from WMAP centered on SDSS quasars. The effective contamination to this signal comes from dust, galactic foregrounds, radio emissions from quasars, and the primary temperature fluctuations in the black body. Different masks and spatial filters are applied to minimize the systematic effects. We use two models to fit the cross-correlation spectrum. One model involves SZ and the other model involves SZ and dust. The reduced χ^2 values for the two fits are 2.76 and 2.01, respectively. We use the BIC criterion to test the validity of these models. The BIC values indicate that inclusion of the dust parameter improves the fits significantly. The best-fit values for the y parameter are $(4.2 \pm 2.28) \times 10^{-7}$ and $(5.8 \pm 1.8) \times 10^{-7}$ respectively, for the two models. At WMAP scales it is difficult to resolve point sources from galaxy clusters and so we conclude that the signal is likely to be coming from galaxy clusters. Finally, we presented the projected signal-to-noise for ACT observations and concluded that the chances for detecting this cross-correlation signal with ACT is significantly higher than WMAP within the limits of contamination from other sources.

8.2 DISCUSSION OF RESULTS

The SZ effect from quasars acts as a contamination in SZ surveys that propose to detect galaxy clusters. Since the amplitude of this signal ($\sim 1\mu$K) is well below the amplitude of the SZ distortion from galaxy clusters ($\sim 100\mu$K), this effect will not be important for detecting galaxy clusters. This signal is at or below the target noise level of SZ experiments like ACT and SPT. However the signal is interesting, if we consider it as a viable probe for detecting hot gas in AGN environments. The theoretical models and experimental probes discussed in this thesis can serve as interesting directions for eventually detecting this signal. In this Section, I will discuss some of the major issues related to different aspects of the work described in this dissertation.

The one-dimensional Sedov-Taylor solution is used to model the energetics of the quasar environment. The Sedov-Taylor model is valid for a point-like explosion in an uniform

medium. The assumption of point-like explosion is valid since the duration time of the explosion is much shorter than the expansion time of the bubble. However the assumption about the uniform density of the medium needs some justification. The density of the medium will likely have a power law dependence. In addition, the medium will not be static (Scannapieco & Oh 2004). The results obtained from numerical models that solve the coupled differential equations involving radial dependence of the density profile and the accretion infall are similar to the Sedov-Taylor solution (Barkana & Loeb 2001; Furlanetto & Loeb 2001). The assumptions of spherical symmetry, uniform temperature, and uniform density of the gas within the bubble are also approximate. These are used to obtain a closed form solution. Another assumption involves the redshift distribution of energy injection. We assume a delta-function distribution where all the quasars eject their energy at a single redshift. A more realistic approach would use the quasar luminosity functions to characterize the redshift distribution of quasars.

The other issue involves δ_s, which relates to the density of the AGN environment. In simulations AGNs tend to live in dense environments but this needs more observations to be confirmed. The signal scales weakly with δ_s. However, depending on the value of δ_s, the conclusions about detectibility can vary. Another important issue involves the mode of energy feedback. As discussed in Chapter 3, the two possible modes of feedback are radio mode and quasar mode. The radio or the mechanical mode geometry is in the form of a collimated jet whereas the quasar mode is isotropic. The assumption of isotropy and spherical symmetry intrinsically implies a quasar mode. Radio loud quasars transport most of their energy in the mechanical mode. In the radio quiet population the outflow could be in the form of winds (e.g., Blandford & Payne 1982; Proga, Stone & Kallman 2000; Pereyra, Hillier, & Turnshek 2006). In both cases the isotropic mode is not the main outflow geometry. However, the amplitude of the SZ signal will not depend significantly on the mode of energy transfer.

The next key issue is the assumption about the feedback efficiency. Di Matteo et al. (2008) assumes that the feedback energy is 0.5% of the rest mass energy when AGNs are operating in the quasar mode. This assumption is based on the normalization of the $M - \sigma$ relation. This feedback fraction reproduces the correct $M - \sigma$ relation in the local universe

(Tremaine et al. 2002). Sijacki et al. (2007) investigates AGN feedback in galaxy clusters with the mechanical mode. The mechanical feedback fraction assumed by Sijacki et al. (2007) is 2% of the rest mass energy. This assumption predicts an $M-\sigma$ relation that varies significantly at the low mass end, from the observed $M-\sigma$ relation. However the simulation carried out by Sijacki et al. (2007) reproduces the correct $L_X - T$ relation in galaxy groups and clusters (Puchwein, Sijacki, & Springel 2008). The SZ signal depends on the feedback efficiency and the assumption on feedback efficiency can also affect the detectibility of the effect.

The simulation we have used assumes seed black holes, with masses $10^5 h^{-1} M_\odot$. The motivation behind choosing a seed mass of $10^5 h^{-1} M_\odot$ comes from currently proposed scenarios of seed black hole formation. To have a supermassive black hole of mass $10^9 M_\odot$ in less than a billion years (as indicated by the $z = 6$ quasars in SDSS), current theories require, either: (1) formation of seed black holes of mass $10^4 - 10^6 M_\odot$ from the catastrophic collapse of supermassive stars (Bromm & Loeb 2003) or (2) formation of smaller seed black holes (masses $10^2 M_\odot$) and exponential growth afterwards (Bromm & Larson 2004). The choice of $10^5 h^{-1} M_\odot$ approximately matches the two scenarios described above. For scenario one, the choice of seed mass falls in the right range. The seed black holes are introduced into halos of masses $\geq 10^{10} h^{-1} M_\odot$. Eddington growth predicts that a black hole of mass $10^2 M_\odot$ will roughly grow to a value of $10^5 M_\odot$ by the time collapsed objects of masses $10^{10} M_\odot$ are formed (Di Matteo et al. 2008).

The cross-correlation analysis presented in Chapter 7 shows a first step for detecting the SZ signal from quasars. At frequencies below the null frequency the SZ signal is a decrement and this makes it unique compared to the involved systematics at those frequencies. However observations near and above the null frequency will give more robust confirmation about the origin of the signal. In the present work we get a deficit in flux which suggests SZ, but the fits to the observed spectrum are not sufficiently robust to confirm this conclusion. It is possible that these results come from the cold spots in the primary CMB signal but the primary CMB signal is unlikely to correlate with quasar positions. We need further investigations to study the source of this signal. Wright et al. (2009), Hinshaw et al. (2007), and Chen & Wright (2008) report detections of negative fluxes associated with the point source amplitudes in

the WMAP 3yr and 5yr point source catalogs. The observed correlation with the LRGs are the same as the observed correlations with quasars. This suggests that the source of the signal might be similar. LRGs are tracers of galaxy clusters and hence the SZ effect that we observe can also be originating from galaxy clusters. We note that the detection of the SZ effect from quasars will always suffer from the systematic noise of SZ distortion from galaxy clusters.

The optimum way to disentangle the cluster contribution is to look at field AGNs. Also the SZ effect is still sub dominant at angular scales probed by WMAP (see Komatsu & Seljak 2002). The Planck surveyor satellite and ongoing CMB experiments like ACT and SPT will be sensitive to scales where the SZ signal will be more dominant compared to the primary temperature fluctuations. This will increase the signal per pixel from SZ. Resolving galaxy clusters in Planck or ACT maps will give us a better control on subtracting the cluster contribution to the SZ signal. The detector noise thresholds for Planck and ACT/SPT will be an order of magnitude lower than WMAP. This makes the plausibility of detecting this signal better with future CMB experiments. The filtering technique that has been used in the current work has certain limitations in dealing with C_l^{CMB} as a noise term. Chen & Wright (2008) introduce a CMB free filtering technique which increased the number of source detections in the 5yr maps. This technique can also be applied to the current problem.

8.3 FUTURE WORK

There can be several possible extensions of the work presented in this thesis.

The mass scaling relations shown in Table 5.3 capture the time-dependent component of AGN feedback. The simulation that we have used offers the possibility of tracking the accretion history and duty cycle of an individual black hole. The issue of time dependence of feedback and its connection with accretion rates can be studied by simulating the SZ signal and observing its time dependence over the whole evolutionary history of a black hole. The simulation also offers the possibility of studying quasar environments and how they depend on different parameters. One of the interesting application would involve studying

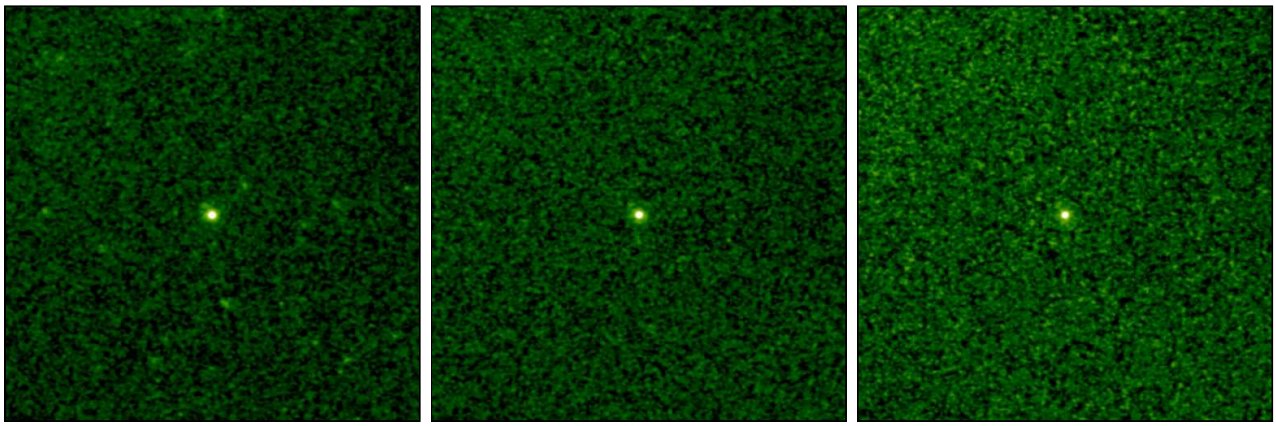

Figure 8.1: Co-added maps of the AGNs (in the EGS field) in three X-ray bands. The three bands are $0.5-2$ Kev (left), $2-4$ Kev (middle), and $4-7$ Kev (right). The maps are 5 arcminutes on each side.

the environmental effects on accretion rates of supermassive black holes from the simulation. Prochaska & Hennawi (2008) show a novel technique to study the environments of a quasar by using a background quasar in the line of sight to study the physical state of the foreground quasar. With KECK HIRES Echelle spectograph they measured HI column densities. The measurement of these column densities will provide constraints on the kinematics, temperature and ionization structure of the quasar environment (Prochaska & Hennawi 2008). Our simulations can be used to compute HI column densities around individual black holes. The results from the simulation can be directly compared with the data.

With the simulation we can also do an X-ray analysis of the black hole environments which will be complimentary to the SZ analysis that we have already done. With a combined X-ray and SZ analysis of the same effect we will be able to put stronger constraints on theoretical models of feedback. The X-ray results can be directly compared with observations. Currently, I am involved in detecting AGN feedback (Chatterjee et al. 2009 (in prep)) by stacking *Chandra* maps of DEEP 2 AGNs in the Extended Groth Strip (EGS). The stacked X-ray maps are shown in Fig. 8.1 in three energy bands. An interesting application of the cross-correlation analysis will involve stacking galaxy clusters from public X-ray and Optical

catalogs (SDSS-MaxBcg) to detect the SZ signal from galaxy clusters. ALMA mock observations derived from the simulations and the maps presented in Chapter 5 will be useful in outlining the feasibility of direct detection.

The CMB has been used as a back light to study a number of physical processes in the universe. In the present work we emphasize the technique of using the CMB to study an important aspect of theories involving galaxy formation, namely feedback from AGNs. I hope this work will initiate more exciting and detailed studies in the field.

BIBLIOGRAPHY

[1] Abazajian, K., et al. 2003, AJ, 126, 2081

[2] Afshordi, N., Loh, Y., & Strauss, M., 2004, PhRvD, 69, 083524

[3] Afshordi, N., Lin, Y. T., & Sanderson, A. J. R., 2005, ApJ, 629, 1

[4] Aghanim, N., Balland, C., & Silk, J., 2000, A&A, 357, 1

[5] Aghanim, N., Gorski, K. M., & Puget, J. L., 2001, A&A, 374, 1

[6] Aghanim, N., Majumdar, S., & Silk, J., 2008, RPPh, 71, 066902

[7] Arnaud, M., & Evrard, A. E., 1999, MNRAS, 305, 631

[8] Babich, D. & Loeb, A. 2007, MNRAS, 374, L24

[9] Bagla, J., 2002, JApA, 23, 185

[10] Bahcall, J. N., et al. 1997, ApJ, 479, 642

[11] Barkana, R. & Loeb, A. 2001, Phys. Rep., 349, 125

[12] Barkana, R. & Loeb, A. 2007, Reports on Progress in Physics, 70, 627

[13] Barnes, J., & Hut, P., 1986, Nature, 324, 446

[14] Begelman, M. C., 2001, ASPC, 240, 363

[15] Benson, A. J., Reichardt C., & Kamionkowski M., 2001, MNRAS,

[16] Bennett, C. L., et al. 1996, ApJ, 464, L1

[17] Bennett, C. L., et al. 2003, ApJS, 148, 1

[18] Bernardeau, F., 1997, A&A, 324, 15

[19] Best, P. N., et al. 2006a, MNRAS, 368, 67

[20] Best, P. N., et al. 2007, HVCG conference, 166 (Springer-Verlag)

[21] Bhattacharya, S., Di Matteo, T., & Kosowsky, A., 2007, MNRAS, 389, 34

[22] Bhattacharya, S., & Kosowsky, A., 2008, PhRvD, 77, 3004

[23] Binney, J., & Tabor, G., 1995, MNRAS, 276, 663

[24] Birkinshaw, M., & Gull, S. F., Northover, K. J. E., 1978, MNRAS, 185, 245

[25] Birkinshaw, M., & Gull, S. F., 1983, Nature, 302, 315

[26] Birzan, L., Rafferty, D. A., McNamara, B. R., Wise, M. W., & Nulsen, P. E. J., 2004, ApJ, 607, 800

[27] Blanchard, A., & Schneider, J., 1987, A&A, 184, 1

[28] Blandford, R. D., & Payne, D. G., 1982, MNRAS, 199, 883

[29] Blanton, E., et al. 2001, ApJ, 558, 15

[30] Bonamente, M., et al. 2006, ApJ, 647, 25

[31] Boehringer, H., et al. 1993, MNRAS, 264, 25

[32] Bode, P., Ostriker, J. P., & Xu, G., 2000, ApJS, 128, 561

[33] Bondi, H., 1952, MNRAS, 112, 195

[34] Bondi, H., & Hoyle, F., 1944, MNRAS, 104, 273

[35] Boughn, S. P., & Crittenden, R. G., 2005, NewAR, 49, 75

[36] Boughn, S.P., & Partridge, B., 2008, PASP, 120, 281, arxiv:0708.4220

[37] Bower, R. G., Benson, A. J., Mallbon, R., Helly, J.C., Frenk, C. S., Baugh, C. M., Cole, S., & Lacey C. G., 2006, MNRAS, 370, 645

[38] Bradac, M., et al. 2006, ApJ, 652, 937

[39] Branduardi-Raymont, G., et al. 1981, ApJ, 248, 55

[40] Bromm, V., & Larson, R. B., 2004, ARA&A, 42, 79

[41] Bromm, V., & Loeb, A., 2003, ApJ, 596, 34

[42] Bruggen, M., & Kaiser, C. R., 2002, Nature, 418, 301

[43] Burns, J., 1990, AJ, 99, 14

[44] Carlstrom, J., E., Holder, G., P., & Reese, E. D., 2002, ARA&A, 40, 643

[45] Carlstrom, J., E., Joy, M., & Grego, L., 1996, ApJ, 456, L75

[46] Cattaneo A. et al. 2007, MNRAS, 377, 63

[47] Cen, R., et al. 1990, ApJ, 362, 41

[48] Chartas, G., et al. 2007, AJ, 133, 1849

[49] Chen, X., Wright, E. L., 2008, ApJ, 681, 747

[50] Cheng, L. M., Wu, X. P., & Cooray, A., 2004, A&A, 413, 65

[51] Ciotti, L., & Ostriker, J. P., 2001, ApJ, 551, 131

[52] Clowe, D., et al. 2006, ApJ, L109

[53] Coil, A. L., Hennawi, J. F., Newman, J. A., Cooper, M. C., & Davis, M., 2007, ApJ, 654, 115

[54] Colafrancesco, S., Dar, A., & De Rujula, A., 2004, A&A, 413, 441

[55] Cole, S., & Kaiser, N., 1988, MNRAS, 233, 637

[56] Condon J. J., et al. 1998, ApJ, 115, 1693

[57] Cooray, A., & Sheth, R. K. 2002, Phys. Rep., 372, 1

[58] Cooray, A., 2002a, PhRvD, 65, 3518

[59] Cooray, A., 2002c, PhRvD, 65, 3512

[60] Couchman, H. M. P., 1991, ApJ, 368, L23

[61] Cowie, L. L., Songaila, A., Hu, E. M., & Cohen, J. G., 1996, AJ, 112, 89

[62] Croft, R. A. C., Banday, A. J., & Hernquist, L., 2006, MNRAS, 369, 1090

[63] Croft, R.A.C., Di Matteo, T., Springel, V., Hernquist, L., 2008, MNRAS, submitted

[64] Croton, D., et al. 2006, MNRAS, 365, 11

[65] Dalla Vecchia, C., et al. 2004, MNRAS, 355, 995

[66] Das, S., & Spergel, D. N., 2008, PhRvD, 79, 043509

[67] Davis, M., et al., 2007, ApJ, 660, L1

[68] De Zotti, G., Burigana, C., Cavaliere, A., Danese, L., Granato, G. L., Lapi, A., Platania, P., & Silva, L., 2004, AIPC, 703, 375D

[69] de Bernardis, P., et al. 2000, Nature, 404, 955

[70] deKool, M., 1997, arxiv: 9704230

[71] Dickinson, C., et al. 2004, MNRAS, 353, 732

[72] Diego, J. M., Silk, J., & Sliwa, W., 2003, MNRAS, 346, 940

[73] Diego, J. M., Hansen, S. H., & Silk, J., 2003, MNRAS, 338, 796

[74] Diego, J. M., & Partridge, B, preprint, arxiv: 0907.0233

[75] Di Matteo, T., Springel, V., & Hernquist, L., 2005, Nature, 433, 604

[76] Di Matteo, T., Colberg, J., Springel, V., Hernquist, L., & Sijacki, D., 2008, ApJ, 676, 33

[77] Dodelson, S., & Jubas, J. M., 1995, ApJ, 439, 503

[78] Dodelson, S., 2002, Modern Cosmology, Academic Press (Amsterdam)

[79] Dubinski, J., Mihos, C. J., & Hernquist, L. 1996, ApJ, 462, 576

[80] Dunkley, J., et al. 2009, ApJS, 180, 306

[81] Dunn, R. J. H., Fabian, A. C., & Taylor, G. B., 2005, MNRAS, 364, 1343

[82] Dunn, R. J. H., & Fabian, A. C., 2006, MNRAS, 373, 959

[83] Eddington, A., 1926, The Internal Constitution of the Stars, Cambridge University Press

[84] Efstathiou, G., et al. 1985, ApJS, 57, 241

[85] Eisenstein, D. J., & Hu, W., 1999, ApJ, 496, 605

[86] Eisenstein, D. J., et al. 2005, ApJ, 633, 560

[87] Ellingson, E., Yee, H. K.C., & Green, R. F., 1991, ApJ, 371, 49

[88] Fabian, A. C., 1994, Ann. Rev. Astron. Astrophys., 32, 277

[89] Fabian, A. C., 1999, MNRAS, 308, 39

[90] Fabian, A. C., et al. 2002, MNRAS, 331, 369

[91] Fabian, A. C., et al. 2003, MNRAS, 344, 43

[92] Fabian, A. C., et al. 2005, MNRAS, 363, 891

[93] Ferrarese, L., & Merritt, D., 2000, ApJ, 539, L9

[94] Ferrarese, L., 2002, ApJ, 578, 90

[95] Fixsen, D. J., & Mather, J. C., 2002, ApJ, 581, 817.

[96] Francis, M. R., Bean, R., & Kosowsky, A., 2005, JCAP, 12, 001

[97] Frenk, C. S., et al. 1999, ApJ, 525, 554

[98] Fosalba, P., Gaztanaga, E., & Castander, F. J., 2003, ApJ, 597, L89

[99] Fosalba, P., & Gaztanaga, E., 2004, MNRAS, 350, L37

[100] Forman, W., Kellogg, E., Gursky, H., Tananbaum, H., & Giacconi, R., 1972, ApJ, 178, 309

[101] Forman, W., et al. 2005, ApJ, 635, 894

[102] Freedman, W. L., et al. 2001, ApJ, 553, 47

[103] Fukugita, M., Ichikawa, T., Gunn, J. E., Doi, M., Shimasaku, K., & Schneider, D. P., 1996, AJ, 111, 1748

[104] Furlanetto, S., & Loeb, A., 2001, ApJ, 556, 619

[105] Gallagher, S., et al. 2006, ApJ, 644, 709

[106] Gebhardt, K., et al. 2000, ApJ, 539, 13

[107] Giacconi, R., Kellogg, E., Gorenstein, P., Gursky, H., & Tananbaum, H., 1971, ApJ, 165, L27

[108] Giannantonio, T., Scranton, R., Crittenden, R. G. Nicol, R. C., Boughn, S. P., Myers, A. D., & Richards, G. T., 2008, PhRvD, 77, 123520

[109] Giacintucci, S., et al. 2008, ApJ, 682, 186

[110] Glazebrook, K., et al. 2004, Nature, 430, 6996

[111] Gradshteyn, I. S., & Ryzhik, I. M., 1980, Tables of Integrals, Series, and Products (Academic Press)

[112] Graham, A. W., & Driver, S. P., 2007, ApJ, 655, 77

[113] Gold, B., et al. 2009, ApJs, 180, 265

[114] Gorski, K. M., et al. 2005, ApJ, 622, 759

[115] Granato, G. L., De Zotti, G., Silva, L., Bressan, A., & Danese, L., 2004, ApJ, 600, 580

[116] Guo, F., Oh, S. P., & Ruszkowski, M., 2008, ApJ, 688, 859

[117] Gunn, J. E., & Peterson, B. A., 1965, ApJ, 142, 1633

[118] Gunderson, J.O., et al. 1995, ApJ, 443, L57

[119] Gursky, H., Kellogg, E., Murray, S., Leong, C., Tananbaum, H., & Giacconi, R., 1971, ApJ, 167, L81

[120] Gursky, H., & Schwartz, D. A., 1977, Ann. Rev. Astron. Astrophys, 15, 541

[121] Halverson, N. W., et al. 2002, ApJ, 568, 38

[122] Hanany, S., et al. 2000, ApJ, 545, L5

[123] Heinz, S., et al. 2002, ApJ, 569, 79

[124] Helsdon, S. F., & Ponman, T. J., 2000, MNRAS, 315, 356

[125] Hernandez-Monteagudo, C., Macias-Perez, J. F., Tristram, M., & Desert, F., X., 2006, A&A, 449, 41

[126] Hewett, P. C., & Foltz, C. B., 2003, AJ, 125, 178

[127] Hincks, A. D., et al. 2009, arxiv: 0907.0461

[128] Hinshaw, G., et al. 2007, ApJS, 170, 288

[129] Hinshaw, G., et al. 2009, ApJS, 180, 225

[130] Hirata, C. M., Padmanabhan, N., Seljak, U., Schlegel, D., & Brinkmann, J., 2004, PhRvD, 70, 103501

[131] Ho, S., Hirata, C. M., Padmanabhan, N., Seljak, U., & Bahcall, N., 2008, PhRvD, 78, 043519

[132] Ho, S., Dedeo, S., & Spergel, D., 2009, arxiv:0903.2845

[133] Hogg, D. W., 1999, arxiv:/9905116

[134] Holzapfel, W. L., 1997, ApJ, 481, 35

[135] Hopkins, P. F., & Hernquist, L., 2006, ApJS, 163, 50

[136] Hopkins P F., Narayan R., & Hernquist L., 2006, ApJ, 643, 641

[137] Hoyle, F., Burbidge, G., & Narlikar, J.V., 1993, ApJ, 410, 437

[138] Hoyle, F., & Lyttleton, R. A., 1939, in proceedings of the Cambridge Philosophical Society, 405

[139] Hu, W., & Dodelson, S., 2002, Ann. Rev. Astron. Astrophys, 40, 171

[140] Hu, W., Fukugita, M., Zaldarriaga, M., & Tegmark, M., 2001, ApJ, 549, 669

[141] Hu, W., & Haiman, Z., 2002, PhRvD, 68, 063004

[142] Hu, W., 2000, ApJ, 529, 12

[143] Hu, W., 2008, Arxiv:0802.3688b

[144] Huang, Z., & Sarazin, C. L., 1998, ApJ, 496, 728

[145] Iliev, I. T., Pen, U.-L., Bond, J. R., Mellema, G., & Shapiro, P. R. 2006, New Astron. Rev. 50, 909.

[146] Jenkins, A., et al. 2001, MNRAS, 321, 372

[147] Joy, M., et al. 2001, ApJ, 551, L1-L4

[148] Jungman, G., Kamionkowski, M., Kosowsky, A., & Spergel, D.N. 1996, Phys. Rev. Lett. 76, 1007

[149] Kaiser, N., 1986, MNRAS, 222, 323

[150] Kaiser, C. R., & Binney, J. J., 2003, MNRAS, 338, 837

[151] Kamionkowski, M., Kosowsky, A., & Stebbins, A., 1997, PhRvD, 55, 7368

[152] Kang, H., et al. 1994, ApJ, 430, 83

[153] Kaplinghat, M., Knox, L., & Song, Y. S., 2003, PRL, 89, 011303

[154] Kawata, D., & Gibson, B. K., 2005, MNRAS, 358, L16

[155] Kennicut, R. C., 1998, ApJ, 498, 541

[156] Keres, D., et al. 2005, MNRAS, 363, 2

[157] Kesden, M., Cooray, A., & Kamionkowski, M., 2003, PhRvD, 67, 123507

[158] Khochfar, S., & Ostriker, J. P., 2008, ApJ, 680, 54

[159] Komatsu, E., & Kityama, T., 1999, ApJ, 526, 1

[160] Komatsu, E., & Seljak, U., 2002, MNRAS, 336, 1256

[161] Komatsu, E., et al. 2009, ApJS, 180, 330

[162] Kompaneets, A. S., 1957, JETP (Soviet Physics), 730, 4

[163] Kosowsky, A., et al. 2006, New Astron. Rev. 50, 969.

[164] Kowalski, M., et al. 2008, ApJ, 686, 749

[165] Kragh, H., 1999, Cosmology and Controversy, Princeton University Press

[166] Kravtsov, A. V., Klypin, A. A., & Khokhlov, A. M., 1997, ApJS, 111, 73

[167] Landau, L. D., & Lifshitz, E. M., 1987, Course of Theoretical Physics, Vol 6, Fluid Mechanics

[168] Lapi, A., Cavaliere, A., & De Zotti, G., 2003, ApJl, 597, L93

[169] Lapi, A., Cavaliere, A., & Menci, N., 2005, ApJ, 619, 60

[170] Lapi, A., Shankar, F., Mao, J., Granato, G. L., Silva, L., De Zotti, G., & Danese, L., 2006, ApJ, 650, 42

[171] LaRoque, S. J., et al. 2006, ApJ, 652, 917

[172] Lay, O. P., & Halverson, N. W., 2000, ApJ, 787

[173] Levin, R., & Gnedin, N., 2005, ApJ, 632, 727

[174] Levin, R., & Gnedin, N., 2006, ApJ. 649, 57

[175] Lewis, A., Challinor, A., Lasenby, A., 2000, ApJ, 538, 473

[176] Liddle, A., Mukherjee, P., & Parkinson, D., 2006, arxiv: astro-ph/0608184

[177] Magorrian, J., et al. 1998, AJ, 115, 2285

[178] Marconi, A., & Hunt, L. K., 2003, ApJ, 589, L21

[179] Markevitch, M., 1998, ApJ, 504, 27

[180] Majumdar, S., Nath, B., & Chiba, M., 2001, MNRAS, 324, 537

[181] Mason, B. S., et al. 2003, ApJ, 591, 540

[182] Massardi, M., Lapi, A., de Zotti, G., Ekers, R. D., & Danese, L., 2008, MNRAS, 384, 701

[183] Mather, J. C., et al. 1990, ApJ, 354, L37

[184] McKee, C. F., & Ostriker, J. P., 1977, ApJ, 218, 148

[185] McLure, R. J., & Dunlop, J. S., 2001, MNRAS, 321, 515

[186] McNamara, B. R., et al. 2000, ApJ, 534, 135

[187] McNamara, B. R., et al. 2001, ApJ, 562, 149

[188] McNamara, B. R., Nulsen, P. E. J., Wise, M. W., Rafferty, D. A., Carilli, C., Sarazin, C. l., & Blanton, E. L., 2005, Nature, 433, 45

[189] McNamara, B. R., & Nulsen, P. E. J., 2007, ARA&A, 45, 117

[190] McQuinn, M., Furlanetto, S. R., Hernquist, L., Zahn, O., & Zaldarriaga, M., 2005, ApJ, 630, 643

[191] Menci, N., et al. 2006, ApJ, 647, 753

[192] Merritt, D., & Ferrarese, L., 2001, ApJ, 547, 140

[193] Michel, F. C., 1971, Astrophysics and Space Science, 15, 153

[194] Miller, A. D., et al. 1999, ApJ, 524, L1

[195] Mo, H. J., & Mao, S., 2002, MNRAS, 333, 768

[196] Mohr, J. J., 2005, ASPC, 339, 140

[197] Moodley, K., Warne, R., Goheer, N., & Trac, H., 2008, arxiv:0809.5172

[198] Monaghan, J. J., 1992, ARA&A, 30, 543

[199] Myers, A. D., Shanks, T., Outram, P. J., Frith, W. J., & Wolfendale, A. W., 2004, MNRAS, 347, L67

[200] Nagai, D., 2006, ApJ, 650, 538

[201] Nath, B. B., & Roychowdhury, S., 2002, MNRAS, 333, 145

[202] Natarajan, P., & Sigurdsson, S., 1999, MNRAS, 302, 288

[203] Nolta, M., et al. 2009, ApJS, 180, 296

[204] Norman, M. L., & Bryan, G. L., 1998, ASSL, 240, 19, arxiv:/9807121

[205] Nulsen, P., McNamara, B., David, L., & Wise, M., 2004, cosp, 35, 3235

[206] Oh, S. P., Cooray, A., & Kamionkowski, M. 2003, MNRAS, 342, 20

[207] Oh, S. P., & Benson, A., 2003, MNRAS, 342, 664

[208] Ostriker, J. P., & Vishniac, E. T., 1986, ApJ, 306, L51

[209] Padin, S., et al. 2001, ApJ, 549, L1

[210] Padmanabhan, N., et al. 2005a, MNRAS, 359, 237

[211] Padmanabhan, N., Hirata, C. M., Seljak, U., Schlegel, D. J., Brinkmann, J., & Schneider, D. P., 2005b, PhRvD, 72, 043525

[212] Page, L., et al. 2003, ApJS, 148, 39

[213] Page, L., et al. 2007, ApJS, 170, 335

[214] Peacock, J. A., 1999, Cosmological Physics (Cambridge university press)

[215] Peebles, P. J. E., & Yu J. T., 1970, ApJ, 162, 815

[216] Peebles, P. J. E., 1980, Large Scale Structure of the Universe Princeton University Press

[217] Peiris, H. V., & Spergel, D. N., 2000, ApJ, 540, 605

[218] Penzias, A. A., & Wilson, R. W., 1965, ApJ, 142, 419

[219] Percival, W. J., et al. 2007, MNRAS, 381, 1053

[220] Pereyra, N. A., Hillier, J. D., & Turnshek, D., 2006, ApJ, 636, 411

[221] Perlmutter, S., et al. 1999, ApJ, 517, 565

[222] Peterson, R., & Fabian, A., 2006, Phys. Rep., 427, 1

[223] Pettini, M., et al. 2001, ApJ, 528, 96

[224] Platania, P., Burigana, C., De Zotti, G., Lazzaro, E., & Bersanelli, M., 2002, MNRAS, 337, 242

[225] Proga, D., Stone, J. M., & Kallman, T. R., 2000, ApJ, 543, 686

[226] Puchwein, E., Sijacki, D., & Springel, V., 2008, ApJ, 687, L53

[227] Quilis, V., et al. 2001, MNRAS, 328, 1091

[228] Rafferty, D. A., et al. 2006, ApJ, 652, 216

[229] Rashkov, V., 2009, (unpublished Princeton senior thesis)

[230] Reichardt, C. L., et al. 2009, ApJ, 694, 1200

[231] Reichard, T. A., et al. 2003, AJ, 126, 2594

[232] Rees, M. J., & Scaima, D. W., 1968, Nature, 517, 611

[233] Rees, M. J., & Ostriker, J. P., 1977, MNRAS, 179, 541

[234] Refregier,A., Spergel, D. N., & Herbig, T., 2000, ApJ, 531, 31

[235] Reynolds, C., et al. 2002, MNRAS, 332, 271

[236] Richards, G. T. et al. 2006, AJ, 131, 2766

[237] Riess, A. G., et al. 1998, AJ, 116, 1009

[238] Riess, A. G., et al. 2004, ApJ, 607, 665

[239] Rephaeli, Y., 1995, ARA&A, 33, 541

[240] Rosa-Gonzalez, D., Terlvich, R., Terlvich, E., Friaca, A., & Gaztanaga, E., 2004, MNRAS, 348, 669

[241] Roychowdhury, S., Ruszkowski, M., & Nath, B. B. 2005, ApJ, 634, 90

[242] Roychowdhury, S., et al. 2004, ApJ, 615, 681

[243] Ruhl, J. E., et al. 2004, Proc. SPIE, 5498, 11

[244] Rybicki, G. B., & Lightman, A. P., 1985, Radiative processes in astrophysics (John Wiley & Sons)

[245] Ryden, B. S., 2002, Introduction to Cosmology, Addison Wesley

[246] Sachs, R. K. & Wolfe, A. M., 1967, ApJ, 147, 73

[247] Salpeter, E. E., 1955, ApJ, 121, 161

[248] Sanderson, A. J. R., Ponman, T. J., & O'Sullivan, E., 2006, MNRAS, 372, 1496

[249] Sarazin, C., 1988, X-ray emissions from clusters of galaxies (Sky and Telescope)

[250] Scannapieco, E., 2000, ApJ, 540, 20

[251] Scannapieco, E., & Oh, S. P., 2004, ApJ, 608, 62

[252] Scannapieco, E., Silk, J., & Bouwens, R., 2005, ApJ, L13

[253] Scannapieco, E., Thacker, R. J., Couchman, H. M. P., 2008, ApJ, 678, 674

[254] Schawinski, K., Tomas, D., Sarzi, M., Maraston, C., Kaviraj, S., Joo, S., Yi, S., & Silk, J., 2007, MNRAS, 382, 1415

[255] Schlegel, D. J., Finkbeiner, D. P., & Davis, M., 1998, ApJ, 500, 525

[256] Sheth, R. K., & Tormen, G., 1999, MNRAS, 308, 119

[257] Seljak, U., 1996a, ApJ, 460, 549

[258] Seljak, U., 2000, MNRAS, 318, 203

[259] Seljak, U., Slosar, A., & McDonald, P., 2006, JCAP, 10, 14

[260] Shakura, N. I., & Sunyaev, R. A., 1973, A&A, 24, 337

[261] Shields, G. A., et al. 2003, ApJ, 583, 124

[262] Shu, F., 1992, The Physics of Astrophysics, Vol II: Gas dynamics (University Science Books, Mill Valley, California)

[263] Sijacki, D., Springel, V., Di Matteo, T., & Hernquist, L., 2007, MNRAS, 380, 877

[264] Silk, J., 1968, ApJ, 151, 459

[265] Silk, J., 1977, ApJ, 211, 638

[266] Silk, J., & Rees, M. J., 1998, A&A, 331, L1

[267] Silk, J., et al. 1986, ApJ, 307, 1986

[268] Smith, K. M., Zahn, O., & Dore, O., 2007, PhRvD, 76, 043510

[269] Smoot, G. F., et al. 1992, ApJ, 396, L1

[270] Spergel, D. N., et al. 2003, ApJS, 148, 175

[271] Spergel, D. N., et al. 2007, ApJS, 170, 377

[272] Springel, V., Yoshida, N., & White, S. D. M., 2001, New Astronomy, 6, 79

[273] Springel, V., 2005, MNRAS, 364, 1105

[274] Springel, V., & Hernquist L., 2003, MNRAS, 339, 312

[275] Staniszewski, Z., et al. 2008, preprint/arxiv: 0810.1578

[276] Sutherland, R. S., & Dopita, M. A., 1993, ApJS, 88, 253

[277] Sunyaev, R. A., & Zel'dovich, Ya. B., 1972, Comments Astrophys. Space Phys., 4, 173

[278] Sunyaev, R. A., & Zel'dovich, Ya. B., 1980, MNRAS, 190, 413

[279] Tegmark, M., et al. 2004, ApJ, 606, 702

[280] Tegmark, M., & de Oliveira-Costa, A., 1998, ApJ, 500, L83

[281] Thacker, R. J., Scannapieco, E., & Couchman, H. M. P., 2006, ApJ, 653, 86

[282] Totani, T, 2004, PhRvL, 92, 1301

[283] Tremaine, S., et.al. 2002, ApJ, 574, 740

[284] Tristram, M., et al. 2005; A&A, 436, 785

[285] Truelove, J. K., et al. 1998, ApJ, 495, 821

[286] Turnshek, D., 1984, ApJ, 280, 51

[287] Ueda, Y., 2003, ApJ, 598, 886

[288] Verde, L., & Haiman, Z., & Spergel, D. N., 2002, ApJ, 581, 5

[289] Vikhlinin, A., et al. 2009, ApJ, 692, 1060

[290] Voit, G. M., Balogh, M. L., Bower, R. G., Lacey, C. G., & Bryan, G. L., 2003, ApJ, 593, 272

[291] Voigt, L. M., & Fabian, A. C., 2004, MNRAS, 347, 1130

[292] Voit, G. M., & Donahue, M., 2005, ApJ, 634, 955

[293] Vrtilek, J. M., et al. 2008, AAS HEAD meeting, 10, 904

[294] Wang, S., et al. 2004, PhRvD, 70, 123008

[295] Weinmann, S. M., VandenBosch, F. C., Yang, X., Mo, H. J., Croton, D. J., & Moore, B., 2006, MNRAS, 372, 1161

[296] White M., Hernquist, L., & Springel, V., 2002, ApJ, 579, 16

[297] White, S., Navarro, J., Evrard, A., & Frenk, C., 1993, Nature, 366, 429

[298] Wilson, G. W., et al. 2000, ApJ, 532, 57

[299] Wright, E., et al. 2009, ApJS, 180, 283

[300] Wu, K. K. S., Fabian, A. C., & Nulsen, P. E. J., 2000, MNRAS, 318, 889

[301] Wyithe, J. S. B., & Loeb, A., 2003, ApJ, 595, 614

[302] Xu, G., 1995, ApJS, 98, 355

[303] Yamada, M., Sugiyama, N., & Silk, J. 1999, ApJ, 22, 66

[304] Zakamska, N., & Narayan, R., 2003, ApJ, 582, 162

[305] Zaldarriaga, M., 2000, PhRvD, 62, 063510

[306] Zanni, C., Murante, G., Bodo, G., Massaglia, S., Rossi, P., & Ferrari, A., 2005, A&A, 429, 399

[307] Zel'dovich, Ya. B., & Sunyaev, R. A., 1969, Astrophysics and Space Science, 4, 301

[308] Zhang, P., Pen, U., & Trac, H., 2004, MNRAS, 347, 1224

APPENDIX A

SCALE INVARIANCE

The CDM perturbation equation for the kth mode is given by (Ryden 2002)

$$\frac{d^2\delta_k}{dt^2} + 2H\frac{d\delta_k}{dt} - (3/2)\Omega_m H^2 \delta_k = 0. \tag{A.1}$$

The power spectrum of fluctuation is given by $P(k) = \langle|\delta_k|^2\rangle$. Within a sphere of radius k, we can write the mass fluctuations as

$$\left(\frac{\delta M}{M}\right)^2 \propto k^3 P(k),$$
$$\delta M \propto k^{-3/2}(P(k))^{1/2}. \tag{A.2}$$

For a power law spectrum $P(k) = k^n$, we have $\delta M \propto k^{(n-3)/2}$. This enables us to write the perturbation in the gravitational potential as

$$\delta\phi \propto \delta M k \propto k^{(n-1)/2}. \tag{A.3}$$

For $n = 1$ (Harrison-Zeldovich spectrum) $\delta\phi$ is independent of scales and is same for all scales. This particular case is called scale invariance of fluctuations and the power spectrum $P(k) \propto k$ is called a scale invariant power spectrum.

APPENDIX B

SOUND WAVES IN AN IDEAL FLUID

Let us consider an ideal fluid with perturbations δP, $\delta\rho$, $\delta\phi$, and δv in pressure, density, gravitational potential, and velocity. This is a simplified picture of the actual acoustic oscillations that occurred in the early universe. One needs to do a full Boltzmann formalism to study the acoustic oscillations in the CMB (see Dodelson 2002). The Euler equation in linearized variable is given as:

$$\frac{\partial \delta v}{\partial t} = \frac{-\nabla(\delta P)}{\rho_0} - \nabla(\delta\phi). \tag{B.1}$$

The continuity equation is given as:

$$\frac{\partial(\delta\rho)}{\partial t} = \rho_0(\nabla(\delta v)). \tag{B.2}$$

The Poisson equation is given as:

$$\nabla^2(\delta\phi) = 4\pi G\delta\rho. \tag{B.3}$$

Taking the partial derivative of the continuity equation with time and using the Euler equation we have

$$\frac{\partial^2\rho}{\partial t^2} - \nabla^2(\delta P) - \rho_0\nabla^2\phi = 0. \tag{B.4}$$

Using the equation of state $\delta P = c_s^2\delta\rho$ (c_s^2 is the speed of sound), and the Poisson equation we get the following relation:

$$\frac{\partial^2(\delta\rho)}{\partial t^2} - c_s^2\nabla^2\delta\rho = 4\pi G\rho_0\delta\rho \tag{B.5}$$

If $\delta_\rho = A_k \exp(-i\omega t) \exp(i\mathbf{k}.\mathbf{x})$, we get the following dispersion relation,

$$\omega(k) = c_s^2 k^2 - 4\pi G\rho_0. \tag{B.6}$$

For $c_s^2 k^2 > 4\pi G\rho_0$ there is an oscillatory solution and standing waves are generated.

APPENDIX C

COSMOLOGY WITH GALAXY CLUSTERS

Galaxy clusters are interesting probes of cosmology. Galaxy clusters have the following advantages as cosmological probes.

1) Observations are complimentary with CMB and supernovae.

2) There are several observables that can be constructed from galaxy clusters (e.g., SZ flux, X-ray flux, number of galaxies, lensing signatures).

3) It simultaneously allow us to probe the expansion history of the universe and the growth of structures. The three main cosmological observables that can be obtained from galaxy clusters are (see, Hu & Haiman 2003; Verde, Haiman & Spergel 2002; Wang et al. 2004):

1)the evolution of cluster abundance with redshift,

2)cluster power spectrum,

3)galaxy cluster scaling relations.

The number density of clusters is given as follows,

$$\frac{dN}{d\Omega dz} = \left(\frac{dV}{d\Omega dz}\right) \int_{M_{min}}^{\infty} dM \frac{dn}{dM}, \tag{C.1}$$

where the mass function in Eq. C.2 is obtained from a Hubble volume N-body simulation, (Jenkins et al. 2001)

$$\frac{dn}{dM} = -0.315 \frac{\rho}{M} \left(\frac{d\sigma_M}{\sigma_M dM}\right) \exp(-[0.61 - \log(g(z), \sigma_M)]^{3.8}). \tag{C.2}$$

In Eq. C.1 the bracketed term is the comoving volume term, and in Eq. C.2, g(z) is the growth factor. This shows the simultaneous dependence of cluster number density on the expansion history and the growth history respectively.

The cluster power spectrum is given as (Hu & Haiman 2003)

$$P_c(k) = b^2 g(z)^2 \left(1 + \frac{d\ln g(z)}{b d\ln a}\left(\frac{{k_r}^2}{k}\right)\right) P(k), \tag{C.3}$$

where k_r is the radial component of the wave vector. The radial component k_r is proportional to Hubble constant and the transverse component $k_T \propto d_A(z)$ (angular diameter distance). So the cluster power spectrum can also be used to do cosmology. The other method for doing cosmology with galaxy clusters is through scaling relations between SZ flux, X-ray temperature, and virial radius (see Verde, Haiman & Spergel 2002 for details).

APPENDIX D

CLUSTER PROFILES

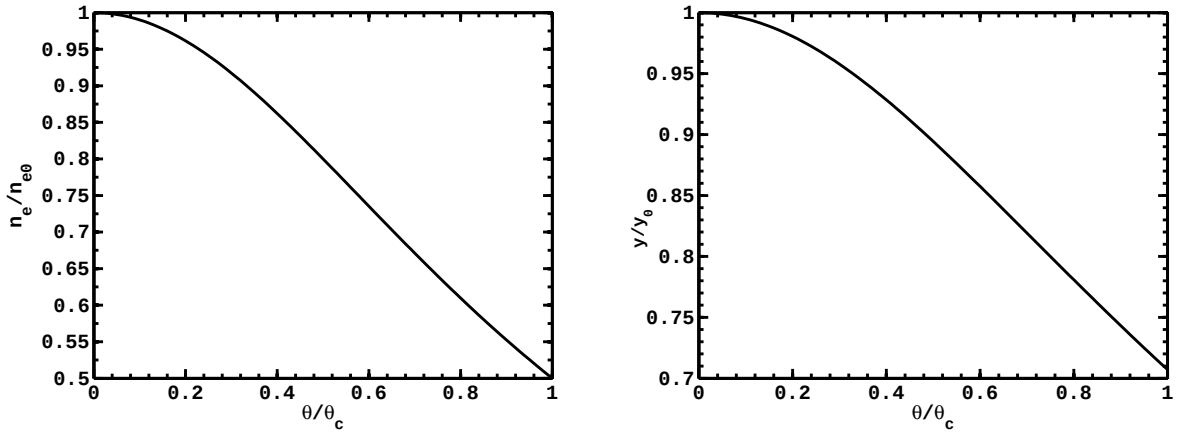

Figure D1: Isothermal β profile for gas density (left panel) and y distortion (right panel) in a cluster. In this model the temperature of the cluster is assumed to be constant.

The electron density profile in galaxy clusters is assumed to be an isothermal β model. This is obtained from simulations. In this model the temperature of the cluster is assumed to be constant and hence the profile is called isothermal. The density and the y distortion profiles are given as follows:

$$n_e = n_{e0}\left(1+\left(\frac{\theta}{\theta_c}\right)^2\right)^{-3\beta/2}, \tag{D.1}$$

$$y = y_0\left(1+\left(\frac{\theta}{\theta_c}\right)^2\right)^{(1-3\beta)/2}, \tag{D.2}$$

where θ_c is the characteristic scale of the cluster. This is different from our model described in Chapter 4 where we have assumed a constant density and a constant temperature profile. For $\beta = 2/3$ the plots are shown in Fig. D1. The y distortion profile shown in Fig. D1 has some similarities with the y distortion profiles shown in Fig. 4.2.

D.1 SMALL ANGLE APPROXIMATION FOR THE ANGULAR FOURIER TRANSFORM

The angular Fourier transform of y distortion (Eq. 4.16) is given as

$$y_l = \int_{-1}^{1} d\cos\theta y(\theta) P_l(\cos\theta). \tag{D.3}$$

We can write the integral representation of the Legendre polynomial as (Peebles 1980)

$$P_l(cos\theta) = \frac{2}{\pi}\int_0^{\theta} \frac{dx\cos(l+1/2)x}{(2(\cos x - \cos\theta))^{1/2}}. \tag{D.4}$$

For, small x and θ we can write $\cos x \approx 1 + x^2/2$, and $\cos\theta \approx 1 + \theta^2/2$. If we now substitute $x = \theta\sin\phi$, we can write Eq. D.4 as

$$P_l(\cos\theta) = \frac{1}{\pi}\int_0^{\pi} \cos((l+1/2)\theta\sin\phi)d\phi, \tag{D.5}$$

where we have explicitly used the fact that the cosine is an even function. The integral representation of the Bessel function is given as

$$J_n(x) = \frac{1}{\pi}\int_0^{\pi} \cos(n\tau - x\sin\tau)d\tau. \tag{D.6}$$

Comparing Eqns. D.5 and D.6 we can write, $P_l = J_0((l+1/2)\theta)$, where we have assumed $\cos(-\beta) = \cos(\beta)$. This enables us to write Eq. D.3 as,

$$y_l = \int \theta d\theta J_0((l+1/2)\theta) y(\theta), \tag{D.7}$$

where we have written $\sin\theta = \theta$. This gives us Eq. 4.17.

APPENDIX E

STAR FORMATION MODEL

The star formation and the associated supernova feedback in the simulation is accomplished in the following way. Each SPH particle represents a region in the Inter Stellar Medium (ISM) and is assumed to be a fluid comprising of cold (density ρ_c) and hot gas (density ρ_h). The density of the gas in that region is $\rho = \rho_c + \rho_h$, and ρ_{star} is the density of stars. The three basic processes that are modeled for mass exchange between the two phases are

(1) star formation from cold gas (clouds),

(2) evaporation of cold clouds due to heating from supernova,

(3) growth of cold cloud due to cooling of hot gas.

This maintains a self-regulatory cycle in the simulation. Star-formation converts clouds into stars in a characteristic time scale t_{star}. A mass-fraction β of these stars instantly die to form supernova. The parameter β is the mass fraction of massive stars. We can thus write,

$$\frac{d\rho_{star}}{dt} = \frac{(1-\beta)\rho_c}{t_{star}}. \tag{E.1}$$

For a Salpeter Initial Mass Function (IMF) (Salpeter 1955) with slope 1.35 and mass limits $40M_\odot$ and 0.1M$_\odot$, $\beta = 0.1$ (Springel & Hernquist 2003). For this particular mass function the average energy that goes into the ISM from each solar mass is $\epsilon_{SN} = 4 \times 10^{48} ergs M_\odot^{-1}$. It is assumed that each supernova gives an energy of 10^{51} ergs. This allows us to write the supernova heating rate as

$$\frac{d\rho_h u_h}{dt} = \epsilon_{SN} \frac{d\rho_{star}}{dt}, \tag{E.2}$$

where u_h is the energy of unit mass of the hot gas. The evaporation of the cold clouds due to heating from the supernova is given as (McKee & Ostriker 1977)

$$\frac{d\rho_c}{dt}|_{EV} = \epsilon_{EV}\beta\frac{\rho_c}{t_{star}}, \tag{E.3}$$

where ϵ_{EV} is the evaporation efficiency. Finally the cooling of the hot gas and hence growth in mass of the cold gas is given as

$$\frac{d\rho_c}{dt} = -\frac{d\rho_h}{dt} = \frac{\Lambda(\rho_h, u_h)}{u_h - u_c}, \tag{E.4}$$

where Λ is the cooling function and u_c and u_h are the energy of unit mass of the cold and hot gas respectively. There are two free parameters in the model. The first one is the effective density of the medium above which there exists a two-phase state of the gas. The second free parameter is the time scale of star formation. The effective density is determined self-consistently by requiring the equation of state to be continuous between the two phases at the onset of star formation (see Springel & Hernquist 2003 for details). The time scale of star formation is obtained by matching the simulation with the observed Kennicut-Schmidt law (Kennicut 1998)

$$\Sigma_{SFR} = (2.5 \pm 0.7) \times 10^{-4} \left(\frac{\Sigma_{gas}}{M_\odot Pc^{-2}}\right)^{(1.4\pm0.15)} \frac{M_\odot}{yrKpc^2}, \tag{E.5}$$

where Σ_{SFR} and Σ_{gas} are the star-formation rate per unit area and surface gas density respectively.

APPENDIX F

BONDI ACCRETION

Bondi accretion is valid for mass accretion onto an object of mass M from a medium with uniform density and with radial flow of the gas in the medium (spherical symmetry). If v be the velocity of the gas with respect to the object of mass M, and ρ be the density of the gas, then the mass accretion rate can be written as $\dot{M} = 4\pi r^2 v\rho$. Using Bernoulli's equation of flow we can write (Bondi 1952)

$$\frac{v^2}{2} + \int \frac{dP}{\rho} - \frac{GM}{r} = 0. \tag{F.1}$$

The local speed of sound is given by $c_s^2 = \gamma P/\rho$ for an adiabatic fluid. After integrating we have the following result, $GM/r = v^2/2 + (c_s^2/\gamma)\ln\rho$. With the following substitution we can write the accretion rate as

$$\dot{M} = \frac{4\pi G^2 M^2 \rho v}{(v^2/2 + c_s^2 \ln\rho/\gamma)^2} \simeq \frac{4\pi G^2 M^2 \rho}{(v^2 + c_s^2)^{3/2}} \tag{F.2}$$

This gives the Bondi formula discussed in Chapter 5.

It is important to note about the physical conditions that apply to different models of accretion. Here, I will discuss the physical pictures of three cases, namely, spherical accretion (Bondi 1952), disc accretion (Shakura & Sunyaev 1973), and relativistic spherical accretion (Michel 1972). The discussion is adopted from Burkhard Zink's presentation. For the Bondi-Hoyle accretion, Newtonian dynamics is used (as shown above). The fluid is assumed to be adiabatic and non-viscous and the flow is assumed to be stationary, hydrodynamic with spherical symmetry. Self gravitation of the accreted matter is neglected. The accretion

sphere is stabilized by pressure gradient (as shown above). There is no radiative transfer in the problem. For the Shakura-Sunyaev model, Newtonian dynamics is assumed. The fluid is viscous and non-adiabatic, and the flow is assumed to be stationary, hydrodynamic with a disc geometry. Self gravitation of the accreted matter is neglected. The accretion sphere is stabilized by centrifugal forces. There is simple radiative transfer in the problem. The relativistic model uses general relativistic assumptions with adiabatic fluid and spherical symmetry.